Fluorescence diffuse optical tomography using time-domain peak time asymptotic analysis

(時間領域ピーク時間の漸近解析による蛍光光拡散トモグラフィー)

Thesis submitted for the Degree of Doctor of Philosophy

by

Shuli Chen

Department of Mathematics
Graduate School of Science
Hokkaido University

· June 2024 ·

Supervised by
Professor Hideo Kubo

Fluorescence diffuse optical tomography using time-domain peak time asymptotic analysis

Thesis submitted for the Degree of Doctor of Philosophy

Shuli Chen

Department of Mathematics
Graduate School of Science
Hokkaido University

· June 2024 ·

Abstract

This thesis concerns an inverse problem for time-domain fluorescence diffuse optical tomography (FDOT) reconstructing multiple point targets from the boundary measured data. The targets are fluorophores. The FDOT process is modeled by two diffusion equations coupled with the source term in a half-space domain (DE model). Our measured data are the time-domain data (temporal response function), measured at some detector points as the temporal response of the fluorescence intensity to an instantaneous injection of the excitation light from a source point. For a fixed pair of detector and source points (S-D pair), the time-domain data has a unique time when the fluorescence intensity reaches its maximum. We call this time the peak time of time-domain data. Physically, the peak time has three unique advantages: (i) it is unique, (ii) it is the least noisy data point in time-domain data, (iii) it can reflect the optical path length distribution. Considering these advantages, the ill-posedness of the inverse problem and large-scale computation costs, we give a precise mathematical analysis and propose an efficient reconstruction algorithm as follows.

We start with studying the asymptotic formulae of the solution to the DE model and its derivative in the case of a single point target. Based on this, we introduce an approximate peak time satisfying a polynomial function, which agrees very well with the peak time obtained by the numerical calculation using typical optical parameters. Then, using approximate peak time and combining it with the bisection method, we propose a mathematically rigorous bisection reconstruction algorithm to reconstruct the target. For multiple point targets, we show the asymptotic formulae of the corresponding solution and its derivative. By choosing a localized S-D pair, we derive a localized asymptotic analysis on a specific target and define its approximate peak time. A localized reconstruction algorithm is proposed under the assumption of well-separateness to the targets. Finally, we consider the target with a small volume and extend the bisection reconstruction algorithm to reconstruct its approximate location.

The novelty of this thesis is that we apply asymptotic analysis to derive reconstruction formulae containing the physical properties of the data. Several numerical experiments show that our proposed algorithms are efficient, robust and accurate even for deeply embedded targets.

Thesis Outline

The time-domain data measured by a pair of source and detect points (S-D pair) for our FDOT problem has a unique peak time when it reaches its maximum. Concerning the physical properties of the peak time that can reflect the distance between the targets and the S-D pair, we develop precise asymptotic analyses to introduce approximate peak times for a single point target and multiple point targets, respectively. Then, we propose some algorithms to reconstruct the location(s) of the target(s) by using the peak time as an index.

For the case of single point target, we first introduce a non-dimensional solution to equally handle the physical parameters inside the solution of the mathematical model of FDOT. We derive the asymptotic formula of the non-dimensional solution in Theorem 3.1, which includes the effect of Robin coefficient. In Theorem 3.2, we derive the asymptotic formula of the time-derivative of the non-dimensional solution in a specific time interval (see the details in (3.1.17)). Since it is asymptotically given in the form of cubic polynomial times a non-vanishing function, as in (3.1.19), we define the approximate peak time as the positive root of the cubic polynomial equation. It turns out that the approximate peak time has very nice accuracy to the peak time, numerically. Based on the approximate peak time formula, we derive the properties (see Theorems 4.2 and 4.3) on the approximate peak time, which are related to the distance between the target and the S-D pair. By the proposed bisection reconstruction algorithm as in Chapter 5, the properties of the approximate peak time will be used to reconstruct the first two coordinates of the location of the target. For the reconstruction of the depth of the target, we can directly solve the cubic equation as in (5.1.1) to obtain the depth of the target. This bisection algorithm is not only rigorous but also numerically effective.

For the multiple point targets case, we can derive the asymptotic formulae of its solution by using the principle of superposition to the asymptotic formulae of the single point target case (See Theorem 6.1). The approximate peak time formula is derived by using a localized S-D pair (See Corollary 6.1). We numerically study the properties of the peak time and the accuracy of the approximate peak time. After this, we define the well-separatedness of multiple point targets as in Definition 6.2 and give a localized reconstruction algorithm to reconstruct the locations of well-separated multiple point targets. Even though we cannot validate this algorithm theoretically, this algorithm numerically works well for well-separated multiple point targets.

We would also like to point out the following. For a region in the measurement surface, we repeat the step of the bisection algorithm only for shrinking the region of the horizontal location of the target a limited number of times, which gives a good approximation of its horizontal location. In addition, the whole reconstruction algorithm is less time-consuming, efficient, potentially robust and accurate for reconstructing the locations of the deeply embedded targets. We also expand this algorithm to reconstruct a marker point of the target with a small volume in Chapter 7.

This thesis is organized as follows:

- Chapter 1: We introduce the background of FDOT and the advantage of the time-domain method, which will be applied to our FDOT problem. We explain the research motivation of this thesis.

- Chapter 2: We briefly describe the derivation of the mathematical model of our FDOT problem. The aim and some related works of our FDOT problem are given.
- Chapter 3: We study asymptotic formulae of solution of our mathematical model for FDOT and its time-derivative in the case of single point target. Some numerical verifications are presented to further explain the asymptotic analysis.
- Chapter 4: We introduce the definition of approximate peak time and its mathematical properties for the case of single point target. Then, we verify the consistency of the properties and the accuracy between the approximate peak time and the peak time, numerically.
- Chapter 5: Based on the properties and the accuracy of the approximate peak time, we present a bisection reconstruction algorithm to reconstruct the location of an unknown single point target from several measured peak times.
- Chapter 6: We start to consider the FDOT problem for multiple point targets. We first derive asymptotic formulae of the solution and its time-derivative. An approximate peak time for each target is defined by using a localized S-D pair. Based on numerical verifications of the approximate peak time, we propose a localized reconstruction algorithm to reconstruct the locations of unknown targets. Some numerical experiments are presented to examine the performance of the proposed algorithm.
- Chapter 7: We consider reconstructing an approximate location of an unknown target from measured peak times, where the unknown target has a small volume. We conduct some numerical experiments to extend the bisection reconstruction algorithm for approximately reconstructing the unknown target.
- Chapter 8: We give conclusions and discuss some future works.

The Chapters 3–5 of this thesis is mainly based on the paper [11].

Acknowledgements

First and foremost, I would like to express my sincere gratitude to my supervisor Prof. Hideo Kubo at Hokkaido University, who gave me kind help and far-sighted guidance on my studying and constant encouragement in life. I would also like to thank him and his colleagues for their meticulous organization of the weekly PDE seminars. I have learned a lot during attending this seminar.

Second, I would like to give my special thanks to Prof. Gen Nakamura (Professor Emeritus, Hokkaido University), Prof. Goro Nishimura (Research Institute for Electronic Science, Hokkaido University) and Dr. Junyong Eom (Research Institute for Electronic Science, Hokkaido University), who are also my advisers and gave me a lot of ideas to write this thesis. Weekly meetings have always been the best memory of my years. During these discussions, I was inspired by their belief and attitude toward academic research, as well as their vision and enthusiasm for multidisciplinary collaboration.

The Department of Mathematics of Hokkaido University has provided me with a perfect learning experience in mathematics and I am grateful to the faculty and staff for their dedicated work. I also appreciate Prof. Masaharu Nagayama (Hokkaido University) for his willingness to share an academic exchange place with me.

Next, I extend my gratitude to Prof. Yikan Liu (Kyoto University) and Dr. Takashi Furuya (Shimane University) for their plenty of help in my studies and my life. I am grateful to my supervisor Prof. Haibing Wang at Southeast University for building a bridge for me to study abroad.

I have been financially supported by China Scholarship Council (No. 202106090240). I am also grateful for the financial support from Hokkaido University, Research Institute for Mathematical Science (RIMS) at Kyoto University, Prof. Gen Nakamura and Prof. Yikan Liu. These grants help me with research and academic exchanges.

Last but not least, I would like to thank my family. I am grateful to my parents for their perennial support and encouragement all through these years. I am deeply indebted to my wife for always being there for me and cheering me up.

——— Shuli Chen, 2024, 3, 28

Contents

Chapter 1

Introduction to FDOT and Inverse Problem

In this chapter, we will briefly introduce the background of fluorescence diffuse optical tomography (FDOT) and some methods of its study in Section 1.1. In Section 1.2, we give the concept of the inverse problem and its difficulty of research. Since FDOT is a typical inverse problem and contains large computational costs, we explain the research motivation of our thesis.

1.1 Fluorescence diffuse optical tomography

1.1.1 Background of fluorescence diffuse optical tomography

FDOT is one of the imaging techniques that makes use of fluorescence light from fluorophores. This imaging technique has potentially powerful potential for medical and biological applications. For some specific diseases and biological activities, their unknown regions can be fluorescently labeled and be reconstructed in a non-invasive way [41, 44, 47]. This imaging technique is also commonly referred to as fluorescence molecular tomography (FMT).

FDOT is an extension of the standard fluorescence imaging method to strongly scattering media like biological tissues. In this medium, the light propagation is considered as an energy dissipation by random scattering. The spatial distribution of fluorescence will be significantly blurred by strong scattering. In this case, many usual imaging techniques cannot be applied to this problem. Since light diffuses strongly, we should first model the propagation of the light, and then the fluorescence image should be reconstructed from the blurred image. FDOT is a method to reconstruct such fluorescence and an essential for the strongly scattering media.

The reconstruction of the distribution of the fluorophores needs to solve an inverse problem with a light propagation model for such media. This inverse problem is the so-called FDOT. This problem is a kind of diffuse optical tomography (DOT) [15] but specifically using fluorescence. As shown in Figure 1.1, for fluorescence, two physical processes are coupled, namely excitation and fluorescence (emission). Excitation photons injected at the boundary of the medium propagate to the fluorophores, and then some of the photons are absorbed by them which excite the fluorophore molecules. After a moment of absorption by fluorophores, the fluorophore emits other photons at a longer wavelength than those of the excitation photons. These photons again propagate until they are observed by a detector located at the boundary of the medium [31, 51].

FDOT has advantages in medical applications because fluorophores can be designed for specific targets. Fluorescence is generated only in this target region, which

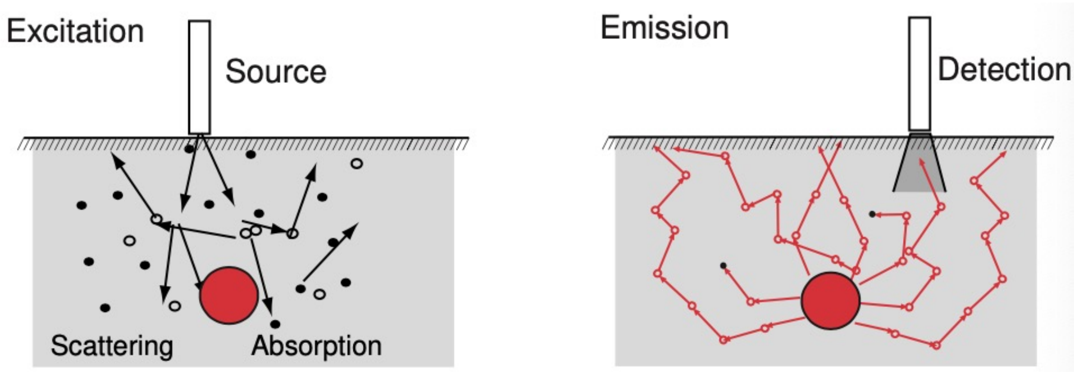

FIGURE 1.1: Physical processes of excitation and emission in FDOT

results in FDOT being potentially sensitive to specificity compared with many DOT applications using intrinsic absorption.

1.1.2 Time-domain method and its advantage

The FDOT or DOT technique can be categorized by measuring physical quantities [5, 28], such as the steady-state fluorescence intensity (continuous wave method; CW method) [12, 27], the temporal response of the fluorescence intensity with an instantaneous injection of the excitation light (time-domain method; TD method) [39, 49], the phase and demodulation of the fluorescence intensity with a sinusoidally modulated excitation light (frequency-domain method; FD method) [2, 43] and a hybrid method of them [48], combining geometrical information of the excitation light source and the detector locations.

The measured data of the TD method is a temporal response function, which records the fluorescence intensity over time when the excitation light is injected. Compared with the measured data of other methods, the unique advantage of this data is that it reflects the optical path length distribution [4]. More precisely, if a single target produces fluorescence, the temporal response function is related to the distance to that object. This relation will guide in reconstructing the location of the target. Therefore, this thesis will focus on the TD method.

Since the TD method provides information on the optical path in the medium, several approaches have been proposed. For example, only early arrival photons are used to reconstruct the geometrical shortest path [9, 46]. However, due to the specular reflections, the limitation of the detector and the insufficient number of photons, the early time of the temporal profiles suffers artifacts, which may cause problems in use. The peak time is used [22, 23], where the peak time is the time when the temporal response function reaches its maximum. The physical intuition of the peak time is similar to the first moment [13, 38] because both reflect the time when the majority of photons arrive. However, the peak time can always uniquely be evaluated and is the least noisy data point in the temporal response function, making it potentially robust in the reconstruction. In this thesis, we focus on this advantage and consider applying the peak time to our FDOT problem (see Section 2.2).

1.2 FDOT as an inverse problem

In this section, we introduce the concept of the inverse problem. Since FDOT is an important, typical and well-studied inverse problem, we will explain the difficulty of studying inverse problems by introducing the definition of ill-posedness. And then we return to our FDOT problem and explain the research motivation.

1.2.1 Concept of inverse problem

When using the terminology, inverse problem, the natural questions are "inverse to what" and "which problem is an inverse problem". The terminology inverse problem is defined as the terminology itself indicates, as the inverse of forward problems. Following Keller [36], one calls two problems inverse to each other if the formulation of one problem involves the other one. For mostly historical reasons, people might call one of these problems (usually the simpler one or the one which was studied earlier) the forward problem, the other one the inverse problem. However, if there is a practical problem behind the mathematical problem studied, there is, in most cases, a quite natural distinction between the forward and the inverse problem. For instance, if we want to predict the future behavior of a physical system from knowledge of its present state and the physical laws (including concrete values of all relevant physical parameters), we will call this the forward problem. Possible inverse problems are the reconstruction of physical parameters from observations of the evolution of the system (parameter identification).

From the applied point of view, we might say the inverse problems are concerned with determining causes giving a measured effect, such as seismic exploration [53], computerized tomography [45], air and water quality control [26], etc. Back to the FDOT problem, it aims to reconstruct the fluorophores quantitatively from the boundary measurements. So FDOT is an inverse problem.

For the mathematical study, we can define inverse problems with the help of abstract operator equations. Let q and f represent the unknown and the measured data of the inverse problem, respectively. Then, we define an operator equation

$$K(q) = f, \tag{1.2.1}$$

where K is an operator acting to the space $\mathcal{Q}$ of the unknown to the space $\mathcal{F}$ of the measured data. The forward problem is to determine f for a given q within the space $\mathcal{Q}$, whereas the inverse problem is to reconstruct q from f for a given K.

1.2.2 Well-posedness and ill-posedness

The well-posedness of problem (1.2.1) was defined by Hadamard [21,37] as follows.

Definition 1.1. *Let $\mathcal{Q}$ and $\mathcal{F}$ be normed spaces and let $K : \mathcal{Q} \mapsto \mathcal{F}$ be a (possibly nonlinear) continuous operator from $\mathcal{Q}$ into $\mathcal{F}$. The inverse problem defined by* (1.2.1) *is well-posed if all three conditions are satisfied:*

(i) **Existence**: *For any $f \in \mathcal{F}$, there exists at least one solution q such that $K(q) = f$, i.e., $Range(K) = \mathcal{F}$.*

(ii) **Uniqueness**: *For any $f \in \mathcal{F}$, the solution q^* to the equation $K(q) = f$ is unique in $\mathcal{Q}$, i.e., there exists an inverse operator $K^{-1} : \mathcal{F} \mapsto \mathcal{Q}$.*

(iii) **Stability**: *Any sequence $q_1, q_2, \cdots \subset \mathcal{Q}$ satisfying $K(q_n) \to K(q)$ as $n \to \infty$ implies $q_n \to q$ as $n \to \infty$. i.e., the operator K^{-1} is continuous.*

A problem for which at least one of the three conditions above fails to hold is termed ill-posed.

Usually, the forward problems are well-posed because they are correctly modeled according to physical laws. Then the inverse problem in physical processes is usually ill-posed because it may encounter the following difficulties [29]:

(i) A given measurement is inevitably noisy. If the noisy measurement $f^\delta \notin Range(K)$, there exists no solution in $\mathcal{Q}$.

(ii) Even if K^{-1} exists and $f^\delta \in Range(K)$, it does not guarantee the solution q^δ solved by $K^{-1}f^\delta$ satisfies $q^\delta \to q$ as $f^\delta \to f$, since the operator K^{-1} may be unbounded. That is, a small error in f may produce an enormous error in q^δ.

Due to their practical importance and ill-posedness, the research of inverse problems has attracted the attention of many scholars.

1.2.3 Overview of our FDOT problem

In this section, we explain our research motivation through an intuitive argument for our FDOT problem.

Through mathematical formulation, some inverse problems will eventually be reduced to solving a Fredholm integral equation of the first kind [33]. Our FDOT problem is one of them.

Let us introduce the following example to explain the ill-posedness of our FDOT problem.

Example 1.1. (Fredholm integral equation of the first kind) *Consider the problem of solving a Fredholm integral equation of the first kind*

$$\int_a^b k(t,\, y)q(y)\mathrm{d}y = f(t), \quad c \le t \le d. \tag{1.2.2}$$

For given the kernel $k(t,\, y)$ and the function $f(t)$, the problem is to find $q(y)$. It is assumed that $f(t) \in C[c,\, d]$, $q(y) \in C[a,\, b]$, $k(t,\, y), \partial_t k(t,\, y)$ and $\partial_y k(t,\, y)$ are continuous in the rectangle $c \le t \le d, a \le y \le b$.

The problem of solving equation (1.2.2) is ill-posed because solutions may not exist for some functions $f(t) \in C[c, d]$. For example, take a function $f(t)$ that is continuous but not differentiable on $[c, d]$. With such a right-hand side, the equation cannot have a continuous solution $q(y)$ since the conditions for the kernel $k(t,\, y)$ imply that the integral in the left-hand side of (1.2.2) is differentiable with respect to the parameter t for any continuous function $q(y)$.

In this thesis, we use the TD method to consider our FDOT problem. The measurement is a temporal response function $u_m(x,\, t;\, x_s)$ satisfying (2.2.3), where x and x_s are given. Our FDOT problem aims to reconstruct μ_f from $u_m(x,\, t;\, x_s)$ via (2.2.3). Hence, if we assume $\Omega = [a,\, b]$ in (2.2.3), our problem can be reduced to (1.2.2) with

$$k(t,\, y) := D\int_0^t \mathcal{K}(x,\, y;\, t-s)\mathcal{K}(y,\, x_s;\, s)\,\mathrm{d}s, \;\; q(y) := \mu_f(y), \;\; f(t) := u_m(x,\, t;\, x_s).$$

Unfortunately, the measurement $u(x,\, t;\, x_s)$ inevitably contains noise, i.e., may not be differentiable. So, our FDOT problem is ill-posed.

The research motivation for our FDOT problem comes from the following issues:

(i) How to reduce the effect of the ill-posedness of the inverse problem on the reconstruction of μ_f?

(ii) Since the domain Ω in our problem is a half-space of three-dimensional space, reconstructing μ_f by (2.2.3) must be of large-scale numerical computations.

These two issues require to develop a mathematical analysis. There are many very classical methods, which can be easily applied to our FDOT problem. For instance, we can transform the problem into a minimization problem for a cost functional incorporated with an appropriate regularization [16, 30, 35]. Then, we can propose an iterative method to solve the minimization problem. However, we may need to discuss the computational costs of the algorithm, the selection of regularization parameters and so on. Instead of doing these, we can take advantage of the inherent advantages of the TD method as mentioned above. Namely, we applied an asymptotic analysis on the temporal response function $u_m(x, t; x_s)$ to derive the relation between the peak time and the optical path length distribution. In this way, we can have an efficient and robust reconstruction method.

Chapter 2

Mathematical Formulation to Our FDOT Problem

In this chapter, we introduce the mathematical description of FDOT and our FDOT problem. In Section 2.1, the physical processes of FDOT are described by radiative transfer equations (RTEs) in half space. Using this mathematical model to reconstruct the absorption coefficient of fluorophore, the amount of computations is so heavy to solve our FDOT problem, numerically. We introduce coupled diffusion equations, whose solution nonlinearly depends on the absorption coefficient of the fluorophore. In Section 2.2, we formulate our FDOT problem based on linearized diffusion equations. We list some related works in Section 2.3.

2.1 From RTE Model to DE Model

In this section, we introduce the radiative transfer equation (RTE) in the half-space domain, which is considered to be a general description of dissipating light in the scattering medium. Then, we give its approximation modeled by coupled diffusion equations (DEs) for the averaged fields [40].

There are several geometrical situations in realistic problems. It should be reasonable to consider the case of simple half-space geometry for potential medical applications on the body of a human, like a chest, which is significantly larger (~ 20 cm) than the size of the measurable distance ($< 3-4$ cm) in the case of the point source and detector measurement scheme. Therefore, the curvature of the measurement boundary is approximately flat. Let us define the domain (medium)

$$\Omega := \mathbb{R}^3_+ = \{x := (x_1,\, x_2,\, x_3) \,:\, (x_1,\, x_2) \in \mathbb{R}^2,\, x_3 > 0\}$$

with the boundary $\partial\Omega := \{(x_1,\, x_2,\, 0) \,:\, (x_1,\, x_2) \in \mathbb{R}^2\}$.

2.1.1 Coupled radiative transfer equations model

As shown in Figure 1.1, we inject the excitation light on $\partial\Omega$ at the first process of FDOT. The RTE can accurately describe the light propagation through strong turbid media [10, 19]. The following coupled RTEs can formulate the two physical processes (excitation and emission) in FDOT:

$$v^{-1}\partial_t\Phi_e + \theta\cdot\nabla\Phi_e + (\mu_{ae} + \mu_f(x) + \mu_{se})\Phi_e - \mu_{se}\int_{\mathbb{S}^2}\eta(\theta,\, \theta')\Phi_e(x,\, \theta',\, t)\mathrm{d}\theta' = 0, \quad (2.1.1)$$

and

$$v^{-1}\partial_t\Phi_m+\theta\cdot\nabla\Phi_m+(\mu_{am}+\mu_{sm})\Phi_m-\mu_{sm}\int_{\mathbb{S}^2}\eta(\theta,\,\theta')\Phi_m(x,\,\theta',\,t)\mathrm{d}\theta'=q_m,\quad(2.1.2)$$

where $\Phi_e(x,\,\theta,\,t)$ and $\Phi_m(x,\,\theta,\,t)$ represent the angularly resolved radiant intensity of the excitation and emission light, respectively. v is the speed of light propagation. μ_{ae} and μ_{am} are the absorption coefficients for the excitation and emission light, respectively. μ_{se} and μ_{sm} are the scattering coefficients for the excitation and emission light, respectively. $\mathbb{S}^2$ is the unit sphere. The scattering phase function, $\eta(\theta,\,\theta')$, describes the probability that a photon traveling in direction θ is scattered within the unit solid angle around the direction θ', which meets the condition $\int_{\mathbb{S}^2}\eta(\theta,\,\theta')\mathrm{d}\theta=1$.

The source term for Φ_m in (2.1.2) coming from the excitation field is specified by

$$q_m(x,\,t)=\frac{\gamma\mu_f(x)}{4\pi\ell}\int_0^t\int_{\mathbb{S}^2}\exp\left(-\frac{t-t'}{\ell}\right)\Phi_e(x,\,\theta',\,t')\mathrm{d}\theta'\mathrm{d}t',\qquad(2.1.3)$$

where $\ell>0$ is the fluorescence lifetime. $0<\gamma\leq 1$ is the quantum efficiency of the fluorescence. μ_f is the absorption coefficient of the fluorophore.

Assume that the excitation field Φ_e is generated by a point source at $x_s\in\partial\Omega$. Then the Fresnel reflection law [6, 55] leads to the boundary conditions

$$\begin{aligned}\Phi_e(x,\,\theta,\,t)&=R_e(|\theta\cdot\nu|)\Phi_e(x,\,\theta^\top,\,t)+\delta(x-x_s)\delta(\theta+\nu)\delta(t),\quad x\in\partial\Omega,&(2.1.4)\\ \Phi_m(x,\,\theta,\,t)&=R_m(|\theta\cdot\nu|)\Phi_m(x,\,\theta^\top,\,t),\quad x\in\partial\Omega&(2.1.5)\end{aligned}$$

for $\theta\cdot\nu<0$, where $\nu=(0,\,0,\,-1)$ is the unit outward normal vector. Here, $\delta(\cdot)$ is the Dirac δ-function, $\theta^\top\in\mathbb{S}^2$ is the angle symmetric to θ about ν. R_e and R_m are the Fresnel reflection coefficients. Let n_1 and n_2 with $n_1>n_2$ be the refractive indices inside and outside of the medium, respectively. Assuming that $R:=R_e=R_m$ and for the unpolarized light, there is [42]

$$R(\cos\xi):=\begin{cases}\frac{1}{2}(R_s(\cos\xi)+R_p(\cos\xi)), & 0\leq\xi\leq\xi_c,\\ 1, & \xi_c\leq\xi\leq\pi/2,\end{cases}$$

where R_s and R_p denote the Fresnel reflection of the perpendicular and parallel polarizations given as

$$R_s(\cos\xi):=\left|\frac{n_1\cos\xi-n_2\cos\xi_t}{n_1\cos\xi+n_2\cos\xi_t}\right|^2,\quad R_p(\cos\xi):=\left|\frac{n_1\cos\xi_t-n_2\cos\xi}{n_1\cos\xi_t+n_2\cos\xi}\right|^2,$$

with the critical angle $\xi_c:=\arcsin\frac{n_2}{n_1}$, while $\cos\xi_t=(1-(\frac{n_1}{n_2}\sin\xi)^2)^{1/2}$.

The initial conditions are given by

$$\begin{aligned}\Phi_e(x,\,\theta,\,0)&=0,\quad(x,\,\theta)\in\Omega\times\mathbb{S}^2,&(2.1.6)\\ \Phi_m(x,\,\theta,\,0)&=0,\quad(x,\,\theta)\in\Omega\times\mathbb{S}^2.&(2.1.7)\end{aligned}$$

From above, the physical processes (excitation and emission) in FDOT can be described by the governed equations (2.1.1)–(2.1.2), the boundary conditions (2.1.4)–(2.1.5) and the initial conditions (2.1.6)–(2.1.7).

2.1.2 Coupled diffusion equations model

Since both Φ_e and Φ_m depend on the scattering direction $\theta \in \mathbb{S}^2$, for reconstructing μ_f from measuring Φ_m over the boundary, the amount of numerical computation is huge. Hence, instead of RTEs, people use its approximation given as the following coupled diffusion equations [40]:

$$\begin{cases} \left(v^{-1}\partial_t - D\Delta + \mu_a + \mu_f(x)\right) U_e = 0, & (x,\, t) \in \Omega \times (0,\, \infty), \\ U_e = 0, & (x,\, t) \in \bar{\Omega} \times \{0\}, \\ \partial_\nu U_e + \beta U_e = w_e \delta(x - x_s)\delta(t), & x,\, x_s \in \partial\Omega,\, t \in (0,\, \infty), \end{cases} \tag{2.1.8}$$

and

$$\begin{cases} \left(v^{-1}\partial_t - D\Delta + \mu_a\right) U_m = S[\mu_f, U_e](x,\, t), & (x,\, t) \in \Omega \times (0,\, \infty), \\ U_m = 0, & (x,\, t) \in \bar{\Omega} \times \{0\}, \\ \partial_\nu U_m + \beta U_m = 0, & (x,\, t) \in \partial\Omega \times (0,\, \infty), \end{cases} \tag{2.1.9}$$

where $\partial_\nu := \nu \cdot \nabla$ is the exterior normal derivative, the physical parameters

$$D := \frac{1}{3\mu_s(1-g)}, \quad \mu_a := \mu_{ae} = \mu_{am}, \quad \mu_s := \mu_{se} = \mu_{sm},$$
$$w_e := \frac{6\mu_s(1-g)}{1 + 3\int_0^1 R(\mu)\mu^2 \, \mathrm{d}\mu}, \quad \beta := \frac{3\mu_s(1-g)}{2} \frac{1 - 2\int_0^1 R(\mu)\mu \, \mathrm{d}\mu}{1 + 3\int_0^1 R(\mu)\mu^2 \, \mathrm{d}\mu},$$

where g is called the anisotropy factor, which is defined by the average cosine of the phase function $\eta(\theta, \theta')$, and usually given by a physical parameter of the medium. The source term in (2.1.9) for U_m is

$$S[\mu_f, U_e](x, t) := \frac{\gamma \mu_f(x)}{\ell} \int_0^t e^{-\frac{t-s}{\ell}} U_e(x, s) \, \mathrm{d}s. \tag{2.1.10}$$

Here, we remark that U_m depends on μ_f, nonlinearly.

2.2 Liniarized FDOT problem for multiple point targets

In this section, we formulate our FDOT problem (inverse problem) based on the linearized diffusion equations of (2.1.8)–(2.1.10), whose solution linearly depends on μ_f.

Let u_e and u_m be excitation and emission light for the fluorescence process, respectively. These two processes can be modeled as a coupled initial boundary value problem as follows:

$$\begin{cases} \left(v^{-1}\partial_t - D\Delta + \mu_a\right) u_e = 0, & (x,\, t) \in \Omega \times (0,\, \infty), \\ u_e = 0, & (x,\, t) \in \bar{\Omega} \times \{0\}, \\ \partial_\nu u_e + \beta u_e = \delta\left(x - x_s\right)\delta(t), & (x,\, t) \in \partial\Omega \times (0,\, \infty) \end{cases} \tag{2.2.1}$$

and

$$\begin{cases} \left(v^{-1}\partial_t - D\Delta + \mu_a\right) u_m = \mu_f u_e, & (x,\, t) \in \Omega \times (0,\, \infty), \\ u_m = 0, & (x,\, t) \in \bar{\Omega} \times \{0\}, \\ \partial_\nu u_m + \beta u_m = 0, & (x,\, t) \in \partial\Omega \times (0,\, \infty), \end{cases} \tag{2.2.2}$$

where $\Omega := \mathbb{R}^3_+$. $\partial\Omega$ is the boundary of Ω. μ_a is the absorption coefficient. D is the diffusion constant. v is the speed of light in the medium. $\beta = b/D > 0$ is the Robin coefficient. $x_s \in \partial\Omega$ denotes the location of the point source where the excitation light is injected.

Remark 2.1. *The diffusion equation (2.1.8) can be linearized by assuming that $\|\mu_f\|_{L^2(\omega)} \ll \mu_a$. This assumption is quite natural in many applications. The error estimate of this linearization has been proved in [40]. Further, if we take $w_e = 1$ and $\ell \to 0$, we can get (2.2.1)–(2.2.2), where the solution u_m linearly depends on μ_f.*

The solution u_m to (2.2.2) is given as

$$\begin{aligned} &u_m(x,t;x_s) \\ &= D\int_0^t \int_\Omega \mu_f(y)\mathcal{K}(x,y;t-s)\mathcal{K}(y,x_s;s)\,\mathrm{d}y\mathrm{d}s, \quad (x,t) \in \overline{\Omega} \times (0,T). \end{aligned} \tag{2.2.3}$$

Here, $\mathcal{K}(x,y;t)$ is the Green function associated with (2.2.2),

$$\mathcal{K}(x,y;t) = \frac{ve^{-v\mu_a t}}{(4\pi vDt)^{3/2}} e^{-\frac{(x_1-y_1)^2+(x_2-y_2)^2}{4vDt}} \mathcal{K}_3(x_3,y_3;t), \tag{2.2.4}$$

where $\mathcal{K}_3$ satisfies the Robin boundary condition, which is

$$\begin{cases} \mathcal{K}_3(x_3,y_3;t) = e^{-\frac{(x_3+y_3)^2}{4vDt}} + e^{-\frac{(x_3-y_3)^2}{4vDt}} \\ \qquad\qquad -2\beta\sqrt{\pi vDt}e^{\beta(x_3+y_3)+\beta^2 vDt}\,\mathrm{erfc}\left(\frac{x_3+y_3+2\beta vDt}{\sqrt{4vDt}}\right), \\ \mathrm{erfc}(\eta) = \frac{2}{\sqrt{\pi}}\int_\eta^\infty e^{-s^2}\,\mathrm{d}s, \quad \eta \in \mathbb{R}, \end{cases}$$

where x_j denotes j-th component of the three dimensional vector x.

Now, our inverse problem (FDOT problem) is formulated as follows.

Inverse Problem: Let

$$\mu_f(x) = \sum_{j=1}^J c_j \delta(x - x_c^{(j)}), \tag{2.2.5}$$

where each $x_c^{(j)}$ is the location of an unknown target, and each unknown c_j is the absorption strength of the fluorophore committed by the target at $x_c^{(j)}$. Then, reconstruct each $x_c^{(j)}$ from the measured peak times given as

$$t_{peak}^{(n)} := t_{peak}(x_d^{(n)},\, x_s^{(n)}) = \{t : \arg\max_{t>0} u_m(x_d^{(n)},\, t;\, x_s^{(n)})\},\ n = 1,\, 2,\, \cdots,\, N,$$

where $\{x_d^{(n)},\, x_s^{(n)}\}$, $n = 1,\, 2,\, \cdots,\, N$, are N sets of source and detector points (S-D pair) located on $\partial\Omega$. For $J = 1$ and $J \geq 2$, we call μ_f a single point target and multiple point targets, respectively.

Then, the inverse problem is to reconstruct the location of small fluorophores (point targets), whose simplified system allows us to make a precise mathematical analysis.

2.3 Related works

In this section, we review some related works to our FDOT problem, which primarily focus on using the time-domain data and studying the peak time of time-domain data in the diffusion approximation models of FDOT. These studies are one kind of FDOT problem considering its data (model) types. As discussed in Chapter 1, there are other fruitful studies besides the time-domain data.

For the case of the target having a volume, there are some works reconstructing the target by using the time-domain data. In [52], the authors introduced the idea of cuboid approximation to reconstruct the shape of the target based on the linearized DE model with the fluorescence lifetime $\ell > 0$. In [54], the authors considered the inverse problem of reconstructing an ellipsoidal target or an untilted cubic-shaped target based on the linearized DE model with $\ell > 0$. Both [52] and [54] first recovered a location of the target on the measurement surface. After that, the detailed approximation of the shape of the target is reconstructed by solving an optimization problem. The paper [14] reduced the inverse problem of choosing the best data features. The data feature problem has been reinterpreted from the point of view of the projection of the data onto some basis functions and a wavelet approach has been proposed. Some reconstruction frameworks are proposed based on a formulation of the three-dimensional finite element method [20, 56].

For assuming the target is a point target, the paper [18] considered using a minimal number of S-D pairs to reconstruct the location of the point target. By a local analysis, they gave a reconstruction algorithm using the Levenberg-Marquardt method and proved its local Lipschitz stability. For their reconstruction, they need a good initial guess.

There are several studies on the peak time of the time-domain data. In [22, 23], they reconstructed the depth of the point target with the homogeneous Neumann boundary condition by numerically calculating the peak time. However, their analysis was based on an empirical way using numerical simulation of the peak time without analytical investigations yielding a mathematical formula of the peak time. In [17], they first considered the expressions of the approximate peak time of time-domain data for Dirichlet, Neumann and Robin boundary conditions based on the asymptotic formulae of the solution of the linearized DE model. However, the expression under the Robin boundary condition only considers an extreme condition with a lack of verification for applying our actual inverse problem.

In general, FDOT is an ill-posed inverse problem discussed in enormous studies, and it is known that the initial guess and the regularization to confine the problem are ones of crucial points to solve FDOT [5]. To improve the image quality, we refer to [8, 25] for L^p regularization, [1, 7] for total variation regularization and [24, 34, 41] for sparsity regularization.

For more extended studies of FDOT, we can refer to the monographs [31] and [32], which introduce the principles and applications of DOT and FDOT, respectively. Concerning diffusion approximation models to describe the physical processes of FDOT, we refer to [3, 6, 40] and the references therein.

Chapter 3

Asymptotic Formulae of Solution for Single Point Target

In this chapter, we begin with studying asymptotic formulae of the solution u_m to (2.2.2) and its time-derivative solution $\partial_t u_m$ in the case of a single point target, i.e., $J = 1$ in (2.2.5). After that, we provide some numerical verifications to examine the asymptotic behaviors.

For $J = 1$ in (2.2.5), we suppressed the superscript (j) of $x_c^{(j)}$ and the subscript j of c_j, i.e.,

$$\mu_f(x) = c\,\delta(x - x_c).$$

Then, for any given $x_d, x_s \in \partial\Omega$, u_m of (2.2.3) becomes

$$u_m(x_d, t; x_s) = \frac{ce^{-v\mu_a t}}{16\pi^3 D^2 v} \int_0^t \big((t-s)s\big)^{-\frac{3}{2}} e^{-\frac{|x_d - x_c|^2}{4vD(t-s)}} e^{-\frac{|x_s - x_c|^2}{4vDs}} \times \hat{\mathcal{K}}_3(x_{c_3}; t-s)\hat{\mathcal{K}}_3(x_{c_3}; s)\,\mathrm{d}s, \qquad (3.0.1)$$

where

$$\hat{\mathcal{K}}_3(x_{c_3}; t) := 1 - \beta\sqrt{\pi v D t}\, \exp\left(\left(\frac{x_{c_3} + 2\beta v D t}{\sqrt{4vDt}}\right)^2\right) \operatorname{erfc}\left(\frac{x_{c_3} + 2\beta v D t}{\sqrt{4vDt}}\right).$$

Here, $|x|^2 = x_1^2 + x_2^2 + x_3^2$ for $x = (x_1, x_2, x_3) \in \mathbb{R}^3$.

The rest of this chapter is organized as follows. We first derive non-dimensional asymptotic formulae of the solution defined by (3.0.1) and its time-derivative in Section 3.1. Then, dimensional asymptotic formulae of the solution defined by (3.0.1) and its time-derivative are established in Section 3.2. The effectiveness of the asymptotic formulae is demonstrated by using some numerical verifications in Section 3.3.

3.1 Non-dimensional asymptotic formulae of solution

In this section, we give a non-dimensional asymptotic analysis of solution defined by (3.0.1). The motivation for doing this is to equally handle all the parameters inside the solution without concerning their physical dimension,

Let us define non-dimensional lengths and time as follows:

$$\rho = \frac{x}{D},\ \rho_d = \frac{x_d}{D},\ \rho_s = \frac{x_s}{D},\ \rho_c = \frac{x_c}{D},\ \tau = \frac{vt}{D},\ b = \beta D,$$

and

$$\tilde{u}_m(\rho, \tau; \rho_s) := u_m(x, t; x_s), \quad \tilde{\mathcal{K}}_3(\rho_3; \tau) := \hat{\mathcal{K}}_3(x_{c_3}; t).$$

Then, $\tilde{u}_m$ is written as follows (see [18, Lemma 2.1]).

Lemma 3.1. *For any given $\rho_d,\ \rho_s \in \partial\Omega$,*

$$\tilde{u}_m(\tau) = C(\tau)\tau^{-2}\big(I_{\lambda_{d,s}}(\tau) + I_{\lambda_{s,d}}(\tau)\big), \tag{3.1.1}$$

where

$$C(\tau) := \frac{cv\exp\left(-\mu_a D\tau\right)}{16\pi^3 D^4},\ \lambda_d := \frac{|\rho_d-\rho_c|^2}{4\tau},\ \lambda_s := \frac{|\rho_s-\rho_c|^2}{4\tau},\ \lambda_c := \frac{\rho_{c3}^2}{4\tau}, \tag{3.1.2}$$

$$I_{\lambda_{d,s}}(\tau) := \int_0^{1/2} \big((1-\sigma)\sigma\big)^{-\frac{3}{2}} e^{-\frac{\lambda_d}{(1-\sigma)\sigma}} e^{-\frac{\lambda_s-\lambda_d}{1-\sigma}} \tilde{\mathcal{K}}_3(\lambda_c;1-\sigma)\tilde{\mathcal{K}}_3(\lambda_c;\sigma)\,\mathrm{d}\sigma, \tag{3.1.3}$$

and $I_{\lambda_{s,d}}(\tau)$ is defined by switching the role of λ_d and λ_s in $I_{\lambda_{d,s}}(\tau)$. Here, $\tilde{\mathcal{K}}_3$ is given as

$$\tilde{\mathcal{K}}_3(\lambda_c;\sigma) = 1 - \frac{b\sqrt{\tau}\sigma}{\sqrt{\lambda_c}+b\sqrt{\tau}\sigma}\sqrt{\pi}\, z_\sigma \exp\left(z_\sigma^2\right)\operatorname{erfc}\left(z_\sigma\right) \tag{3.1.4}$$

with $z_\sigma = \frac{\sqrt{\lambda_c}+b\sqrt{\tau}\sigma}{\sqrt{\sigma}}$ for $0<\sigma<1$.

In the next Theorem 3.1, we obtain the asymptotic formula of $\tilde{u}_m$ based on the asymptotic of $\tilde{\mathcal{K}}_3$ as $\rho_{c3}\to\infty$.

Theorem 3.1. *Let $\rho_d,\ \rho_s \in \partial\Omega$. Assume that*

$$\Big||\rho_d-\rho_c|^2 - |\rho_s-\rho_c|^2\Big| \le C\tau \quad \text{for some} \quad C>0. \tag{3.1.5}$$

Then, $\tilde{u}_m$ of (3.1.1) satisfies

$$\tilde{u}_m(\tau) = \tilde{u}_m^a(\tau) + O\left(\tilde{u}_m^a(\tau)\rho_{c3}^{-1}\right) \tag{3.1.6}$$

as $\rho_{c3}\to\infty$, where

$$\begin{aligned}&\tilde{u}_m^a(\tau)\\ :=&\sqrt{\pi}C(\tau)\tau^{-\frac{3}{2}}\left(\frac{2}{|\rho_d-\rho_c|}+\frac{2}{|\rho_s-\rho_c|}\right)e^{-\frac{|\rho_d-\rho_c|^2+|\rho_s-\rho_c|^2}{2\tau}}\left(\frac{\rho_{c3}}{\rho_{c3}+b\tau}\right)^2.\end{aligned} \tag{3.1.7}$$

Proof. The proof of Theorem 3.1 can be done in a similar way as in [18, Corollary 2.3]. For readers' convenience, we provide the proof here in detail. By (3.1.4) and

$$\begin{aligned}\exp\left(z^2\right)\operatorname{erfc}\left(z\right) &= \frac{2}{\sqrt{\pi}}\exp\left(z^2\right)\int_z^\infty \exp\left(-s^2\right)\mathrm{d}s\\ &= \frac{1}{\sqrt{\pi}z} - \frac{\exp\left(z^2\right)}{\sqrt{\pi}}\int_z^\infty s^{-2}\exp\left(-s^2\right)\mathrm{d}s, \quad z>0,\end{aligned}$$

we obtain

$$\tilde{\mathcal{K}}_3(\tau,\rho_{c3};\sigma) = \frac{\rho_{c3}}{\rho_{c3}+2b\sigma\tau} + r(\sigma),$$

where

$$r(\sigma) := b\sqrt{\tau\sigma}\exp\left(z_\sigma^2\right)\int_{z_\sigma}^\infty s^{-2}\exp\left(-s^2\right)\mathrm{d}s.$$

This implies

$$\left|\tilde{\mathcal{K}}_3(\tau,\rho_{c_3};\sigma)-\frac{\rho_{c_3}}{\rho_{c_3}+2b\sigma\tau}\right|=|r(\sigma)|\le Cz_\sigma^{-3}=O\left(\rho_{c_3}^{-3}\right) \tag{3.1.8}$$

as $\rho_{c_3}\to\infty$. Set

$$e^{-\frac{\lambda_s-\lambda_d}{1-\sigma}}\tilde{\mathcal{K}}_3(\tau,\rho_{c_3};\sigma)\tilde{\mathcal{K}}_3(\tau,\rho_{c_3};1-\sigma)=g(\tau;\sigma)+l(\tau;\sigma), \tag{3.1.9}$$

where

$$\begin{aligned} l(\tau;\sigma)&:=e^{-\frac{\lambda_s-\lambda_d}{1-\sigma}}\left(\frac{\rho_{c_3}}{\rho_{c_3}+2b\sigma\tau}r(1-\sigma)+\frac{\rho_{c_3}}{\rho_{c_3}+2b(1-\sigma)\tau}r(\sigma)+r(\sigma)r(1-\sigma)\right),\\ g(\tau;\sigma)&:=e^{-\frac{\lambda_s-\lambda_d}{1-\sigma}}\frac{\rho_{c_3}}{\rho_{c_3}+2b\sigma\tau}\frac{\rho_{c_3}}{\rho_{c_3}+2b(1-\sigma)\tau}. \end{aligned} \tag{3.1.10}$$

Based on (3.1.9), we split $I_{\lambda_{d,s}}$ of (3.1.3) into

$$I_{\lambda_{d,s}}(\tau):=I_d^a(\tau)+R_d^r(\tau), \tag{3.1.11}$$

where

$$\begin{aligned} I_d^a(\tau)&:=\int_0^{1/2}\big((1-\sigma)\sigma\big)^{-\frac{3}{2}}e^{-\frac{\lambda_d}{(1-\sigma)\sigma}}g(\tau;\sigma)\,\mathrm{d}\sigma,\\ R_d^r(\tau)&:=\int_0^{1/2}\big((1-\sigma)\sigma\big)^{-\frac{3}{2}}e^{-\frac{\lambda_d}{(1-\sigma)\sigma}}l(\tau;\sigma)\,\mathrm{d}\sigma. \end{aligned} \tag{3.1.12}$$

By (3.1.8), we note that R_d^r is a remainder term of $I_{\lambda_{d,s}}$ in (3.1.11) as $\rho_{c_3}\to\infty$. Further, we split I_d^a by applying the Taylor theorem to g of (3.1.10) at the center $\sigma=1/2$. Then, we obtain

$$g(\tau;\sigma)=g(\tau;1/2)+\partial_\sigma g(\tau,\theta_\sigma)\left(\sigma-\frac{1}{2}\right)\quad\text{with}\quad 0<\theta_\sigma<1/2,$$

and

$$I_d^a(\tau):=\int_0^{1/2}\big((1-\sigma)\sigma\big)^{-\frac{3}{2}}e^{-\frac{\lambda_d}{(1-\sigma)\sigma}}\left[g(\tau;1/2)+\partial_\sigma g(\tau,\theta)\left(\sigma-\frac{1}{2}\right)\right]\mathrm{d}\sigma. \tag{3.1.13}$$

We decompose $I_d^a(\tau)$ into $I_d^a(\tau)=I_d(\tau)+R_d(\tau)$, where

$$I_d(\tau):=\int_0^{1/2}\big((1-\sigma)\sigma\big)^{-\frac{3}{2}}e^{-\frac{\lambda_d}{(1-\sigma)\sigma}}g(\tau;1/2)\,\mathrm{d}\sigma,$$

and

$$R_d(\tau):=\int_0^{1/2}\big((1-\sigma)\sigma\big)^{-\frac{3}{2}}e^{-\frac{\lambda_d}{(1-\sigma)\sigma}}\partial_\sigma g(\tau,\theta)\left(\sigma-\frac{1}{2}\right)\mathrm{d}\sigma.$$

By change of a variable, we obtain

$$\begin{aligned} I_d(\tau)&=g(\tau;1/2)\int_0^\infty \xi^{-\frac{1}{2}}e^{-\lambda_d(4+\xi)}\,\mathrm{d}\xi=g(\tau;1/2)\sqrt{\pi}\lambda_d^{-\frac{1}{2}}e^{-4\lambda_d}\\ &=\frac{2\sqrt{\pi\tau}}{|\rho_d-\rho_c|}e^{-\frac{|\rho_d-\rho_c|^2+|\rho_s-\rho_c|^2}{2\tau}}\left(\frac{\rho_{c_3}}{\rho_{c_3}+b\tau}\right)^2, \end{aligned}$$

which determines the asymptotics in (3.1.7). By (3.1.5), we have $|\partial_\sigma g(\tau;\sigma)| < C$, which implies

$$
\begin{aligned}
|R_d(\tau)| &= \left| \int_0^{1/2} \big((1-\sigma)\sigma\big)^{-\frac{3}{2}} e^{-\frac{\lambda_d}{(1-\sigma)\sigma}} \partial_\sigma g(\tau,\theta) \left(\sigma - \frac{1}{2}\right) \mathrm{d}\sigma \right| \\
&\le C \int_0^\infty e^{-\lambda_d(4+\zeta)} (\zeta+4)^{-\frac{1}{2}} \,\mathrm{d}\zeta \\
&\le C\lambda_d^{-1} e^{-4\lambda_d} \quad \text{for} \quad \tau > 0. \qquad (3.1.14)
\end{aligned}
$$

This implies R_d is a remainder term of I_d^a in (3.1.13), precisely,

$$C(\tau)\tau^{-2}|R_d(\tau)| = C(\tau)\tau^{-2} O\left(\lambda_d^{-1} e^{-2(\lambda_d+\lambda_s)}\right) = O\left(\tilde{u}_m^a(\tau)\rho_{c_3}^{-1}\right)$$

as $\rho_{c_3} \to \infty$. Then, by (3.1.1), (3.1.7), (3.1.11) and (3.1.13)-(3.1.14), we obtain

$$
\begin{aligned}
\tilde{u}_m(\tau) &= C(\tau)\tau^{-2}\big(I_{\lambda_{d,s}}(\tau) + I_{\lambda_{s,d}}(\tau)\big) \\
&= C(\tau)\tau^{-2}\big([I_d^a(\tau) + R_d^r(\tau)] + [I_s^a(\tau) + R_s^r(\tau)] \big) \\
&= C(\tau)\tau^{-2}\left[I_d(\tau) + I_s(\tau)\right] + C(\tau)\tau^{-2} O\Big(R_d(\tau) + R_s(\tau)\Big) \\
&= \tilde{u}_m^a(\tau) + O\left(\tilde{u}_m^a(\tau)\rho_{c_3}^{-1}\right) \qquad (3.1.15)
\end{aligned}
$$

as $\rho_{c_3} \to \infty$. This implies (3.1.6), and the proof of Theorem 3.1 is complete. □

Remark 3.1. *In Theorem 3.1, the error between $\tilde{u}_m$ of (3.1.6) and its asymptotic expansion is estimated by $\rho_{c_3}^{-1}$. This is the same as the case $b = 0$, i.e., $\beta = 0$ as in [18, Corollary 2.3]. However, a new feature here is that there is a factor*

$$\left(\frac{\rho_{c_3}}{\rho_{c_3} + b\tau}\right)^2 \qquad (3.1.16)$$

in (3.1.7), which is an effect coming from the boundary. We will show the effect of Robin coefficient β by using some numerical verifications shown in Subsection 3.3.2.

In the next Theorem 3.2, we obtain the asymptotic formula of $\partial_\tau \tilde{u}_m$ under the condition

$$
\begin{aligned}
&\Big| |\rho_d - \rho_c|^2 - |\rho_s - \rho_c|^2 \Big| \le C_1 \tau \rho_{c_3}^{-1} \quad \text{for some } C_1 > 0, \\
&C_2\rho_{c_3} \le \tau \le C_3\rho_{c_3} \quad \text{for some } C_2,\ C_3 > 0.
\end{aligned} \qquad (3.1.17)
$$

Theorem 3.2. *Let $\rho_d,\ \rho_s \in \partial\Omega$. Assume (3.1.17). Then, $\tilde{u}_m$ of (3.1.1) satisfies*

$$\partial_\tau \tilde{u}_m(\tau) = \partial_\tau \tilde{u}_m^a(\tau) + O\left(\tilde{u}_m^a(\tau)\rho_{c_3}^{-3/2}\right), \qquad (3.1.18)$$

as $\rho_{c_3} \to \infty$, where $\tilde{u}_m^a(\tau)$ is as in (3.1.7). Here,

$$
\begin{aligned}
&\partial_\tau \tilde{u}_m^a(\tau) = \tilde{P}_3(\tau)\tilde{u}_m^a(\tau), \\
&\tilde{P}_3(\tau) := -\mu_a D - \frac{3}{2}\tau^{-1} + \frac{|\rho_d - \rho_c|^2 + |\rho_s - \rho_c|^2}{2}\tau^{-2} - \frac{2b}{\rho_{c_3} + b\tau}.
\end{aligned} \qquad (3.1.19)
$$

Proof. The proof of Theorem 3.2 can be done in a similar way as in Theorem 3.1. The only difference occurs when we compute $\partial_\sigma g$, where g is as in (3.1.10). By (3.1.17), we obtain

$$\left|\partial_\sigma e^{-\frac{\lambda_s-\lambda_d}{1-\sigma}}\right| \le C\left|\lambda_d-\lambda_s\right| e^{-\frac{\lambda_s-\lambda_d}{1-\sigma}} \le C\rho_{c_3}^{-1}$$

for $0<\sigma<1/2$, which yields

$$|\partial_\sigma g(\tau;\sigma)| = \left|\partial_\sigma\left(e^{-\frac{\lambda_s-\lambda_d}{1-\sigma}}\frac{\rho_{c_3}}{\rho_{c_3}+2b\sigma\tau}\frac{\rho_{c_3}}{\rho_{c_3}+2b(1-\sigma)\tau}\right)\right| \le C\rho_{c_3}^{-1} \tag{3.1.20}$$

for $0<\sigma<1/2$. This implies

$$\begin{aligned}|R_d(\tau)| &= \left|\int_0^{1/2}\big((1-\sigma)\sigma\big)^{-\frac{3}{2}} e^{-\frac{\lambda_d}{(1-\sigma)\sigma}}\partial_\sigma g(\tau,\theta)\left(\sigma-\frac{1}{2}\right)\mathrm{d}\sigma\right| \\ &\le C\rho_{c_3}^{-1}\int_0^\infty e^{-\lambda_d(4+\zeta)}(\zeta+4)^{-\frac{1}{2}}\,\mathrm{d}\zeta = O\left(\rho_{c_3}^{-1}\lambda_d^{-1}e^{-4\lambda_d}\right)\end{aligned} \tag{3.1.21}$$

as $\rho_{c_3}\to\infty$. By (3.1.17), we have

$$\left|\partial_\tau e^{-\frac{\lambda_d}{(1-\sigma)\sigma}}\right| \le C\frac{|\rho_d-\rho_c|^2}{\tau^2}e^{-\frac{\lambda_d}{(1-\sigma)\sigma}} \le Ce^{-\frac{\lambda_d}{(1-\sigma)\sigma}} \quad \text{for} \quad \rho_{c_3}>0,$$

which yields from (3.1.20) that

$$\begin{aligned}&|\partial_\tau R_d(\tau)| \\ \le&\left|\int_0^{1/2}\big((1-\sigma)\sigma\big)^{-\frac{3}{2}}\left[\partial_\tau e^{-\frac{\lambda_d}{(1-\sigma)\sigma}}\right]\partial_\sigma g(\tau,\theta)\left(\sigma-\frac{1}{2}\right)\mathrm{d}\sigma\right| \\ &+\left|\int_0^{1/2}\big((1-\sigma)\sigma\big)^{-\frac{3}{2}}e^{-\frac{\lambda_d}{(1-\sigma)\sigma}}\left[\partial_\tau\partial_\sigma g(\tau,\theta)\right]\left(\sigma-\frac{1}{2}\right)\mathrm{d}\sigma\right| \\ \le& C\rho_{c_3}^{-1}\int_0^{1/2}\big((1-\sigma)\sigma\big)^{-\frac{3}{2}}e^{-\frac{\lambda_d}{(1-\sigma)\sigma}}\left|\sigma-\frac{1}{2}\right|\mathrm{d}\sigma = O\left(\rho_{c_3}^{-1}\lambda_d^{-1}e^{-4\lambda_d}\right)\end{aligned} \tag{3.1.22}$$

as $\rho_{c_3}\to\infty$. By (3.1.17), (3.1.21) and (3.1.22), we obtain

$$\begin{aligned}&\left|\partial_\tau\left[C(\tau)\tau^{-2}R_d(\tau)\right]\right| \\ \le& C\left(\left|\partial_\tau[C(\tau)]\tau^{-2}R_d(\tau)\right|+\left|C(\tau)\tau^{-3}R_d(\tau)\right|+\left|C(\tau)\tau^{-2}\partial_\tau R_d(\tau)\right|\right) \\ =& C(\tau)\tau^{-2}\Big(O\left(R_d(\tau)\right)+O\left(\partial_\tau R_d(\tau)\right)\Big) \\ =& C(\tau)\tau^{-2}O\Big(\rho_{c_3}^{-1}\lambda_d^{-1}e^{-4\lambda_d}\Big) \\ =& O\left(\tau^{-\frac{1}{2}}\lambda_d^{-1}\tilde{u}_m^a(\tau)\right) = O\left(\rho_{c_3}^{-3/2}\tilde{u}_m^a(\tau)\right)\end{aligned} \tag{3.1.23}$$

as $\rho_{c_3}\to\infty$. In a similar way as in (3.1.15) and (3.1.23), we obtain

$$\begin{aligned}\partial_\tau\tilde{u}_m(\tau) &= \partial_\tau\Big(C(\tau)\tau^{-2}\big[I_{\lambda_{d,s}}(\tau)+I_{\lambda_{s,d}}(\tau)\big]\Big) \\ &= \partial_\tau\Big(C(\tau)\tau^{-2}\left[I_d^a(\tau)+I_s^a(\tau)\right]\Big)+\partial_\tau\Big(C(\tau)\tau^{-2}\left[R_d^r(\tau)+R_s^r(\tau)\right]\Big) \\ &= \partial_\tau\tilde{u}_m^a(\tau)+O\left(\partial_\tau\Big[C(\tau)\tau^{-2}[R_d(\tau)+R_s(\tau)]\Big]\right) \\ &= \tilde{P}_3(\tau)\tilde{u}_m^a(\tau)+O\left(\rho_{c_3}^{-3/2}\tilde{u}_m^a(\tau)\right)\end{aligned}$$

as $\rho_{c_3} \to \infty$, where $\tilde{P}_3$ is as in (3.1.19). □

3.2 Dimensional asymptotic formulae of solution

In this section, we are going to rewrite the asymptotic formulae of the non-dimensional solution $\tilde{u}_m$ (see Theorem 3.1) and its time-derivative $\partial_\tau \tilde{u}_m$ (see Theorem 3.2) into the dimensional case.

Recall the change of variables

$$x = D\rho,\ x_d = D\rho_d,\ x_s = D\rho_s,\ x_c = D\rho_c,\ t = \frac{Dt}{v},\ b = \beta D. \tag{3.2.1}$$

We easily obtain the following dimensional asymptotic formula of the solution u_m as the depth x_{c_3} of the target goes to infinity.

Theorem 3.3. *For the original solution u_m, (3.1.5), (3.1.6) and (3.1.7) are given as follows. Let $x_d,\ x_s \in \partial\Omega$, and assume that*

$$\left| |x_d - x_c|^2 - |x_s - x_c|^2 \right| \leq Ct \quad \text{for some} \quad C > 0. \tag{3.2.2}$$

Then, u_m satisfies

$$u_m(t) = u_m^a(t) + O\left(u_m^a(t) x_{c3}^{-1}\right) \ \text{ as } \ x_{c3} \to \infty, \tag{3.2.3}$$

where

$$\begin{aligned} u_m^a(t) :=& \frac{c \exp\left(-\mu_a v t\right)}{8\pi^{\frac{5}{2}} v^{\frac{1}{2}} D^{\frac{3}{2}}} \left(\frac{1}{|x_d - x_c|} + \frac{1}{|x_s - x_c|} \right) t^{-\frac{3}{2}} \\ & \times \exp\left(-\frac{|x_d - x_c|^2 + |x_s - x_c|^2}{2vDt} \right) \left(\frac{x_{c3}}{x_{c3} + \beta v D t} \right)^2 . \end{aligned} \tag{3.2.4}$$

It should be mentioned that the condition (3.2.2) is natural. Since the domain Ω is the upper half space and the location x_d of the detector and the location x_s of the source are on the boundary $\partial\Omega$, the left hand side of the condition (3.2.2) will become small when we set the distance between x_d and x_s is small and the depth x_{c_3} of the target is large.

Using the changes (3.2.1) again, we can derive the following asymptotic formula of time-derivative $\partial_t u_m$ as the depth x_{c_3} of the target goes to infinity.

Theorem 3.4. *For the original solution u_m, (3.1.17) and (3.1.18) are given as follows. Let $x_d,\ x_s \in \partial\Omega$, and assume*

$$\begin{aligned} &\left| |x_d - x_c|^2 - |x_s - x_c|^2 \right| \leq C_1 \frac{t}{x_{c3}} \quad \text{for some } \ C_1 > 0, \\ &C_2 x_{c3} \leq t \leq C_3 x_{c3} \quad \text{for some } \ C_2,\ C_3 > 0. \end{aligned} \tag{3.2.5}$$

Then, u_m satisfies

$$\partial_t u_m(t) = \partial_t u_m^a(t) + O\left(u_m^a(t) x_{c3}^{-3/2}\right) \ \text{ as } \ x_{c3} \to \infty, \tag{3.2.6}$$

where $u_m^a(t)$ is as in (3.2.4). Here,

$$\begin{aligned}
&\partial_t u_m^a(t) = P_3(t) u_m^a(t), \\
&P_3(t) := -\mu_a v - \frac{3}{2} t^{-1} + \frac{|x_d - x_c|^2 + |x_s - x_c|^2}{2vD} t^{-2} - \frac{2\beta v D}{x_{c3} + \beta v D t}.
\end{aligned} \tag{3.2.7}$$

From Theorem 3.4, we derived a nice asymptotic formula of $\partial_t u_m$, because its dominant term is in the form of a polynomial multiplied by the asymptotic solution u_m^a. In the following, we make a minor remark on the constraint (3.2.5) and the motivation of giving Theorem 3.4.

Remark 3.2.

(i) *Due to the constraint (3.2.5), as the depth x_{c3} increases the time t also increases. Roughly speaking, the rate of increase in x_{c3} and the time t is the same as $x_{c3} \to \infty$. In fact, we pay more attention to the asymptotic formula at t^*, where t^* is the zero of $\partial_t u_m(t) = 0$. From **Verfication II** given in Section 4.2, we will observe the fact that the time t^* increases as x_{c3} increases.*

(ii) *The motivation for discussing the asymptotic formula of the time-derivative $\partial_t u_m$ is from the physical experience. That is, the process $u_m(t)$ has a unique maximum value to t. We will show this fact by numerical experiments in the next section. But it is difficult to directly prove this fact by using the analytical solution (3.0.1).*

3.3 Numerical verification

In this section, we verify the effectiveness of the asymptotic solution u_m^a by studying some numerical examples. Also, the effect of Robin coefficient β will be numerically demonstrated. These numerical experiments will clearly demonstrate the importance of our asymptotic analysis.

3.3.1 Comparison of exact and approximate solutions

In this subsection, we numerically verify the effectiveness of the asymptotic solution u_m^a given by (3.2.4) compared with the exact solution u_m as the depth x_{c3} increases. Here, we use the numerical solution, denoted by u_m^n, instead of the exact solution.

The numerical solution is obtained by calculating the exact analytical solution (3.0.1) through numerical integration. From (3.0.1), there is no singularity in numerically calculating $u_m(x_d, t; x_c)$ for $x_d \in \partial\Omega$. Let the integral interval $(0, t)$ be divide into J equal subintervals with step size Δt with grid points

$$t_j = j \cdot \Delta t, \quad j = 0, 1, \cdots, J.$$

For fixed detector point x_d, we use the right rectangle method to calculate an approximate estimate for the area under the curve $u_m(x_d, t; x_c)$ by drawing many rectangles with very small width adjacent to each other between the graph of the function $u_m(x_d, t; x_c)$ and the t axis.

It is obvious to see that $u_m^n(x_d,\, t_0;\, x_s) = 0$. For each grid points t_j, $j = 1,\, 2,\, \cdots,\, J$, the numerical solution $u_m^n(x_d,\, t_j;\, x_s)$ can be computed by

$$u_m^n(x_d,\, t_j;\, x_s) = \frac{\Delta t c e^{-v\mu_a t_j}}{16\pi^3 D^2 v} \sum_{j'=1}^{j} \Big[\big((t_j - s_{j'})s_{j'}\big)^{-\frac{3}{2}} e^{-\frac{|x_d - x_c|^2}{4vD(t_j - s_{j'})}} e^{-\frac{|x_s - x_c|^2}{4vDs_{j'}}} \times \hat{\mathcal{K}}_3(x_{c_3};\, t_j - s_{j'}) \hat{\mathcal{K}}_3(x_{c_3};\, s_{j'}) \Big], \tag{3.3.1}$$

where $s_{j'} = j' \cdot \Delta t$ and

$$\hat{\mathcal{K}}_3(x_{c_3};\, t) := 1 - \beta\sqrt{\pi v D t}\, \exp\left(\left(\frac{x_{c_3} + 2\beta v D t}{\sqrt{4vDt}} \right)^2 \right) \operatorname{erfc}\left(\frac{x_{c_3} + 2\beta v D t}{\sqrt{4vDt}} \right).$$

Here, $|x|^2 = x_1^2 + x_2^2 + x_3^2$ for $x = (x_1, x_2, x_3) \in \mathbb{R}^3$.

For the asymptotic solution, we compute the value $u_m^a(x_d,\, t_j;\, x_s)$ at each grid point t_j, $j = 0,\, 1,\, \cdots,\, J$, by (3.2.4).

To show the approximation of the asymptotic solution given in (3.2.3), we will show the changes of the error $Err := Err(x_d,\, x_s,\, x_c)$ between the numerical solution and the asymptotic solution as the depth x_{c_3} increases, where the error is computed by

$$Err = \sum_{j=0}^{J} \left| u_m^n(x_d,\, t_j;\, x_s) x_{c_3}^{-1} - u_m^a(x_d,\, t_j;\, x_s) x_{c_3}^{-1} \right|. \tag{3.3.2}$$

In (3.2.4) and (3.3.1), we set the physical parameters as following:

$$v = 0.219\,\text{mm/ps}, \quad D = 1/3\,\text{mm}, \quad \mu_a = 0.1\,\text{mm}^{-1}, \quad \beta = 0.5493\,\text{mm}^{-1}, \tag{3.3.3}$$

which are typical values in biological tissues.

For fixed x_d and x_s, we numerically calculate u_m^a and u_m^n for different location x_c of target by (3.2.4) and (3.3.1), respectively. The numerical results are shown in Table 3.1 and Figures 3.1–3.2.

TABLE 3.1: Error between $u_m^n(x_d,\, t;\, x_s)$ and $u_m^a(x_d,\, t;\, x_s)$ defined by (3.3.2) for different x_c.

$(x_d,\, x_s)$	x_c	Err	Figure
$\big((14,10,0),(6,10,0)\big)$	$(10,10,10)$	2.3739e-12	Figure 3.1 (a)
	$(10,10,20)$	3.9208e-18	Figure 3.1 (b)
	$(10,10,30)$	1.4695e-23	Figure 3.1 (c)
	$(10,10,40)$	6.1498e-29	Figure 3.1 (d)
$\big((14,10,0),(6,10,0)\big)$	$(15,15,10)$	3.5653e-13	Figure 3.2 (a)
	$(15,15,20)$	1.3741e-18	Figure 3.2 (b)
	$(15,15,30)$	6.9087e-24	Figure 3.2 (c)
	$(15,15,40)$	3.2834e-29	Figure 3.2 (d)

It is easy to observe that there are the following advantages from the numerical results:

(i) The error defined by (3.3.2) between the numerical solution u_m^n and the asymptotic solution u_m^a decreases as the depth x_{c_3} increases.

(ii) The profiles of the numerical solution u_m^n and the asymptotic solution u_m^a are the same. More precisely, the value of both u_m^n and u_m^a increases from 0 to

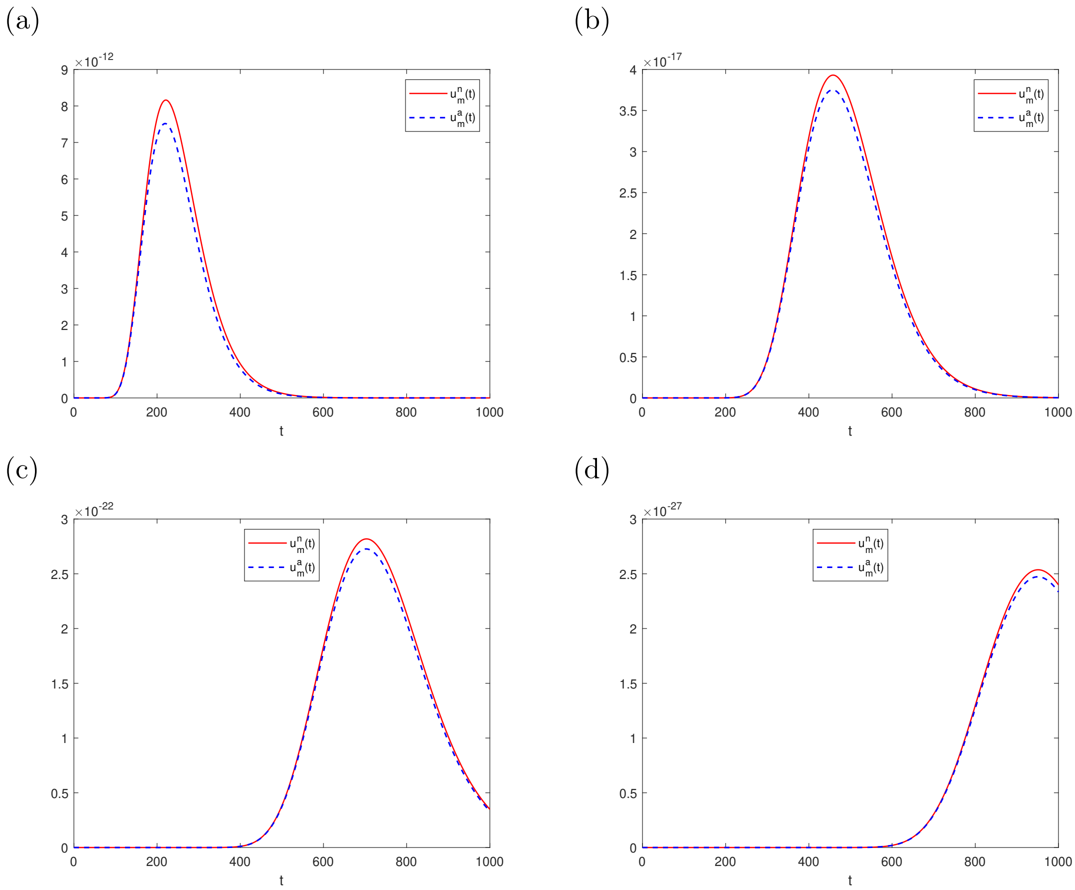

FIGURE 3.1: Numerical solution $u_m^n(x_d,\, t;\, x_s)$ and asymptotic solution $u_m^a(x_d,\, t;\, x_s)$ for $\{x_d,\, x_s\} = \big\{(14,\, 10,\, 0),\, (6,\, 10,\, 0)\big\}$ and different x_c: (a) $x_c = (10,\, 10,\, 10)$, (b) $x_c = (10,\, 10,\, 20)$, (c) $x_c = (10,\, 10,\, 30)$, (d) $x_c = (10,\, 10,\, 40)$

.

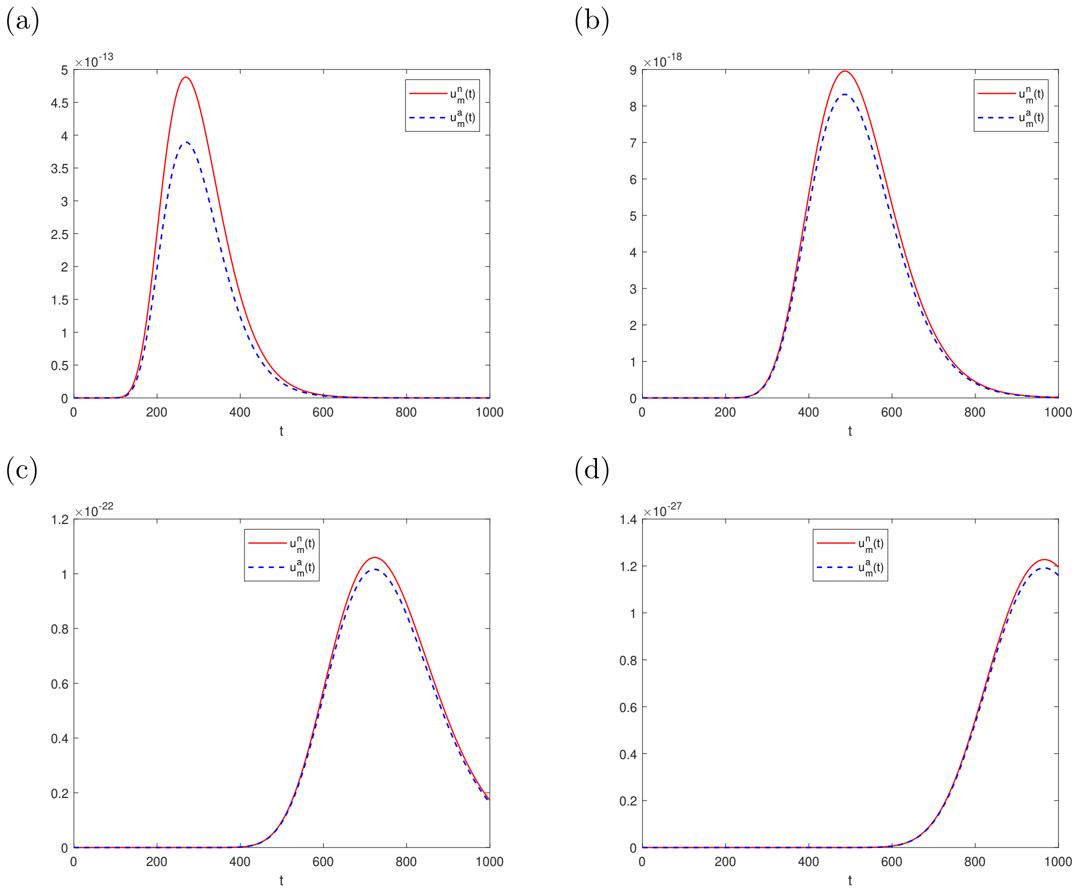

FIGURE 3.2: Numerical solution $u_m^n(x_d, t; x_s)$ and asymptotic solution $u_m^a(x_d, t; x_s)$ for $\{x_d, x_s\} = \{(14, 10, 0), (6, 10, 0)\}$ and different x_c: (a) $x_c = (15, 15, 10)$, (b) $x_c = (15, 15, 20)$, (c) $x_c = (15, 15, 30)$, (d) $x_c = (15, 15, 40)$

.

the maximum over time t and then gradually decreases to 0. There is only one maximum in the whole process.

(iii) For each fixed $\{x_d, x_s\}$ and x_c, although the maximum of u_m^n is obviously different from the maximum of u_m^a, the time t when they reach the maximum value is almost the same.

Remark 3.3. *In this subsection, we will temporarily abandon verifying the asymptotic formula of $\partial_t u_m$ shown in Theorem 3.4. In Chapter 4, we will introduce the definition of approximate peak time based on the result of Theorem 3.4. After this, a more detailed discussion about the approximate peak time will be given.*

3.3.2 Effected by Robin coefficient β

In this subsection, the effect of Robin coefficient β on the solution is verified by using some numerical examples, which will ensure that the asymptotic solution obtained in this chapter is suitable for any β.

We continue a similar discussion as in the previous subsection by calculating the numerical solution $u_m^n(x_d, t; \beta)$ and the asymptotic solution $u_m^a(x_d, t; \beta)$ for different β. Here we write $u_m^n(x_d, t) = u_m^n(x_d, t; \beta)$ to clarify that $u_m^n(x_d, t)$ depends on β, as well as $u_m^a(x_d, t; \beta)$.

Due to the condition $\beta = b/D > 0$, $b \in [0, 1]$ and $D = 1/3\,\mathrm{mm}$, we calculate $u_m^n(x_d, t; \beta)$ and $u_m^a(x_d, t; \beta)$ for

$$\beta \in \{0\,\mathrm{mm}^{-1},\ 0.5\,\mathrm{mm}^{-1},\ 1.0\,\mathrm{mm}^{-1},\ 1.5\,\mathrm{mm}^{-1}\},$$

where $x_c = (10, 10, 30)$, $\{x_d, x_s\} = \big\{(14, 10, 0), (6, 10, 0)\big\}$ and parameters v, μ_a set as (3.3.3). In Figure 3.3, we plot the values of u_m^n and u_m^a for different β.

From the numerical results shown in Figure 3.3, we can summarize the following observations:

(i) For $\beta = 0\,\mathrm{mm}^{-1}$, u_m and u_m^a are almost indistinguishable, which implies that our asymptotic formula is accurate as β approaches 0.

(ii) As β changes, u_m^a has the same change as u_m, which shows that u_m^a depends on Robin coefficient β.

(iii) Comparing the case $\beta = 0$ and $\beta > 0$, the order of magnitude of u_m and the time (peak time) to reach the maximum are significantly different. Physically, photons scattered by fluorophores are less easily observed by the boundary as β increases. Therefore, the measured data at the boundary is smaller and the peak time is earlier. We show the maximum of u_m and u_m^a in Table 6.2, where t_{peak} and t_{peak}^a are the times when u_m and u_m^a reach their maximum, respectively.

TABLE 3.2: Maximum of numerical solution and asymptotic solution for different Robin coefficient β

β	t_{peak}	$u_m(t_{peak})$	t_{peak}^a	$u_m^a(t_{peak}^a)$
0	723.5000	1.0400e-21	723.4726	1.0400e-21
0.5	704.5000	3.0421e-22	703.6550	2.9803e-22
1.0	697.3000	1.4492e-22	696.5935	1.3978e-22
1.5	693.6000	8.3908e-23	692.9314	8.0989e-23

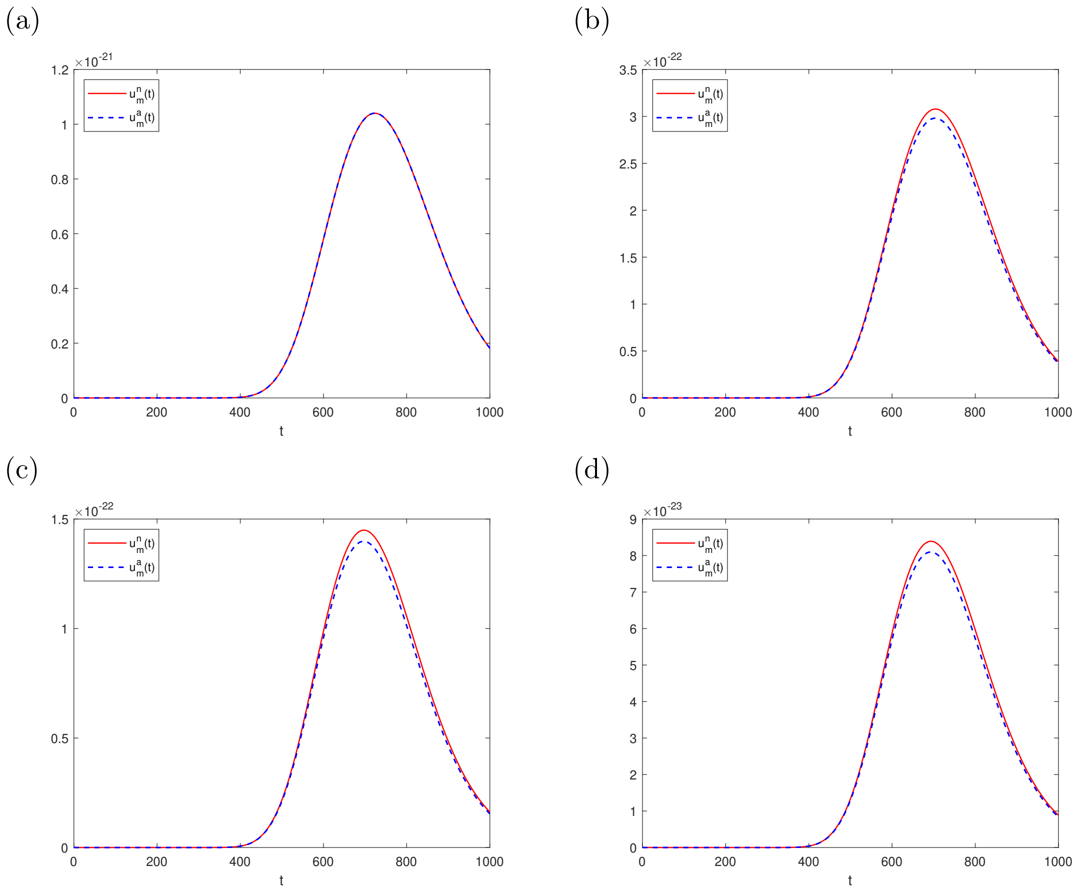

FIGURE 3.3: Numerical solution $u_m^n(x_d,\, t;\, \beta)$ and Asymptotic solution $u_m^a(x_d,\, t;\, \beta)$ for $\{x_d,\, x_s\} = \big\{(14,\, 10,\, 0),\, (6,\, 10,\, 0)\big\}$, $x_c = (10,\, 10,\, 30)$ and different β: (a) $\beta = 0\,\mathrm{mm}^{-1}$, (b) $\beta = 0.5\,\mathrm{mm}^{-1}$, (c) $\beta = 1.0\,\mathrm{mm}^{-1}$, (d) $\beta = 1.5\,\mathrm{mm}^{-1}$

.

We close this chapter by giving some discussions, which is also the motivation for the next chapter. Although we get the asymptotic solution (3.2.4) is more concise than the analytical solution (3.0.1). We already numerically verified that the asymptotic solution approximates the solution very nicely. However, it is still difficult to reconstruct the location x_c of the unknown single point target directly by using (3.2.4). Fortunately, concerning the asymptotic solution and the analytic solution, each of their peak times is unique. Also, their peak times are very close to each other, which can be seen in Table 3.2. Besides this observation, Theorem 3.4 gave the asymptotic formula to the time derivative of u_m, which is written as a polynomial equation multiplying u_m^a. In the next chapter, we are going to use these to analyze the relation between the peak time and the distance between the target and the S-D pair.

Chapter 4

Approximate Peak Time for Single Point Target

In this chapter, we discuss the properties of approximate peak time for the case of single point target. Then, we verify the consistency of the properties and the accuracy between the approximate peak time and the peak time, numerically.

By (3.2.6), which is the asymptotic formula of $\partial_t u_m$, we obtain

$$\partial_t u_m = P_3(t) u_m^a + o\left(u_m^a(t) P_3(t)\right) \quad \text{as} \quad x_{c3} \to \infty,$$

where P_3 is a cubic polynomial as in (3.2.7),

$$P_3(t) = -\mu_a v - \frac{3}{2} t^{-1} + \frac{|x_d - x_c|^2 + |x_s - x_c|^2}{2vD} t^{-2} - \frac{2\beta v D}{x_{c3} + \beta v D t}. \tag{4.0.1}$$

Here, note that $u_m^a(t)$ defined by (3.2.4) is nonnegative for $t > 0$.

Let us first give the mathematical definitions of peak time t_{peak} and approximate peak time t_{peak}^a to $u_m(t)$ and $u_m^a(t)$, respectively.

Definition 4.1. *We respectively call the times $t_{peak} > 0$ and $t_{peak}^a > 0$ the peak time and the approximate peak time if*

$$\partial_t u_m(t_{peak}) = 0 \ \text{ and } \ P_3(t_{peak}^a) = 0,$$

where approximate peak time formula P_3 is defined by (4.0.1). We will prove later that t_{peak}^a is unique in Theorem 4.1, and we can numerically verify that there is only one t_{peak} near t_{peak}^a.

The rest of this chapter is organized as follows. The unique existence and mathematical properties of t_{peak}^a will be rigorously proved in Section 4.1. Numerical verifications of both the unique existence and mathematical properties of t_{peak} are shown in Section 4.2.

4.1 Mathematical properties of approximate peak time

In this section, we show the uniqueness, order relation and symmetry of the approximate peak time, which will be used to propose a reconstruction algorithm in Chapter 5.

We first prove the unique existence of the approximate peak time as follows.

Theorem 4.1 (Uniqueness). *Fix any $x_c \in \Omega$ and x_d, $x_s \in \partial\Omega$. Then, $\partial_t u_m^a$ has a unique positive zero at $t = t_{peak}^a$, which is given as the unique positive root of the* *following cubic equation:*

$$\begin{aligned}\mathcal{T}(t) := &-2\mu_a\beta D^2v^3t^3 - (7\beta v^2D^2 + 2\mu_a Dv^2x_{c_3})t^2 + \big((|x_d - x_c|^2 + |x_s - x_c|^2)\beta vD \\ &- 3vDx_{c_3}\big)t + (|x_d - x_c|^2 + |x_s - x_c|^2)x_{c_3} = 0. \end{aligned} \tag{4.1.1}$$

Proof. Note that $\mathcal{T}(t) = 2vDt^2(x_{c_3} + \beta vDt) \times P_3(t)$. Since there is no positive root of $t^2(x_{c_3} + \beta vDt) = 0$, we show the existence of only one positive root to (4.1.1). To begin with, we examine the monotonicity of $\mathcal{T}(t)$. That is,

$$\frac{\partial\mathcal{T}}{\partial t} = -6\mu_a\beta Dv^2t^2 - (14\beta vD + 4\mu_a vx_{c_3})t + (|x_d - x_c|^2 + |x_s - x_c|^2)\beta - 3x_{c_3}. \tag{4.1.2}$$

Since the physical parameters μ_a, β, D, v and the depth x_{c_3} of the target are positive, it is obvious that the symmetry axis of the parabola associated with the quadratic, the right-hand side of (4.1.2),

$$t = -\frac{7\beta D + 2\mu_a x_{c_3}}{6\mu_a\beta Dv}$$

is negative. When the first-order coefficient of $\mathcal{T}(t)$ is less than or equal to zero, the function $\mathcal{T}(t)$ decreases monotonically over $t > 0$. Conversely, the function $\mathcal{T}(t)$ increases and then decreases. It follows from the positivity of the zero-order term of $\mathcal{T}(t)$ that there exists only a positive root to (4.1.1). □

From the proof of Theorem 4.1, the unique approximate peak time satisfies the cubic equation (4.1.1). For given $x_c \in \Omega$, the approximate peak time t^a_{peak} changes with the distance

$$\xi(x_d, x_s; x_c) := |x_d - x_c|^2 + |x_s - x_c|^2. \tag{4.1.3}$$

In the next theorem, we show that there is an order relation between the distance $\xi(x_d, x_s; x_c)$ and the approximate peak time $t^a_{peak}(x_d, x_s; x_c)$.

Theorem 4.2 (Order relation, see Figure 4.1)**.** *Let $x_c \in \Omega$ and $x_d^{(n)}$, $x_s^{(n)} \in \partial\Omega$, $n =$ 1, 2, satisfy*

$$|x_d^{(1)} - x_s^{(1)}| = |x_d^{(2)} - x_s^{(2)}|. \tag{4.1.4}$$

Then, the order of approximate peak times

$$t^a_{peak}(x_d^{(1)}, x_s^{(1)}; x_c) > t^a_{peak}(x_d^{(2)}, x_s^{(2)}; x_c) \tag{4.1.5}$$

is equivalent to the order of distances

$$\xi(x_d^{(1)}, x_s^{(1)}; x_c) > \xi(x_d^{(2)}, x_s^{(2)}; x_c). \tag{4.1.6}$$

Furthermore, $t^a_{peak}(x_d^{(2)}, x_s^{(2)}; x_c)$ attains its minimum when $x_d^{(2)}$ and $x_s^{(2)}$ satisfy

$$x_{c_1} = \frac{x_{s_1}^{(2)} + x_{d_1}^{(2)}}{2}, \quad x_{c_2} = \frac{x_{s_2}^{(2)} + x_{d_2}^{(2)}}{2}, \tag{4.1.7}$$

where $x_{d_j}^{(2)}$ and $x_{s_j}^{(2)}$, $j = 1, 2$, denote the j-th coordinate of $x_d^{(2)}$ and $x_s^{(2)}$, respectively.

Proof. For simplicity, we write

$$\xi^{(n)} := \xi(x_d^{(n)}, x_s^{(n)}; x_c), \quad t^{a,(n)}_{peak} := t^a_{peak}(x_d^{(n)}, x_s^{(n)}; x_c), \quad n = 1, 2.$$

Suppose that $t^{a,(n)}_{peak}$, $n = 1, 2$, satisfy (4.1.5). By the proof of Theorem 4.1, we have

$$t^{a,(1)}_{peak} = \overline{t^{a,(1)}_{peak}} = \underline{t^{a,(1)}_{peak}}, \tag{4.1.8}$$

where

$$\begin{aligned} \overline{t^{a,(1)}_{peak}} &:= \sup\{t > 0 : \mathcal{T}(t'; \xi^{(1)}) > 0 \ (0 < t' < t)\}, \\ \underline{t^{a,(1)}_{peak}} &:= \inf\{t > 0 : \mathcal{T}(t'; \xi^{(1)}) < 0 \ (t' > t)\}, \end{aligned} \tag{4.1.9}$$

and write $\mathcal{T}(t) = \mathcal{T}(t; \xi)$ to clarify that $\mathcal{T}(t)$ depends on $\xi = \xi(x_d, x_s; x_c)$. Then, (4.1.5) implies

$$0 = \mathcal{T}(t^{a,(1)}_{peak}; \xi^{(1)}) < \mathcal{T}(t^{a,(2)}_{peak}; \xi^{(1)}).$$

Combining this with $\mathcal{T}(t^{a,(2)}_{peak}; \xi^{(2)}) = 0$, we have

$$0 < \mathcal{T}(t^{a,(2)}_{peak}; \xi^{(1)}) - \mathcal{T}(t^{a,(2)}_{peak}; \xi^{(2)}) = (\beta v D t^{a,(2)}_{peak} + x_{c3})(\xi^{(1)} - \xi^{(2)}),$$

which immediately implies (4.1.6).

Conversely, suppose that $\xi^{(n)}$, $n = 1, 2$, satisfy (4.1.6). Then, by the definition of $\mathcal{T}(t; \xi^{(j)})$, $j = 1, 2$, we have

$$0 = \mathcal{T}(t^{a,(2)}_{peak}; \xi^{(2)}) < \mathcal{T}(t^{a,(2)}_{peak}; \xi^{(1)}),$$

which implies (4.1.5) by using (4.1.8).

The distance $\xi^{(2)}$ has a unique smallest value whenever $x^{(2)}_d$ and $x^{(2)}_s$ satisfy the condition (4.1.7). Hence, (4.1.7) gives the condition of taking the minimal approximate peak time. The uniqueness has been proved in Theorem 4.1. □

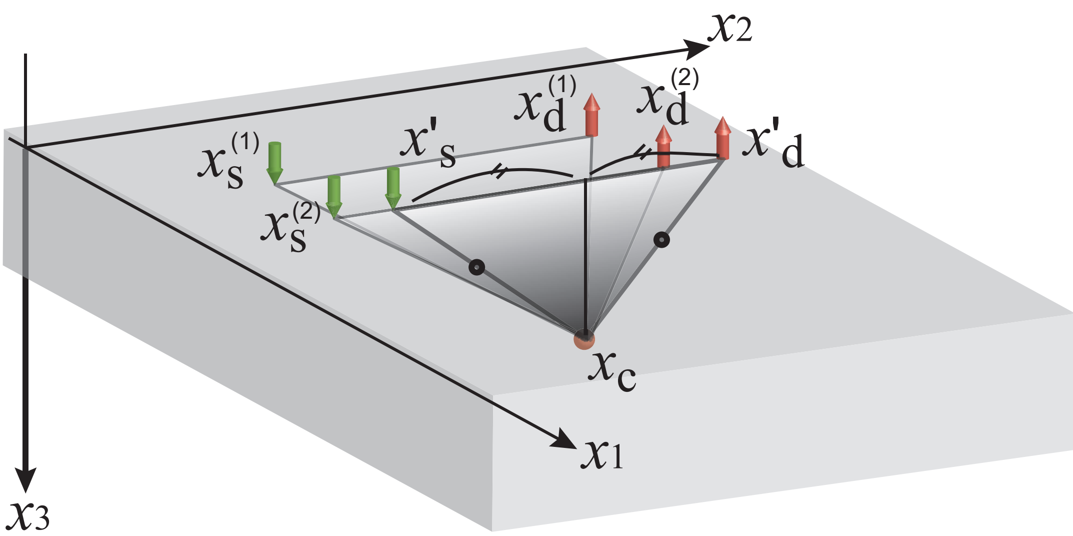

FIGURE 4.1: Mathematical property of the order relation shown in Theorem 4.2. The red symbol is the point target x_c. Two S-D pairs $\{x^{(n)}_d, x^{(n)}_s\}$, $n = 1, 2$, satisfy (4.1.4). A smaller distance between the S-D pair and the target implies a smaller approximate peak time (i.e., (4.1.6) ⇒ (4.1.5)). $\{x'_d, x'_s\}$ satisfying (4.1.7) is one of the S-D pairs with the same distance between the source $x^{(1)}_s$ and the detector $x^{(1)}_d$. It gives the smallest approximate peak time

Next, for two S-D pairs $\{x_d^{(n)}, x_s^{(n)}\}$, $n = 1, 2$, and their corresponding approximate peak times $t^a_{peak}(x_d^{(n)}, x_s^{(n)}; x_c)$, $n = 1, 2$, we define the property of symmetry for the approximation peak times as follows.

Definition 4.2. *Let $x_c \in \Omega$. We call two approximate times $t^a_{peak}(x_d^{(1)}, x_s^{(1)}; x_c)$, $t^a_{peak}(x_d^{(2)}, x_s^{(2)}; x_c)$ are symmetric if we have*

$$t^a_{peak}(x_d^{(1)}, x_s^{(1)}; x_c) = t^a_{peak}(x_d^{(2)}, x_s^{(2)}; x_c), \tag{4.1.10}$$

where $x_d^{(n)}, x_s^{(n)} \in \partial\Omega$, $n = 1, 2$, are two arbitrary S-D pairs .

The meaning of the symmetry here is coming from the following fact:

$$\begin{gathered} t^a_{peak}(x_d^{(1)}, x_s^{(1)}; x_c) = t^a_{peak}(x_d^{(2)}, x_s^{(2)}; x_c) \\ \Updownarrow \\ \xi(x_d^{(1)}, x_s^{(1)}; x_c) = \xi(x_d^{(2)}, x_s^{(2)}; x_c). \end{gathered} \tag{4.1.11}$$

This can be easily observed from (4.1.1) and the uniqueness of the approximate peak times $t^a_{peak}(x_d^{(n)}, x_s^{(n)}; x_c)$, $n = 1, 2$ for given $\{x_d^{(n)}, x_s^{(n)}\}$, $n = 1, 2$. However, there exist several S-D pairs such that their distances defined by (4.1.3) are equal. That is, these two S-D pairs satisfying (4.1.11) cannot be uniquely determined from each other.

In the next theorem, we show one special symmetry to the approximate peak time. The advantage of this kind of symmetry is that if we assume two S-D pairs satisfy the condition (4.1.12), then one of the S-D pairs can be uniquely determined by the other.

Theorem 4.3 (Symmetry, see Figure 4.2)**.** *Let $x_c \in \Omega$ and let $x_d^{(n)}, x_s^{(n)} \in \partial\Omega$, $n = 1, 2$, satisfy*

$$x_d^{(1)} - x_d^{(2)} = x_s^{(1)} - x_s^{(2)}. \tag{4.1.12}$$

Then,

$$t^a_{peak}(x_d^{(1)}, x_s^{(1)}; x_c) = t^a_{peak}(x_d^{(2)}, x_s^{(2)}; x_c)$$

implies

$$x_s^{(2)} = x_s^{(1)} + \widetilde{M}(e_1, e_2, 0), \qquad x_d^{(2)} = x_d^{(1)} + \widetilde{M}(e_1, e_2, 0), \tag{4.1.13}$$

where $\widetilde{M} := (2x_{c_1} - x_{d_1}^{(1)} - x_{s_1}^{(1)})e_1 + (2x_{c_2} - x_{d_2}^{(1)} - x_{s_2}^{(1)})e_2$ and $(e_1, e_2, 0)$ is a unit vector. Here, $\widetilde{M}$ is uniquely determined once we choose a unit vector $(e_1, e_2, 0)$.

Proof. As mentioned above, the symmetry of the approximate peak times implies the fact (4.1.11). Let us further assume that $x_d^{(1)} - x_d^{(2)} = x_s^{(1)} - x_s^{(2)}$. That is, we assume that there exist some vector $M := \widetilde{M}(e_1, e_2, 0)$ with $\widetilde{M} \in \mathbb{R}$ and a unit vector $(e_1, e_2, 0) \in \mathbb{R}^3$ satisfying

$$x_d^{(2)} = x_d^{(1)} + M, \;\; x_s^{(2)} = x_s^{(1)} + M.$$

Consequently, (4.1.11) implies

$$\widetilde{M}(x_{d_1}^{(1)} - x_{c_1})e_1 + \widetilde{M}^2 e_1^2 + \widetilde{M}(x_{d_2}^{(1)} - x_{c_2})e_2 + \widetilde{M}^2 e_2^2 + \widetilde{M}(x_{s_1}^{(1)} - x_{c_1})e_1 + \widetilde{M}(x_{s_2}^{(1)} - x_{c_2})e_2 = 0.$$

Since the vector $(e_1, e_2, 0)$ is a unit vector, we obtain

$$\widetilde{M} = (2x_{c_1} - x_{d_1}^{(1)} - x_{s_1}^{(1)})e_1 + (2x_{c_2} - x_{d_2}^{(1)} - x_{s_2}^{(1)})e_2,$$

which implies the unique existence of vector M. $\square$

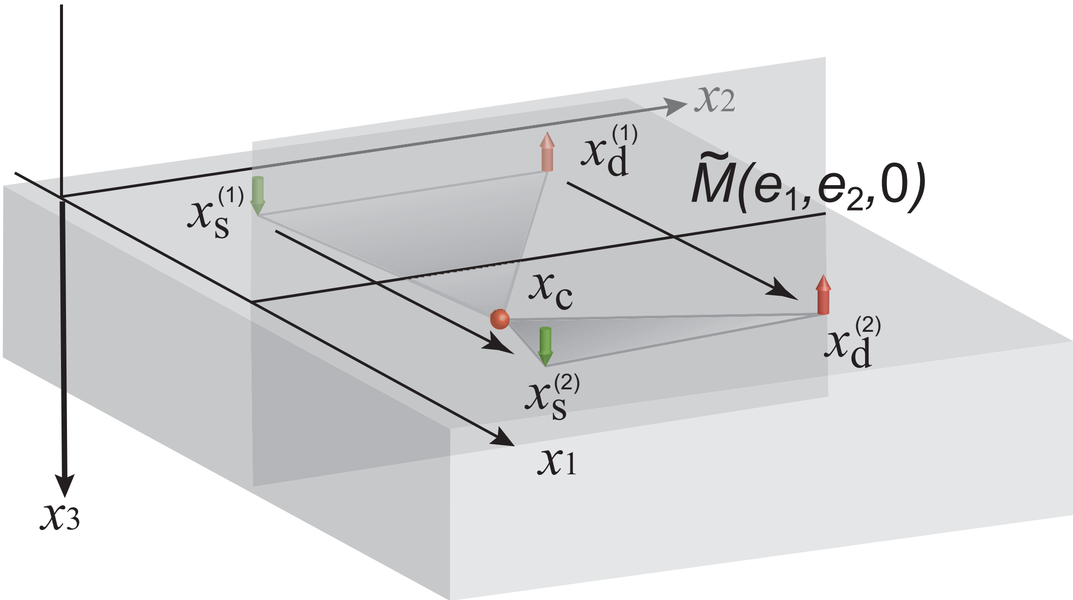

FIGURE 4.2: Mathematical property of symmetry shown in Theorem 4.3. The red symbol is the point target x_c. For two S-D pairs $\{x_d^{(n)}, x_s^{(n)}\}$, $n = 1, 2$, satisfying (4.1.12), these two S-D pairs satisfy the relation (4.1.13) if their corresponding approximate peak times are the same (i.e., (4.1.10) $\Rightarrow$ (4.1.13))

Based on Theorem 4.3, for given $x_d^{(n)}, x_s^{(n)} \in \partial\Omega$, $n = 1, 2$, satisfying (4.1.12), the same approximate peak times (4.1.10) implies that x_{c_1} and x_{c_2} are coupled in the relation as follows:

$$\begin{cases} x_{d_1}^{(2)} = x_{d_1}^{(1)} + (2x_{c_1} - x_{d_1}^{(1)} - x_{s_1}^{(1)})e_1^2 + (2x_{c_2} - x_{d_2}^{(1)} - x_{s_2}^{(1)})e_1e_2, \\ x_{d_2}^{(2)} = x_{d_2}^{(1)} + (2x_{c_1} - x_{d_1}^{(1)} - x_{s_1}^{(1)})e_1e_2 + (2x_{c_2} - x_{d_2}^{(1)} - x_{s_2}^{(1)})e_2^2, \end{cases} \tag{4.1.14}$$

where $e_1 = \frac{x_{d_1}^{(2)} - x_{d_1}^{(1)}}{\sqrt{(x_{d_1}^{(2)} - x_{d_1}^{(1)})^2 + (x_{d_2}^{(2)} - x_{d_2}^{(1)})^2}}$ and $e_2 = \frac{x_{d_2}^{(2)} - x_{d_2}^{(1)}}{\sqrt{(x_{d_1}^{(2)} - x_{d_1}^{(1)})^2 + (x_{d_2}^{(2)} - x_{d_2}^{(1)})^2}}$. However, even if we had relation (4.1.14), we might not be able to solve for x_{c_1}, x_{c_2} for given x_d, x_s.

With an additional assumptions on (4.1.12), we have the following conclusion on the solvability of x_{c_1} and x_{c_2} in (4.1.14).

Corollary 4.1. *For unknown $x_c \in \Omega$, setting $x_d^{(n)}, x_s^{(n)} \in \partial\Omega$, $n = 1, 2$, with*

$$x_{s_1}^{(1)} - x_{s_1}^{(2)} = x_{d_1}^{(1)} - x_{d_1}^{(2)}, \quad x_{s_2}^{(1)} = x_{s_2}^{(2)}, \quad x_{d_2}^{(1)} = x_{d_2}^{(2)}, \tag{4.1.15}$$

then, (4.1.10) implies

$$x_{c_1} = \frac{x_{s_1}^{(1)} + x_{d_1}^{(2)}}{2}.$$

Similarly, if we set $x_d^{(n)}, x_s^{(n)} \in \partial\Omega$, $n = 1, 2$, *with*

$$x_{s_2}^{(1)} - x_{s_2}^{(2)} = x_{d_2}^{(1)} - x_{d_2}^{(2)}, \quad x_{s_1}^{(1)} = x_{s_1}^{(2)}, \quad x_{d_1}^{(1)} = x_{d_1}^{(2)}, \tag{4.1.16}$$

then, (4.1.10) *implies*

$$x_{c_2} = \frac{x_{s_2}^{(1)} + x_{d_2}^{(2)}}{2}.$$

We give a remark about different assumptions for the S-D pairs in Theorem 4.2, Theorem 4.3 and Corollary 4.1.

Remark 4.1.

(i) *The assumption* (4.1.4) *indicates that the distance between each detector point and source point in the two S-D pairs is equal. The assumption* (4.1.12) *indicates that one of these two S-D pairs can be obtained by moving the other at the same time. The assumption* (4.1.15) *and the assumption* (4.1.16) *indicate that one of these two S-D pairs can be obtained by moving the other at the same time along* x*-axis and* y*-axis, respectively.*

(ii) *The properties of approximate peak time shown in Theorem 4.2 and Corollary 4.1 can be obtained under the same assumption* (4.1.15) *or* (4.1.16) *on* $x_d^{(n)}, x_s^{(n)} \in \partial\Omega$, $n = 1, 2$, *since the assumption* (4.1.15) *or* (4.1.16) *directly implies the assumption* (4.1.4).

4.2 Numerical verification of the properties of the peak time

In this section, we numerically verify that the peak time has the same properties, which have been rigorously proved for the approximate peak time in section 4.1. Also, the approximate peak time closes to the peak time as the depth of the single point target increases.

We still set the physical parameters as follows,

$$v = 0.219\,\text{mm/ps}, \quad D = 1/3\,\text{mm}, \quad \mu_a = 0.1\,\text{mm}^{-1}, \quad \beta = 0.5493\,\text{mm}^{-1}.$$

they are typical values in biological tissues. For given $x_c \in \Omega$ and $x_d, x_s \in \partial\Omega$, we can numerically compute the peak time $t_{peak}(x_d, x_s; x_c)$ and the approximate peak time $t_{peak}^a(x_d, x_s; x_c)$ from (3.3.1) and (4.1.1), respectively.

To show the accuracy of the approximate peak time, we calculate the relative error $RelErr_t(x_d, x_s; x_c)$ of the approximate peak time defined as

$$RelErr_t(x_d, x_s; x_c) := \frac{|t_{peak}(x_d, x_s; x_c) - t_{peak}^a(x_d, x_s; x_c)|}{t_{peak}(x_d, x_s; x_c)}, \quad x_d, x_s \in \partial\Omega. \tag{4.2.1}$$

We divide the numerical verification into two parts, i.e., **Verification I** and **Verification II**.

Verification I: the uniqueness, order relation, symmetry of t_{peak} and the accuracy of t_{peak}^a.

Let $x_c = (10,\, 10,\, 20)$, with 21×21 sets of S-D pairs defined as

$$\Big\{ \{x_d^{(n,m)},\, x_s^{(n,m)}\} \\ = \{(4+m,\, n,\, 0),\, (-4+m,\, n,\, 0)\}\,,\;\; n,\, m = 0,\, 1,\, \cdots,\, 20 \Big\}. \tag{4.2.2}$$

Figure 4.3 (a) and (b) show the peak time t_{peak} and the relative error (4.2.1) of the approximate peak time for each S-D pair given in the set (4.2.2), respectively. Here, we should mention that each grid point $(n,\, m)$ in Figure 4.3 (a) and (b) corresponds to the peak time $t_{peak}(x_d^{(n,m)},\, x_s^{(n,m)};\, x_c)$ and the relative error $RelErr_t(x_d^{(n,m)},\, x_s^{(n,m)};\, x_c)$, respectively. For simplicity, let us write

$$t_{peak}^{(n,m)} := t_{peak}(x_d^{(n,m)},\, x_s^{(n,m)};\, x_c),\quad t_{peak}^{a,(n,m)} := t_{peak}^{a}(x_d^{(n,m)},\, x_s^{(n,m)};\, x_c),$$
$$\xi^{(n,\,m)} := \xi(x_d^{(n,m)},\, x_s^{(n,m)};\, x_c),$$

where the distance $\xi^{(n,\,m)}$ is defined by (4.1.3).

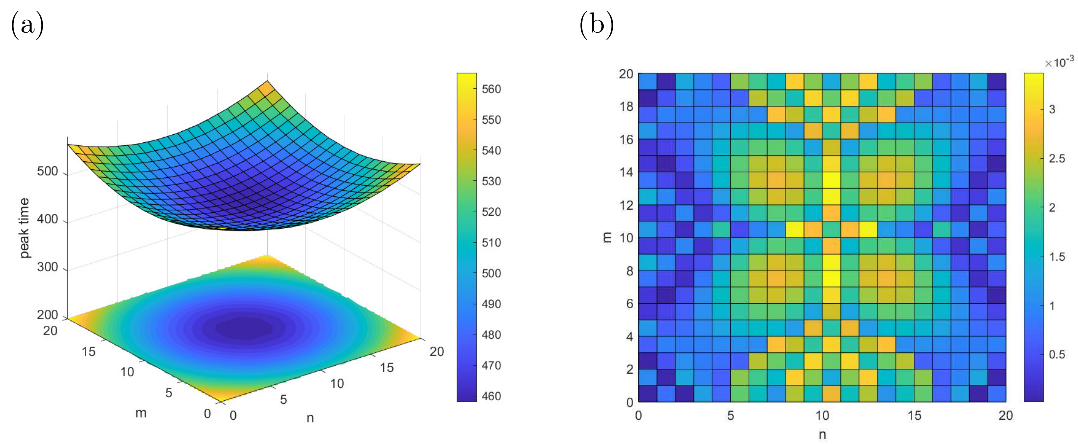

FIGURE 4.3: Peak times (a) and relative error of approximate peak time (b) for target $x_c = (10,\, 10,\, 20)$ and for all S-D pairs (4.2.2)

.

The results shown in Figure 4.3 indicate the consistency between the approximate peak time and the peak time to some extent: uniqueness, the same properties, and nice accuracy. Let us give a more precise explanation as follows.

- Uniqueness: For each S-D pair $\{x_d^{(n,m)},\, x_s^{(n,m)}\}$, $n,\, m = 0,\, 1,\, \cdots,\, 20$, there always exists only one peak time, because the grid points in Figure 4.3 (a) correspond to the peak times one by one.

- Order relation: From the settings of x_c and (4.2.2), the distance $\xi^{(n,m)}$ reaches the minimum as $(n,\, m) = (10,\, 10)$. As $(n,\, m) \to (10,\, 10)$, the distance $\xi^{(n,m)}$ becomes shorter and shorter. From Figure 4.3 (a), the peak time $t_{peak}^{(n,m)}$ becomes smaller and smaller as $(n,\, m) \to (10,\, 10)$. We obtain the smallest peak time as $(n,\, m) = (10,\, 10)$.

- Symmetry: From the contour lines of the peak times at the bottom of Figure 4.3 (a), the peak times have some symmetry with $(n,\, m) = (10,\, 10)$ as the center of symmetry. It is easy to observe that this symmetry agrees with Theorem 4.3 and Corollary 4.1. Furthermore, we already proved the symmetry of the approximate peak time in Theorem 4.3 and Corollary 4.1. The observed symmetry of the relative error in Figure 4.3 (b) implies that the peak time satisfies the same symmetry as the approximate peak time.

- Accuracy: The relative error in Figure 4.3 (b) indicates a good approximation of the approximate peak time.

TABLE 4.1: Peak times and approximate peak times for some S-D pairs in (4.2.2)

x_c	$(n,\ m)$	$x_d^{(n,m)}$	$x_s^{(n,m)}$	$t_{peak}^{(n,m)}$	$t_{peak}^{a,(n,m)}$	$RelErr_t$
	(20, 4)	$(8, 20, 0)$	$(0, 20, 0)$	341.4000	341.0046	1.1580e-03
	(0, 16)	$(20, 0, 0)$	$(12, 0, 0)$	341.4000	341.0046	1.1580e-03
$(10, 10, 10)$	(10, 9)	$(13, 10, 0)$	$(5, 10, 0)$	222.1000	220.5207	7.1109e-03
	(10, 10)	$(14, 10, 0)$	$(6, 10, 0)$	221.1000	219.4309	7.5491e-03
	(10, 11)	$(15, 10, 0)$	$(7, 10, 0)$	222.1000	220.5207	7.1109e-03
	(0, 4)	$(8, 0, 0)$	$(0, 0, 0)$	533.3000	532.6174	1.2800e-03
	(20, 16)	$(20, 20, 0)$	$(12, 20, 0)$	533.3000	532.6174	1.2800e-03
$(10, 10, 20)$	(10, 9)	$(13, 10, 0)$	$(5, 10, 0)$	458.8000	457.6963	2.4056e-03
	(10, 10)	$(14, 10, 0)$	$(6, 10, 0)$	458.2000	457.1005	2.3997e-03
	(10, 11)	$(15, 10, 0)$	$(7, 10, 0)$	458.8000	457.6963	2.4056e-03
$(10, 10, 30)$	(10, 10)	$(14, 10, 0)$	$(6, 10, 0)$	703.5000	702.6783	1.1681e-03
$(10, 10, 40)$	(10, 10)	$(14, 10, 0)$	$(6, 10, 0)$	951.1000	950.4580	6.7505e-04
$(10, 10, 50)$	(10, 10)	$(14, 10, 0)$	$(6, 10, 0)$	1199.7000	1199.1492	4.5911e-04
$(10, 10, 60)$	(10, 10)	$(14, 10, 0)$	$(6, 10, 0)$	1448.8000	1448.3039	3.4242e-04

We further quantify the mentioned consistency between the approximate peak time and the peak time by randomly selecting several sets of S-D pairs from (4.2.2) in Table 4.1. Let us take the case $x_c = (10,\ 10,\ 20)$ as an example, and the case $x_c = (10,\ 10,\ 10)$ shows a similar result. We obtain

$$t_{peak}^{a,(0,4)} = t_{peak}^{a,(20,16)},\ t_{peak}^{(0,4)} = t_{peak}^{(20,16)},\quad t_{peak}^{a,(10,9)} = t_{peak}^{a,(10,11)},\ t_{peak}^{(10,9)} = t_{peak}^{(10,11)},$$

when $\{x_d^{(0,4)},\ x_s^{(20,16)}\}$ and $\{x_d^{(10,9)},\ x_s^{(10,11)}\}$ satisfy the condition (4.1.13), respectively. Also, we observe the order relation

$$t_{peak}^{(0,4)} > t_{peak}^{(10,9)} > t_{peak}^{(10,10)}$$

for $\xi^{(0,\,4)} > \xi^{(10,\,9)} > \xi^{(10,\,10)}$. We get the smallest peak time $t_{peak}^{(10,10)}$ and the smallest approximate peak time $t_{peak}^{a,(10,10)}$, because $\{x_d^{(10,10)},\ x_s^{(10,10)}\}$ satisfies the condition (4.1.7).

Next, we verify the asymptotic formula of $\partial_t u_m$ as $x_{c_3} \to \infty$ proven in Theorem 3.4. Here, we only consider the approximation of the asymptotic formula of (3.2.6) at the peak time.

Verification II: the error between t_{peak} and t_{peak}^a as the depth of target x_c increases.

Let

$$x_c = (10,\ 10,\ 10),\ (10,\ 10,\ 20),\ \cdots,\ (10,\ 10,\ 60).$$

In Table 4.1, we show the results of $t_{peak}^{(10,10)}(x_c)$, $t_{peak}^{a,(10,10)}(x_c)$ and $RelErr_t(x_c)$ for fixed $\{x_d^{(10,10)}, x_s^{(10,10)}\}$. Comparing the relative errors, we observe that $t_{peak}^{a,(10,10)}$ gets closer and closer to $t_{peak}^{(10,10)}$ as the depth x_{c_3} of the target increases, which is consistent with asymptotic formula given in (3.1.18).

Despite the limited numerical results, the same properties can be observed regardless of the S-D pair and the target location. Therefore, it is reasonable to use the approximate peak time formula and the nice properties of the approximate peak time to formulate a scheme to reconstruct the location of the unknown point target in the next chapter.

Chapter 5

Bisection Reconstruction Algorithm and Numerical Experiments for Single Point Target

In this chapter, we present a reconstruction algorithm to reconstruct the location $x_c := (x_{c_1}, x_{c_2}, x_{c_3})$ of an unknown single point target from several measured peak times. It is a bisection-type algorithm. More precisely, by using the mentioned order relation and symmetry, we first reconstruct (x_{c_1}, x_{c_2}) by the bisection method taking the measured peak time t_{peak} as an index. Then, the depth x_{c_3} can be reconstructed by solving a cubic equation. We have assumed here that the peak time has the same properties as the approximate one, i.e., uniqueness, order relation, and symmetry. From here, unless specified, we do not distinguish the peak time and the approximate peak time.

The rest of this chapter is organized as follows. In Section 5.1, we give a framework of the proposed algorithm. A detailed explanation of reconstructing (x_{c_1}, x_{c_2}) is given in Section 5.2. Several numerical experiments are presented in Section 5.3.

5.1 Framework of algorithm

In this section, we utilize the properties of the peak time shown in Chapter 4 and the approximate peak time formula $P_3(t)$ defined by (4.1.1) to give a framework of the bisection reconstruction algorithm.

Rewrite the approximate peak time formula (4.1.1) as a cubic equation for x_{c_3} as follows:

$$\begin{aligned}&2x_{c_3}^3 + 2\beta Dvt x_{c_3}^2 + \big(-2\mu_a Dv^2t^2 - 3Dvt + (x_{d_1} - x_{c_1})^2 + (x_{d_2} - x_{c_2})^2 \\ &+ (x_{s_1} - x_{c_1})^2 + (x_{s_2} - x_{c_2})^2\big)x_{c_3} + \big(-2\mu_a\beta D^2v^3t^3 - 7\beta D^2v^2t^2 \\ &+ \beta Dvt((x_{d_1} - x_{c_1})^2 + (x_{d_2} - x_{c_2})^2 + (x_{s_1} - x_{c_1})^2 + (x_{s_2} - x_{c_2})^2)\big) = 0. \qquad (5.1.1)\end{aligned}$$

From the statements given in Theorem 4.2 and Corollary 4.1, it is obvious that the properties of the peak time only depend on (x_{c_1}, x_{c_2}). Hence, we can divide the procedure of reconstructing x_c into two stages as follows:

Stage 1: Let (x_{c_1}, x_{c_2}) be inside of a region of interest (ROI), where ROI $\subset \partial\Omega$. By using the peak time as an index, we draw lessons from the idea of the bisection method to gradually shrink ROI to get an approximation $(x_{c_1}^{inv}, x_{c_2}^{inv})$ (see Section 5.2 for details).

Stage 2: Substituting a set of parameters $x_d,\, x_s \in \partial\Omega$, $t = t_{peak} := t_{peak}(x_d,\, x_s;\, x_c)$ and $(x_{c_1},\, x_{c_2}) = (x_{c_1}^{inv},\, x_{c_2}^{inv})$ into (5.1.1), the depth x_{c_3} can be determined by solving the cubic equation (5.1.1).

Now we give the existence of a positive solution to equation (5.1.1).

Proposition 5.1. *For given a set of positive parameters β, D, v and t_{peak}, the cubic equation* (5.1.1) *has at most one positive root.*

Proof. For convenience, write (5.1.1) as $X(x_{c_3}) = 0$ and consider its monotonicity over $x_{c_3} > 0$. The x_{c_3}-derivative of X is

$$\begin{aligned}\frac{\mathrm{d}X}{\mathrm{d}x_{c_3}} =& 6x_{c_3}^2 + 4\beta D v t_{peak} x_{c_3} - 2\mu_a D v^2 t_{peak}^2 - 3Dvt_{peak} \\ &+ (x_{d_1} - x_{c_1})^2 + (x_{d_2} - x_{c_2})^2 + (x_{s_1} - x_{c_1})^2 + (x_{s_2} - x_{c_2})^2.\end{aligned} \tag{5.1.2}$$

Since both the physical parameters β, D, v and the peak time t_{peak} are positive, the symmetry axis of the parabola associated with the quadratic, the right hand side of (5.1.2),

$$x_{c_3} = -\frac{\beta D v t_{peak}}{3}$$

is negative. If the constant term of $\frac{\mathrm{d}X}{\mathrm{d}x_{c_3}}$ is less than or equal to zero, which also implies that the constant term of X is less than zero, there exists a unique positive root to (5.1.1). If the constant term of $\frac{\mathrm{d}X}{\mathrm{d}x_{c_3}}$ is larger than zero, we need to consider whether the constant term of X is larger than, equal to or less than zero. (5.1.1) has a unique positive root when the constant term of X is less than zero. Otherwise, there is no positive root. $\square$

We remark here that even though Proposition 5.1 does not state the existence of solution x_{c_3}, it does exist in terms of actual physical processes.

5.2 Alogorithm of reconstructing $(x_{c_1},\, x_{c_2})$

In this section, we use the properties of the peak time discussed in Chapter 4 to develop the reconstruction algorithm of Stage 1. The main purpose here is to show how the bisection method taking the peak time as an index can be applied to reconstruct $(x_{c_1},\, x_{c_2})$.

From Remark 4.1, for any $x_d^{(n)},\, x_s^{(n)} \in \partial\Omega$, $n = 1,\, 2$, satisfying $x_d^{(1)} - x_d^{(2)} = x_s^{(1)} - x_s^{(2)}$, the peak times

$$t_{peak}^{(n)} := t_{peak}(x_d^{(n)},\, x_s^{(n)};\, x_c), \qquad n = 1,\, 2,$$

satisfy the following three properties.

P1) The order relation $t_{peak}^{(1)} > t_{peak}^{(2)}$ implies $\xi(x_d^{(1)},\, x_s^{(1)};\, x_c) > \xi(x_d^{(2)},\, x_s^{(2)};\, x_c)$, where $\xi(x_d^{(n)},\, x_s^{(n)};\, x_c) := |x_d^{(n)} - x_c|^2 + |x_s^{(n)} - x_c|^2$, $n = 1,\, 2$.

P2) $t_{peak}^{(2)}$ attains its minimum when $x_d^{(2)},\, x_s^{(2)} \in \partial\Omega$ satisfy the condition $x_{c_1} = \frac{x_{s_1}^{(2)} + x_{d_1}^{(2)}}{2}$ and $x_{c_2} = \frac{x_{s_2}^{(2)} + x_{d_2}^{(2)}}{2}$.

P3) Equal peak times $t_{peak}^{(1)} = t_{peak}^{(2)}$ implies

$$\begin{cases} x_{d_1}^{(2)} = x_{d_1}^{(1)} + (2x_{c_1} - x_{d_1}^{(1)} - x_{s_1}^{(1)})e_1^2 + (2x_{c_2} - x_{d_2}^{(1)} - x_{s_2}^{(1)})e_1 e_2, \\ x_{d_2}^{(2)} = x_{d_2}^{(1)} + (2x_{c_1} - x_{d_1}^{(1)} - x_{s_1}^{(1)})e_1 e_2 + (2x_{c_2} - x_{d_2}^{(1)} - x_{s_2}^{(1)})e_2^2, \end{cases} \tag{5.2.1}$$

where $e_1 = \frac{x_{d_1}^{(2)} - x_{d_1}^{(1)}}{\sqrt{(x_{d_1}^{(2)} - x_{d_1}^{(1)})^2 + (x_{d_2}^{(2)} - x_{d_2}^{(1)})^2}}$ and $e_2 = \frac{x_{d_2}^{(2)} - x_{d_2}^{(1)}}{\sqrt{(x_{d_1}^{(2)} - x_{d_1}^{(1)})^2 + (x_{d_2}^{(2)} - x_{d_2}^{(1)})^2}}$.

For easy understanding, assume that we already know the second coordinate $x_{c_2} = x_{c_2}^{inv}$ of the unknown target. Let ROI $:= (x_l, x_r) \subset \partial\Omega$ be the region of interest for x_{c_1}, i.e., $x_{c_1} \in$ ROI. In light of the idea of the bisection method to determine the root of a continuous function [50], we can choose two S-D pairs $\{x_d^{(1)}, x_s^{(1)}\}$ and $\{x_d^{(2)}, x_s^{(2)}\}$ satisfying $x_d^{(1)} - x_d^{(2)} = x_s^{(1)} - x_s^{(2)}$ defined as

$$\begin{aligned} \{x_d^{(1)}, x_s^{(1)}\} &:= \left\{(x_l + \tfrac{L}{2}, x_{c_2}^{inv}, 0), (x_l - \tfrac{L}{2}, x_{c_2}^{inv}, 0)\right\}, \\ \{x_d^{(2)}, x_s^{(2)}\} &:= \left\{(x_r + \tfrac{L}{2}, x_{c_2}^{inv}, 0), (x_r - \tfrac{L}{2}, x_{c_2}^{inv}, 0)\right\}, \end{aligned} \tag{5.2.2}$$

with $L > 0$. In this case, we have $e_1 = 1$ and $e_2 = 0$. Then, we use the peak times as the index and the properties P1)–P3) as the criteria to determine x_{c_1}.

More precisely, if $t_{peak}^{(1)} = t_{peak}^{(2)}$, we get the reconstruction $x_{c_1}^{inv} = \frac{x_{s_1}^{(1)} + x_{d_1}^{(2)}}{2} = \frac{x_l + x_r}{2}$ from the property P3). Otherwise, we need to shrink ROI step by step via the property P1) until we arrive at the property P2). That is, if $t_{peak}^{(1)} < t_{peak}^{(2)}$, we halve the current ROI, update x_r as $\frac{x_l + x_r}{2}$, denoting it by $x_r \leftarrow \frac{x_l + x_r}{2}$, and update ROI $\leftarrow (x_l, x_r)$. Conversely, if $t_{peak}^{(1)} > t_{peak}^{(2)}$, we halve the current ROI, update $x_l \leftarrow \frac{x_l + x_r}{2}$, ROI $\leftarrow (x_l, x_r)$. We can go further, setting the S-D pairs as (5.2.2) and repeating to use the order relation of the peak times to reconstruct x_{c_1}. Figure 5.1 shows the shrinking ROI of the first four times by using the peak times as the index when there are no two equal peak times. We refer to this scheme as Algorithm 1 and call it the bisection reconstruction algorithm after the dimensionality reduction.

Algorithm 1 Bisection reconstruction algorithm after the dimensionality reduction

---

Input: Reconstruction $x_{c_2}^{inv}$, ROI$=(x_l, x_r)$, tolerance ϵ_1 and distance L.

Step 1 Define two S-D pairs as (5.2.2).

Step 2 Compare $t_{peak}^{(1)}$ and $t_{peak}^{(2)}$ and update ROI.

If $t_{peak}^{(1)} = t_{peak}^{(2)}$, break the loop and output $x_{c_1}^{inv} = \frac{x_l + x_r}{2}$.

If $t_{peak}^{(1)} < t_{peak}^{(2)}$, update $x_r \leftarrow \frac{x_l + x_r}{2}$, ROI $\leftarrow (x_l, x_r)$.

If $t_{peak}^{(1)} > t_{peak}^{(2)}$, update $x_l \leftarrow \frac{x_l + x_r}{2}$, ROI $\leftarrow (x_l, x_r)$.

Step 3 Compute $Err_1 = x_r - x_l$ and check stop criterion.

If $Err_1 \leq \epsilon_1$, break the loop and output $x_{c_1}^{inv} = \frac{x_l + x_r}{2}$. Otherwise, go to **Step 1**.

(Note: The case of inputting $x_{c_1}^{inv}$, ROI $= (x_b, x_t)$, ϵ_2 and L can be done in the same way.)

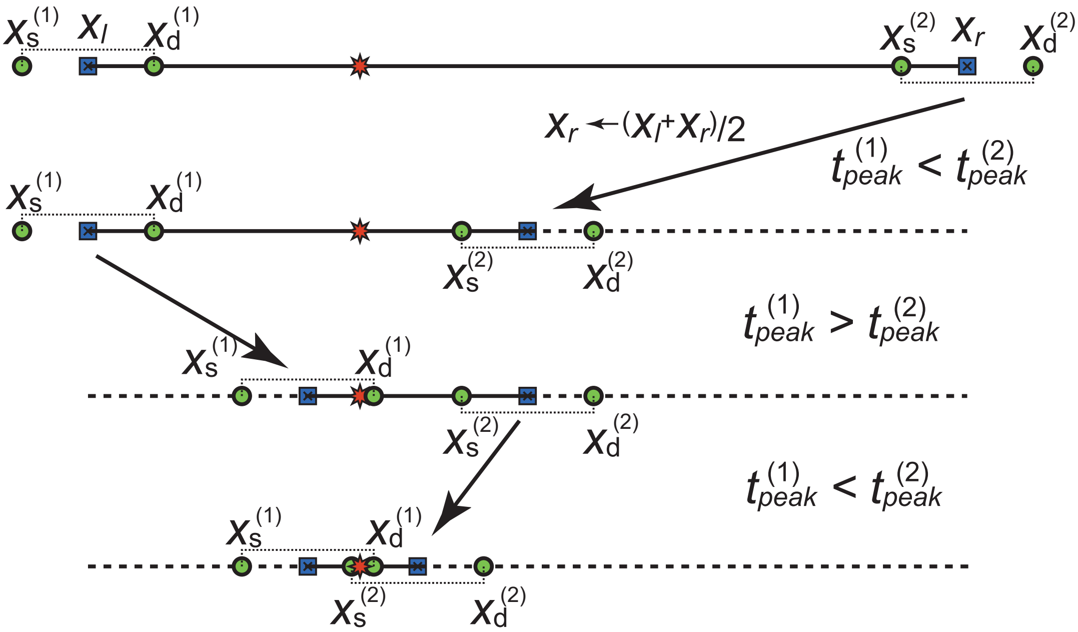

FIGURE 5.1: Bisection reconstruction algorithm to shrink ROI = (x_l, x_r) at the first four times. (Red symbol: projection of point target to ROI. Green circles connected dotted lines: S-D pairs. Solid lines: ROI. Blue boxes: endpoints x_l, x_r of ROI. Black arrows: shrink ROI once via property P1). Dash lines: abandoned ROI)

We are currently at the point of extending Algorithm 1 to reconstruct x_{c_1} and x_{c_2} simultaneously. Without loss of generality, we consider the region of interest as a rectangle, i.e., $x_c = (x_{c_1}, x_{c_2}, x_{c_3})$, $(x_{c_1}, x_{c_2}) \in (x_l, x_r) \times (x_b, x_t) =:$ ROI, which is enclosed by the solid lines in the upper left sub-graph of Figure 5.2. In light of Corollary 4.1, we define four S-D pairs as

$$\begin{aligned} \{x_d^{(1)}, x_s^{(1)}\} &:= \left\{(x_l + \tfrac{L}{2}, x_b, 0), (x_l - \tfrac{L}{2}, x_b, 0)\right\}, \\ \{x_d^{(2)}, x_s^{(2)}\} &:= \left\{(x_r + \tfrac{L}{2}, x_b, 0), (x_r - \tfrac{L}{2}, x_b, 0)\right\}, \\ \{x_d^{(3)}, x_s^{(3)}\} &:= \left\{(x_r + \tfrac{L}{2}, x_t, 0), (x_r - \tfrac{L}{2}, x_t, 0)\right\}, \\ \{x_d^{(4)}, x_s^{(4)}\} &:= \left\{(x_l + \tfrac{L}{2}, x_t, 0), (x_l - \tfrac{L}{2}, x_t, 0)\right\}, \end{aligned} \tag{5.2.3}$$

with $L > 0$. For (5.2.3), we will have four peak times

$$t_{peak}^{(n)} := t_{peak}(x_d^{(n)}, x_s^{(n)}; x_c), \qquad n = 1, 2, 3, 4.$$

We continue to use the peak times as the index and the properties P1)–P3) as the criterion to simultaneously determine (x_{c_1}, x_{c_2}). For instance, if we have

$$t_{peak}^{(1)} = t_{peak}^{(2)} < t_{peak}^{(3)} = t_{peak}^{(4)}, \tag{5.2.4}$$

that implies that

$$\xi(x_d^{(1)}, x_s^{(1)}; x_c) = \xi(x_d^{(2)}, x_s^{(2)}; x_c) < \xi(x_d^{(3)}, x_s^{(3)}; x_c) = \xi(x_d^{(4)}, x_s^{(4)}; x_c).$$

Hence, the equalities in (5.2.4) give $x_{c_1}^{inv} = \frac{x_l + x_r}{2}$ using the property P3). The inequality in (5.2.4) leads to update $x_t \leftarrow \frac{x_b + x_t}{2}$ by the property P1), update ROI $\leftarrow (x_b, x_t)$, and go to Algorithm 1. If there are no equal peak times, we can apply the property

P1) to shrink ROI according to the order relation of the peak times. As shown in the upper left sub-graph to the upper right sub-graph of Figure 5.2, the order relation

$$t_{peak}^{(4)} < \{t_{peak}^{(1)}, t_{peak}^{(2)}, t_{peak}^{(3)}\}$$

gives the information that the S-D pair $\{x_d^{(4)}, x_s^{(4)}\}$ is closer to the unknown target than the other S-D pairs. From the property P1), we halve the sides of the current ROI, update $x_r \leftarrow \frac{x_l+x_r}{2}$, $x_b \leftarrow \frac{x_b+x_t}{2}$ and ROI $\leftarrow (x_l, x_r) \times (x_b, x_t)$. Figure 5.2 shows shrinking ROI of the first four times in the bisection reconstruction algorithm. The detailed explanation of the reconstruction scheme is given as Algorithm 2.

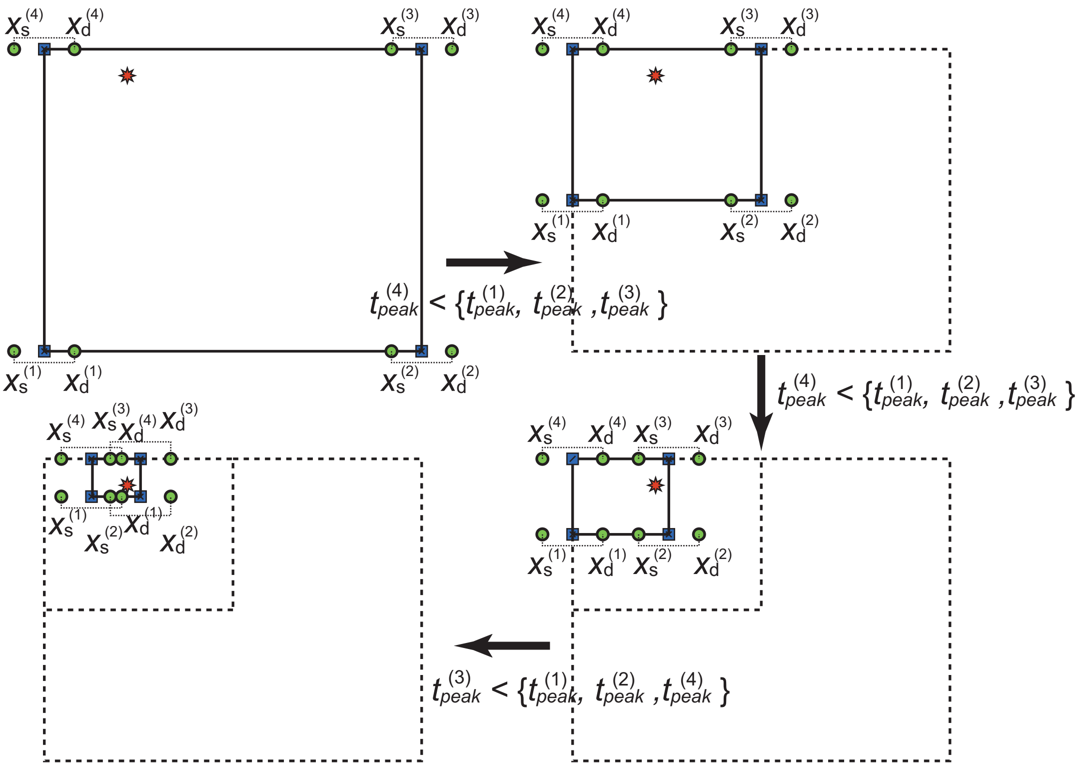

FIGURE 5.2: Bisection reconstruction algorithm to shrink ROI $= (x_l, x_r) \times (x_b, x_t)$ at the first four times. (Red symbol: projection of the point target to ROI. Green circles connected dotted lines: S-D pairs. Region enclosed by solid lines: ROI. Blue boxes: endpoints x_l, x_r, x_b, x_t of ROI. Black arrows: shrink ROI once via property P1). Dash lines: abandoned ROI)

Remark 5.1.

(i) *There is another type of situation in Step 2 of Algorithm 2. For instance, we may arrive at* $t_{peak}^{(4)} < t_{peak}^{(1)} = t_{peak}^{(3)} < t_{peak}^{(2)}$. *From (5.2.1), we can only know that the true location* (x_{c_1}, x_{c_2}) *satisfies the linear equation*

$$x_{c_2} = -\frac{x_r - x_l}{x_t - x_b} x_{c_1} + \frac{x_r^2 - x_l^2}{2(x_t - x_b)} + \frac{x_t + x_b}{2}, \; x_{c_1} < \frac{x_l + x_r}{2}. \tag{5.2.5}$$

Hence, we classify this situation as situation 3d).

(ii) *If the peak time has the same properties as the approximate one, Algorithm 2 is convergent, and its proof is similar to the bisection method for finding the*

Algorithm 2 Reconstructing (x_{c_1}, x_{c_2}) by bisection reconstruction algorithm

---

Input: ROI $= (x_l, x_r) \times (x_b, x_t)$, tolerances $\epsilon_1, \epsilon_2 > 0$ and distance L.

Step 1 Define four S-D pairs as (5.2.3).

Step 2 Compute $t_{peak}^{(n)}$, $n = 1, 2, 3, 4$, and update ROI.

- **1a)** If $t_{peak}^{(1)} = t_{peak}^{(2)} = t_{peak}^{(3)} = t_{peak}^{(4)}$, break the loop and output $x_{c_1}^{inv} = \frac{x_l+x_r}{2}$, $x_{c_2}^{inv} = \frac{x_b+x_t}{2}$.
- **2a)** If $t_{peak}^{(1)} = t_{peak}^{(2)} < t_{peak}^{(3)} = t_{peak}^{(4)}$, output $x_{c_1}^{inv} = \frac{x_l+x_r}{2}$, update $x_t \leftarrow \frac{x_b+x_t}{2}$, ROI $\leftarrow (x_b, x_t)$, break the loop and go to Algorithm 1.
- **2b)** If $t_{peak}^{(1)} = t_{peak}^{(2)} > t_{peak}^{(3)} = t_{peak}^{(4)}$, output $x_{c_1}^{inv} = \frac{x_l+x_r}{2}$, update $x_b \leftarrow \frac{x_b+x_t}{2}$, ROI $\leftarrow (x_b, x_t)$, break the loop and go to Algorithm 1.
- **2c)** If $t_{peak}^{(1)} = t_{peak}^{(4)} < t_{peak}^{(2)} = t_{peak}^{(3)}$, output $x_{c_2}^{inv} = \frac{x_b+x_t}{2}$, update $x_r \leftarrow \frac{x_l+x_r}{2}$, ROI $\leftarrow (x_l, x_r)$, break the loop and go to Algorithm 1.
- **2d)** If $t_{peak}^{(1)} = t_{peak}^{(4)} > t_{peak}^{(2)} = t_{peak}^{(3)}$, output $x_{c_2}^{inv} = \frac{x_b+x_t}{2}$, update $x_l \leftarrow \frac{x_l+x_r}{2}$, ROI $\leftarrow (x_l, x_r)$, break the loop and go to Algorithm 1.
- **3a)** If $t_{peak}^{(1)} < \{t_{peak}^{(2)}, t_{peak}^{(3)}, t_{peak}^{(4)}\}$, update $x_r \leftarrow \frac{x_l+x_r}{2}$, $x_t \leftarrow \frac{x_b+x_t}{2}$, ROI $\leftarrow (x_l, x_r) \times (x_b, x_t)$.
- **3b)** If $t_{peak}^{(2)} < \{t_{peak}^{(1)}, t_{peak}^{(2)}, t_{peak}^{(4)}\}$, update $x_l \leftarrow \frac{x_l+x_r}{2}$, $x_t \leftarrow \frac{x_b+x_t}{2}$, ROI $\leftarrow (x_l, x_r) \times (x_b, x_t)$.
- **3c)** If $t_{peak}^{(3)} < \{t_{peak}^{(1)}, t_{peak}^{(2)}, t_{peak}^{(4)}\}$, update $x_l \leftarrow \frac{x_l+x_r}{2}$, $x_b \leftarrow \frac{x_b+x_t}{2}$, ROI $\leftarrow (x_l, x_r) \times (x_b, x_t)$.
- **3d)** If $t_{peak}^{(4)} < \{t_{peak}^{(1)}, t_{peak}^{(2)}, t_{peak}^{(3)}\}$, update $x_r \leftarrow \frac{x_l+x_r}{2}$, $x_b \leftarrow \frac{x_b+x_t}{2}$, ROI $\leftarrow (x_l, x_r) \times (x_b, x_t)$.

Step 3 Compute $Err_1 := x_r - x_l$, $Err_2 := x_t - x_b$ and check stop criterion.

If $Err_1 \le \epsilon_1$, $Err_2 \le \epsilon_2$, stop and output $x_{c_1}^{inv} = \frac{x_l+x_r}{2}$, $x_{c_2}^{inv} = \frac{x_b+x_t}{2}$.

If $Err_1 > \epsilon_1$, $Err_2 \le \epsilon_2$, output $x_{c_2}^{inv} = \frac{x_b+x_t}{2}$, go to Algorithm 1 with ROI $:= (x_l, x_r)$.

If $Err_1 \le \epsilon_1$, $Err_2 > \epsilon_2$, output $x_{c_1}^{inv} = \frac{x_l+x_r}{2}$, go to Algorithm 1 with ROI $:= (x_b, x_t)$.

If $Err_1 > \epsilon_1$, $Err_2 > \epsilon_2$, go to **Step 1.**

---

root of a continuous function. Even though the speed of convergence is slow, we show that in Section 5.3, a finite number of shrinks can give a reasonable reconstruction.

5.3 Numerical experiments

In this section, we give several numerical experiments to examine the efficiency of the proposed bisection reconstruction algorithm.

Assume that the peak time $t_{peak} := t_{peak}(x_d,\, x_s;\, x_c)$ is measured from the emission light $u_m(x_d,\, t;\, x_s)$, where $\{x_d,\, x_s\}$ is the location of the selected S-D pair. To simulate the emission light for a given S-D pair, we employ the analytical solution (3.0.1) to generate it. However, noise is always unavoidable in the measurements, causing jitters and drifts of the peak time. We assume the noise level of the peak time is of order δ, namely

$$|t^{\delta}_{peak} - t_{peak}| \leq \delta, \tag{5.3.1}$$

where t^{δ}_{peak} and t_{peak} are the peak time having the noise and the peak time, respectively. We perturb t_{peak} by

$$t^{\delta}_{peak} := \Big(1 + \hat{\delta} \times (2 \times \mathrm{rand}(1) - 1)\Big) \times t_{peak}, \tag{5.3.2}$$

where $\hat{\delta}$ is the relative noise level, and rand(1) generates a uniformly distributed random number on the interval $(0,\, 1)$.

In the following numerical experiments, we still set the typical values (3.3.3) of biological tissues as the physical parameters. We define the time step size as 0.1 ps. We compute the relative error of the reconstruction by the following formula:

$$RelErr = \frac{|x_c - x^{inv}_c|}{|x_c|}, \tag{5.3.3}$$

where x_c and x^{inv}_c are the actual and the reconstructed locations of the target, respectively.

In this subsection, let us see the numerical performances of reconstructing a single point target for different noise levels $\hat{\delta}$, tolerances ϵ_1, ϵ_2, and depths of targets x_c. As the tolerances increase, we can decrease the number of shrinking ROI and then avoid an infinite set of data. We denote by ROI^{inv} the final region of interest when we stop shrinking. Since this ROI^{inv} does not always include $(x_{c_1},\, x_{c_2})$, we want to determine what tolerances can be used to get an optimal ROI^{inv}, which is ROI^{inv} including $(x_{c_1},\, x_{c_2})$ for different noise levels.

Theorem 4.2 shows that the value of peak time depends on the distance between the S-D pair and the target. For $x_d,\, x_s \in \partial\Omega$ with $|x_d - x_s| = L$, $L > 0$, (4.1.7) implies that the smallest peak time is

$$t^{min}_{peak} := t_{peak}\left((x_{c_1} + \frac{L}{2},\, x_{c_2},\, 0),\, (x_{c_1} - \frac{L}{2},\, x_{c_2},\, 0);\, x_c\right). \tag{5.3.4}$$

This value will help us visualize at least how a larger noise has been added.

Example 5.1. *Let* $x_c = (7,\, 17,\, 20)$, $\mathrm{ROI} = (0,\, 20) \times (0,\, 20)$ *and* $L = 8$. *The results of numerical inversions for different noise levels and tolerances are listed in Tables 5.1 and 5.2.*

First, let us set the relatively small tolerances $\epsilon_1 = \epsilon_2 = 0.1$, which means the initial ROI needs to be shrunk up to eight times. The numerical results are shown for different noise levels $\hat{\delta}$ in Table 5.1.

TABLE 5.1: Reconstructions for different noise levels and fixed tolerances $\epsilon_1 = \epsilon_2 = 0.1$

x_c	$\hat{\delta}$	x_c^{inv}	$RelErr$	ROI^{inv}
$(7, 17, 20)$	0	$(6.95, 16.95, 20.04)$	2.95e-03	$(6.88,\ 7.03) \times (16.88,\ 17.03)$
	0.1%	$(6.76, 17.30, 20.03)$	1.44e-02	$(6.72,\ 6.80) \times (17.27,\ 17.34)$
	1%	$(7.54, 16.99, 19.94)$	2.00e-02	$(7.50,\ 7.58) \times (16.95,\ 17.03)$
	5%	$(7.85, 17.30, 19.50)$	3.80e-02	$(7.81,\ 7.89) \times (17.27,\ 17.34)$

For the noise-free data in Table 5.1, the reconstruction $(x_{c_1}^{inv},\ x_{c_2}^{inv})$ is very close to the true location, and it is also included in ROI^{inv}. From the size of ROI^{inv}, we will find that the algorithm terminates before $Err_1,\ Err_2 \le \epsilon_1$ because the peak times corresponding to the current four S-D pairs become equal. In fact, these peak times are theoretically not equal but numerically equal due to the current precision limit of time, 0.1 ps. As this precision is improved, the reconstructed coordinate $(x_{c_1}^{inv},\ x_{c_2}^{inv})$ will converge to the true one. When we get excellent $(x_{c_1}^{inv},\ x_{c_2}^{inv})$, the error for $x_{c_3}^{inv}$ mainly comes from the approximation error of the peak time formula (4.1.1). By (5.3.4), we can compute that the smallest peak time $t_{peak}^{min} = 458.2$ ps for given $x_c = (7,\ 17,\ 20)$ and $L = 8$. For the noisy data, the orders of noise contained in the peak time (5.3.1) are at least 0.4582 ps, 4.582 ps and 22.91 ps for 0.1%, 1% and 5% relative noise levels, respectively. We find that the true location $(x_{c_1},\ x_{c_2})$ is outside of ROI^{inv}, but the reconstructions are still very close to the true ones. Even for the data at a 5% relative noise level, the absolute error for each reconstructed coordinate is less than 1 mm.

Next, we consider larger tolerances to reduce the number of shrinks and to find the optimal ROI^{inv}. We can still have reasonable numerical results, which are shown in Table 5.2.

TABLE 5.2: Reconstructions for different noise levels and different tolerances

$\hat{\delta}$	$\epsilon_1,\ \epsilon_2$	x_c^{inv}	$RelErr$	ROI^{inv}
0.1%	$1.25, 1.25$	$(6.88, 16.88, 20.06)$	6.89e-03	$(6.25,\ 7.50) \times (16.25,\ 17.50)$
1%	$1.25, 1.25$	$(8.13, 16.83, 20.27)$	4.29e-02	$(7.50,\ 8.75) \times (16.25,\ 17.50)$
5%	$1.25, 1.25$	$(8.13, 16.83, 20.64)$	4.79e-02	$(7.50,\ 8.75) \times (16.25,\ 17.50)$
1%	$5, 5$	$(7.50, 17.50, 20.06)$	2.61e-02	$(5.00,\ 10.00) \times (15.00,\ 20.00)$
5%	$5, 5$	$(7.50, 17.50, 20.50)$	3.19e-02	$(5.00,\ 10.00) \times (15.00,\ 20.00)$

The numbers of shrinks are 4 and 2 for tolerances $\epsilon_1 = \epsilon_2 = 1.25$ and $\epsilon_1 = \epsilon_2 = 5$, respectively. For the case of $\epsilon_1 = \epsilon_2 = 1.25$, we obtain a better reconstruction x_c^{inv}, and further ROI^{inv} is also much more accurate than the result of the 0.1% case in Table 5.1. The absolute errors of reconstructions $x_{c_1}^{inv}$ and $x_{c_2}^{inv}$ are less than $\frac{\epsilon_1}{2}$ and $\frac{\epsilon_2}{2}$, respectively. However, the 1% case results in a false shrink for $\epsilon_1 = \epsilon_2 = 1.25$, which occurs in the third shrink. The reason is that the true location (x_{c_1}, x_{c_2}) is approximately in the center of the current region of interest when the region of interest shrunk too small. Consequently, the peak times measured by current S-D pairs are very close to each other, making them indistinguishable. When we increase the tolerances, $\epsilon_1 = \epsilon_2 = 5$, we get a better reconstruction and the optimal ROI^{inv}

compared with the result of setting $\epsilon_1 = \epsilon_2 = 1.25$. Numerical results show that a finite number of shrinks can also give a good result and an optimal ROI for the peak time containing the noise.

From Tables 5.1 and 5.2, the depth reconstruction $x_{c_3}^{inv}$ is less affected by the noise than the reconstruction $(x_{c_1}^{inv}, x_{c_2}^{inv})$.

In the next example, we test the inversion effects on deeper targets.

Example 5.2. *We choose the same parameter settings as Example 5.1, i.e.,* ROI $= (0, 20) \times (0, 20)$, $L = 8$. *Let x_c be at* $(7, 17, 30)$ *and* $(7, 17, 40)$. *The results of numerical inversions for different noise levels are listed in Table 5.3.*

TABLE 5.3: Reconstructions for different noise levels and fixed tolerances $\epsilon_1 = \epsilon_2 = 0.1$

x_c	$\hat{\delta}$	x_c^{inv}	*RelErr*	ROI^{inv}
$(7, 17, 30)$	0	$(7.03, 17.03, 30.03)$	1.56e-03	$(6.88,\ 7.19) \times (16.88,\ 17.19)$
	0.1%	$(6.76, 17.30, 30.01)$	1.11e-02	$(6.72,\ 6.80) \times (17.27,\ 17.34)$
	1%	$(7.85, 17.30, 29.88)$	2.59e-02	$(7.81,\ 7.89) \times (17.27,\ 17.34)$
	5%	$(7.85, 17.30, 29.19)$	3.45e-02	$(7.81,\ 7.89) \times (17.27,\ 17.34)$
$(7, 17, 40)$	0	$(7.03, 17.03, 40.03)$	1.16e-03	$(6.88,\ 7.19) \times (16.88,\ 17.19)$
	0.1%	$(6.60, 17.30, 40.00)$	1.14e-02	$(6.56,\ 6.64) \times (17.27,\ 17.34)$
	1%	$(7.85, 17.30, 39.81)$	2.59e-02	$(7.81,\ 7.89) \times (17.27,\ 17.34)$
	5%	$(7.85, 17.30, 38.88)$	3.26e-02	$(7.81,\ 7.89) \times (17.27,\ 17.34)$

By (5.3.4), we can compute the smallest peak times $t_{peak}^{min} = 703.5\,\mathrm{ps}$ and $t_{peak}^{min} = 951.1\,\mathrm{ps}$ for $x_c = (7,\ 17,\ 30)$ and $x_c = (7,\ 17,\ 40)$, respectively. The peak time is more delayed as the target depth increases, causing an increase in the order of noise. Hence, the reconstruction will become worse. Compared with the results in Table 5.1, the relative error of reconstruction for different noise levels is quite similar. However, for deeper targets, the absolute error in each reconstructed coordinate of the target is increasing. Moreover, ROI^{inv} is moving further away from (x_{c_1}, x_{c_2}). In a word, the relative errors of these reconstructions are still marginal, less than a few percent.

We give the following summary of the proposed bisection reconstruction algorithm according to the numerical results:

(i) There are no complicated calculations and regularization in our proposed algorithm.

(ii) Even with a finite number of shrinks, we can still get a good reconstruction (See results in Table 5.2).

(iii) The proposed algorithm is efficient in reconstructing deeper unknown single point target (See results in Table 5.3).

Chapter 6

FDOT Problem for Multiple Point Targets

In this chapter, we consider our FDOT problem for multiple point targets. Based on the asymptotic formulae for single point target given in Theorems 3.3 and 3.4 with the principle of superposition, we first derive asymptotic formulae of the solution u_m and its time-derivative $\partial_t u_m$. Since the asymptotic formulae exponentially depend on the distance between the given S-D pair and each target, we can derive their localized asymptotic formulae. Then, an approximate peak time for each target is defined by a localized S-D pair. We numerically verify the properties and accuracy of the approximate peak time. After that, we propose a localized reconstruction algorithm to reconstruct the locations of unknown targets. We also provide the numerical performance of this algorithm by studying some numerical experiments.

Recall the multiple point targets defined in (2.2.5),

$$\mu_f(x) = \sum_{j=1}^{J} c_j \delta(x - x_c^{(j)}), \quad c_j > 0,\ j = 1,\ 2,\ \cdots,\ J,$$

where $x_c^{(1)}, x_c^{(2)}, \cdots, x_c^{(J)} \in \Omega$ are locations of multiple point targets. By the superposition and for any given $x_d, x_s \in \partial\Omega$, u_m of (2.2.3) becomes

$$u_m(x_d, t; x_s) = \sum_{j=1}^{J} \frac{c_j e^{-v\mu_a t}}{16\pi^3 D^2 v} \int_0^t \big((t-s)s\big)^{-\frac{3}{2}} e^{-\frac{|x_d - x_c^{(j)}|^2}{4vD(t-s)}} e^{-\frac{|x_s - x_c^{(j)}|^2}{4vDs}} \times \hat{\mathcal{K}}_3(x_{c_3}^{(j)};\, t-s)\hat{\mathcal{K}}_3(x_{c_3}^{(j)};\, s)\,\mathrm{d}s, \quad (6.0.1)$$

where

$$\hat{\mathcal{K}}_3(x_{c_3}; t) := 1 - \beta\sqrt{\pi v D t}\, \exp\left(\left(\frac{x_{c_3} + 2\beta v D t}{\sqrt{4vDt}}\right)^2\right) \operatorname{erfc}\left(\frac{x_{c_3} + 2\beta v D t}{\sqrt{4vDt}}\right). \quad (6.0.2)$$

Here, $|x|^2 = x_1^2 + x_2^2 + x_3^2$ for $x = (x_1, x_2, x_3) \in \mathbb{R}^3$.

The rest of this chapter is organized as follows. In Section 6.1, we derive asymptotic analyses on u_m and $\partial_t u_m$. We will obtain localized asymptotic formulae of u_m and $\partial_t u_m$ by choosing a localized S-D pair. In Section 6.2, we define an approximate peak time for each $x_c^{(j)}$, $j = 1,\ 2,\ \cdots,\ J$, by choosing a localized S-D pair. The properties and the accuracy of the approximate peak time have been numerically demonstrated. In Section 6.3, we propose a localized reconstruction algorithm. In Section 6.4, we apply this algorithm in some numerical experiments.

6.1 Asymptotic formulae of solution and its numerical verification

In this section, we give the asymptotic formulae of the solution u_m defined by (6.0.1) and its time-derivative $\partial_t u_m$ for multiple point targets. By localized S-D pair $\{x_d,\, x_s\}$, we derive their localized asymptotic formulae. Some numerical experiments are presented to verify the asymptotic formulae.

6.1.1 Asymptotic formulae of solution

In this subsection, we extend the asymptotic formulae given in Theorem 3.3 and Theorem 3.4 to the case of multiple point targets.

Theorem 6.1. *Let $x_d,\, x_s \in \partial\Omega$ and $x_c^{(1)},\, x_c^{(2)},\, \cdots,\, x_c^{(J)} \in \Omega$. For $1 \le j \le J$, assume that*

$$\Big||x_d - x_c^{(j)}|^2 - |x_s - x_c^{(j)}|^2\Big| \le C^{(j)} t \quad \text{for some} \quad C^{(j)} > 0.$$

Then, we have the asymptotic formula of u_m

$$u_m(t;\, x_c^{(1)},\, x_c^{(2)},\, \cdots,\, x_c^{(J)}) = \sum_{j=1}^{J} u_m^{a,(j)}(t)\big[1 + o(1)\big] \tag{6.1.1}$$

as $x_{c3}^{(j)} \to \infty$, $1 \le j \le J$, where

$$\begin{aligned} u_m^{a,(j)}(t) =& \frac{c_j \exp\left(-\mu_a v t\right)}{8\pi^{\frac{5}{2}} v^{\frac{1}{2}} D^{\frac{3}{2}}} \left(\frac{1}{|x_d - x_c^{(j)}|} + \frac{1}{|x_s - x_c^{(j)}|} \right) t^{-\frac{3}{2}} \\ & \times \exp\left(-\frac{|x_d - x_c^{(j)}|^2 + |x_s - x_c^{(j)}|^2}{2vDt} \right) \left(\frac{x_{c3}^{(j)}}{x_{c3}^{(j)} + \beta v D t} \right)^2 . \end{aligned} \tag{6.1.2}$$

Proof. We denote by for $1 \le j \le J$,

$$\begin{aligned} u_m^{(j)}(x_d, t; x_s) := \frac{c_j e^{-v\mu_a t}}{16\pi^3 D^2 v} \int_0^t \big((t-s)s\big)^{-\frac{3}{2}} e^{-\frac{|x_d - x_c^{(j)}|^2}{4vD(t-s)}} e^{-\frac{|x_s - x_c^{(j)}|^2}{4vDs}} \\ \times \hat{\mathcal{K}}_3(x_{c3}^{(j)};\, t-s)\hat{\mathcal{K}}_3(x_{c3}^{(j)};\, s)\,\mathrm{d}s, \end{aligned} \tag{6.1.3}$$

where function $\hat{\mathcal{K}}_3$ is defined by (6.0.2). By Theorem 3.3, we have asymptotic formula

$$u_m^{(j)}(t) = u_m^{a,(j)}(t) + O(u_m^{a,(j)}(t)(x_{c3}^{(j)})^{-1}) \;\; \text{as} \;\; x_{c3}^{(j)} \to \infty.$$

Then, as $x_{c3}^{(j)} \to \infty$, $1 \le j \le J$, we have

$$\begin{aligned} u_m(t) &= \sum_{j=1}^{J} u_m^{(j)}(t) = \sum_{j=1}^{J} \left(u_m^{a,(j)}(t) + O(u_m^{a,(j)}(t)(x_{c3}^{(j)})^{-1}) \right) \\ &= \sum_{j=1}^{J} u_m^{a,(j)}(t) + O\left(\sum_{j=1}^{J} \left(u_m^{a,(j)}(t)(x_{c3}^{(j)})^{-1} \right) \right), \end{aligned} \tag{6.1.4}$$

which implies (6.1.1). □

Theorem 6.2. *Let x_d, $x_s \in \partial\Omega$ and $x_c^{(1)}, x_c^{(2)}, \cdots, x_c^{(J)} \in \Omega$. For $1 \le j \le J$, assume that*

$$\left| |x_d - x_c^{(j)}|^2 - |x_s - x_c^{(j)}|^2 \right| \le C_1^{(j)} \frac{t}{x_{c3}^{(j)}} \quad \text{for some } C_1^{(j)} > 0,$$
$$C_2^{(j)} x_{c3}^{(j)} \le t \le C_3^{(j)} x_{c3}^{(j)} \quad \text{for some } C_2^{(j)},\ C_3^{(j)} > 0.$$

Furthermore, t-derivative of u_m is given as

$$\partial_t u_m(t) = \partial_t u_m^a(t)[1 + o(1)] = \sum_{j=1}^{J} P_3^{(j)}(t) u_m^{a,(j)}(t)[1 + o(1)] \tag{6.1.5}$$

as $x_{c3}^{(j)} \to \infty$, $1 \le j \le J$, where $u_m^{a,(j)}$ is defined by (6.1.2) and

$$P_3^{(j)}(t) := -\mu_a v - \frac{3}{2} t^{-1} + \frac{|x_d - x_c^{(j)}|^2 + |x_s - x_c^{(j)}|^2}{2vD} t^{-2} - \frac{2\beta v D}{x_{c3}^{(j)} + \beta v D t}. \tag{6.1.6}$$

Proof. By Theorem 3.4, we obtain

$$\partial_t u_m(t) = \sum_{j=1}^{J} \partial_t u_m^{a,(j)}(t) + O\left(\sum_{j=1}^{J} \left(u_m^{a,(j)}(t) (x_{c3}^{(j)})^{-3/2} \right) \right) \tag{6.1.7}$$

as $x_{c3}^{(j)} \to \infty$, $1 \le j \le J$. Then, we can get (6.1.5) with direct computation. □

Since each term, $\exp\left(-\frac{|x_d - x_c^{(j)}|^2 + |x_s - x_c^{(j)}|^2}{2vDt} \right)$, in $u_m^{a,(j)}$ is exponentially small, the dominant parts of the summations in (6.1.1) and (6.1.5) are determined by the smallest value of $|x_d - x_c^{(j)}|^2 + |x_s - x_c^{(j)}|^2$, $1 \le j \le J$.

Then, we have the following localized asymptotic formulae of solution u_m and its time-derivative $\partial_t u_m$.

Corollary 6.1. *Let x_d, $x_s \in \partial\Omega$ and $x_c^{(1)}, x_c^{(2)}, \cdots, x_c^{(J)} \in \Omega$. Assume that some $x_c^{(k)}$, $1 \le k \le J$, satisfies*

$$|x_d - x_c^{(k)}|^2 + |x_s - x_c^{(k)}|^2 < |x_d - x_c^{(j)}|^2 + |x_s - x_c^{(j)}|^2, \quad 1 \le j \ne k \le J, \tag{6.1.8}$$

and

$$\left| |x_d - x_c^{(k)}|^2 - |x_s - x_c^{(k)}|^2 \right| \le Ct \quad \text{for some} \quad C > 0.$$

Then, u_m satisfies

$$u_m(t; x_c^{(1)}, x_c^{(2)}, \cdots, x_c^{(J)}) = u_m^{a,(k)}(t) \big[1 + o(1)\big] \tag{6.1.9}$$

as $x_{c3}^{(j)} \to \infty$, $1 \le j \le J$. Furthermore, assume that

$$\left| |x_d - x_c^{(k)}|^2 - |x_s - x_c^{(k)}|^2 \right| \le C_1 \frac{t}{x_{c3}^{(k)}} \quad \text{for some } C_1 > 0,$$
$$C_2 x_{c3}^{(k)} \le t \le C_3 x_{c3}^{(k)} \quad \text{for some } C_2,\ C_3 > 0.$$

The asymptotic formula of t-derivative of u_m is

$$\partial_t u_m(t) = P_3^{(k)}(t) u_m^{a,(k)}(t)[1 + o(1)] \tag{6.1.10}$$

as $x_{c_3}^{(j)} \to \infty$, $1 \le j \le J$, *where* $u_m^{a,(k)}$ *and* $P_3^{(k)}$ *are defined by* (6.1.2) *and* (6.1.6), *respectively.*

Remark 6.1.

(i) *From Corollary 6.1, we can approximate* (6.0.1) *as there is only a single point target by using some localized S-D pair* $\{x_d, x_s\}$. *The localized S-D pair* $\{x_d, x_s\}$ *means that the condition* (6.1.8) *holds.*

(ii) *In fact, the accuracy of the localized asymptotic formulae given in Corollary 6.1 depends on the condition* (6.1.8). *That is, in the case of* $\{x_d, x_s\}$ *satisfying*

$$|x_d - x_c^{(k)}|^2 + |x_s - x_c^{(k)}|^2 \ll |x_d - x_c^{(j)}|^2 + |x_s - x_c^{(j)}|^2, \quad 1 \le j \ne k \le J, \tag{6.1.11}$$

the asymptotic formulae (6.1.9) *and* (6.1.10) *should be more accurate.*

6.1.2 Numerical verification

In this subsection, we verify the asymptotic formulae given in Corollary 6.1 through numerical experiments. Without loss of generality, we assume that there are two point targets, i.e., $J = 2$ in (2.2.5), with locations $x_c^{(1)}$ and $x_c^{(2)}$.

The following numerical verifications mainly examine the influence of condition (6.1.8) on the asymptotic analysis. The accuracy of the asymptotic formulae is determined by the distance between $x_c^{(1)}$ and $x_c^{(2)}$ for arbitrarily chosen S-D pairs by Remark 6.1 (ii). Therefore, we consider the two extreme cases where two point targets are very far apart and very close in **Verification I** and **Verification II**, respectively. That is, there exists some S-D pair satisfying condition (6.1.11) in **Verification I**. However, there is no such S-D pair in **Verification II**.

For $J = 2$, the analytical solution $u_m = \sum_{j=1}^{2} u_m^{(j)}$, where $u_m^{(j)}$ is defined by (6.1.3). Given $x_c^{(1)}$, $x_c^{(2)} \in \Omega$ and x_d, $x_s \in \partial\Omega$, we numerically calculate each $u_m^{(j)}$ by the numerical integration (3.3.1) and then obtain numerical solution u_m^n of u_m. The asymptotic solution $u_m^{a,(j)}$, $j = 1, 2$, defined by (6.1.2) can be directly calculated at grid points.

Verification I: Let $x_c^{(1)} = (2, 10, 20)$, $x_c^{(2)} = (18, 10, 20)$. These two point targets are far apart.

We choose the following three S-D pairs to calculate u_m^n, $u_m^{a,(1)}$ and $u_m^{a,(2)}$:

$$\{x_d, x_s\} \in \big\{\{(4, 10, 0), (0, 10, 0)\}, \{(12, 10, 0), (8, 10, 0)\}, \{(20, 10, 0), (16, 10, 0)\}\big\}.$$

The numerical results are shown in Figure 6.1, Figure 6.2 and Figure 6.3 for each S-D pair.

Discussion I: For the result of S-D pair $\{x_d, x_s\} = \big\{(4, 10, 0), (0, 10, 0)\big\}$, we have the condition

$$|x_d - x_c^{(1)}|^2 + |x_s - x_c^{(1)}|^2 \ll |x_d - x_c^{(2)}|^2 + |x_s - x_c^{(2)}|^2. \tag{6.1.12}$$

Hence, it is obvious that the asymptotic solutions $u_m^{a,(1)}$ and $u_m^{a,(1)} + u_m^{a,(2)}$ are indistinguishable in Figure 6.1. Also, both of them have a good approximation to u_m^n. Due to (6.1.12), the value of $u_m^{a,(2)}$ is much smaller than $u_m^{a,(1)}$ and u_m^n.

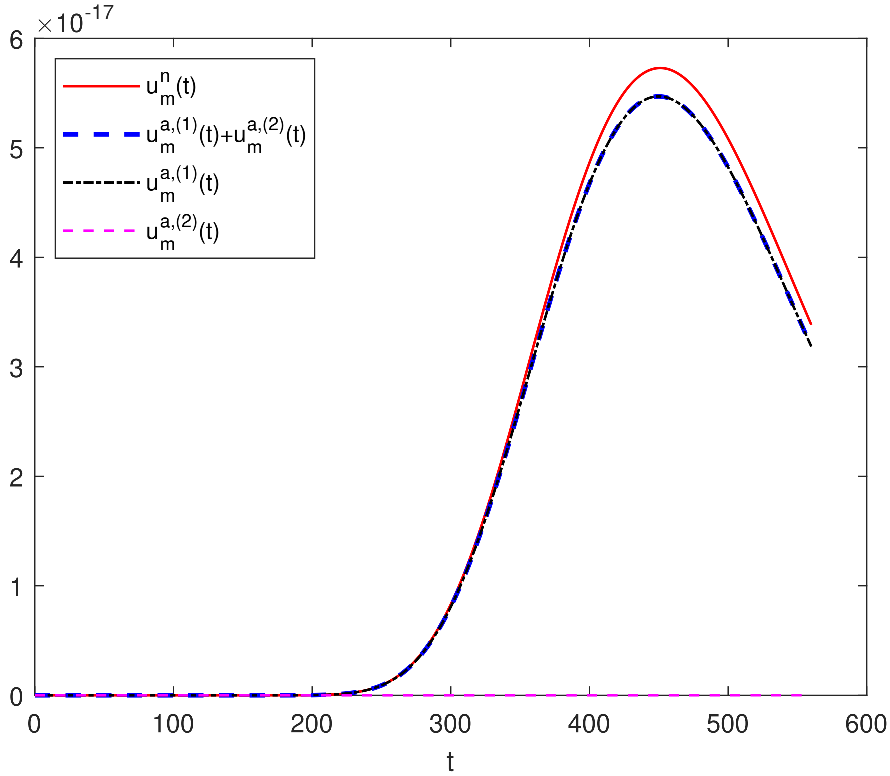

FIGURE 6.1: Numerical solution $u_m^n(x_d, t; x_s)$ and asymptotic solution $u_m^a(x_d, t; x_s)$ of **Verification I** for $\{x_d, x_s\} = \{(4, 10, 0), (0, 10, 0)\}$

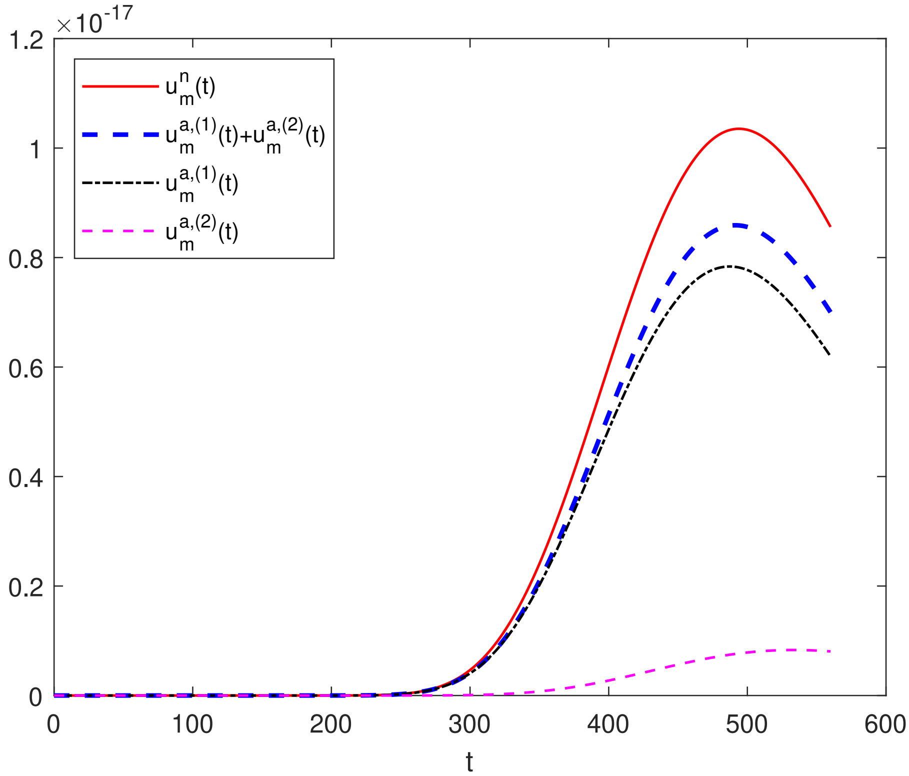

FIGURE 6.2: Numerical solution $u_m^n(x_d,\, t;\, x_s)$ and asymptotic solution $u_m^a(x_d,\, t;\, x_s)$ of **Verification I** for $\{x_d,\, x_s\} = \big\{(12,\, 10,\, 0),\, (8,\, 10,\, 0)\big\}$

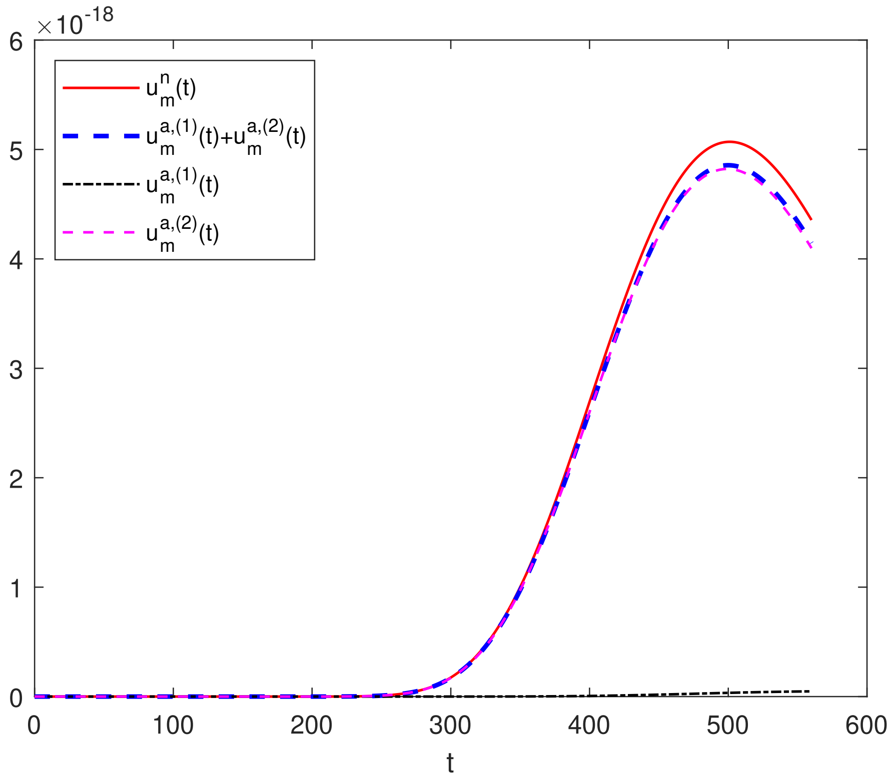

FIGURE 6.3: Numerical solution $u_m^n(x_d,\, t;\, x_s)$ and asymptotic solution $u_m^a(x_d,\, t;\, x_s)$ of **Verification I** for $\{x_d,\, x_s\} = \{(20,\, 10,\, 0),\, (16,\, 10,\, 0)\}$

For the result of S-D pair $\{x_d, x_s\} = \{(20, 10, 0), (16, 10, 0)\}$, we have

$$|x_d - x_c^{(2)}|^2 + |x_s - x_c^{(2)}|^2 \ll |x_d - x_c^{(1)}|^2 + |x_s - x_c^{(1)}|^2.$$

From Figure 6.3, there is a similar observation to the result of S-D pair $\{x_d, x_s\} = \{(4, 10, 0), (0, 10, 0)\}$.

For the result of S-D pair $\{x_d, x_s\} = \{(12, 10, 0), (8, 10, 0)\}$, we only have

$$|x_d - x_c^{(1)}|^2 + |x_s - x_c^{(1)}|^2 < |x_d - x_c^{(2)}|^2 + |x_s - x_c^{(2)}|^2.$$

instead of condition (6.1.12). So we could not see the localized asymptotic behavior (Corollary 6.1) in Figure 6.2, clearly.

Remark 6.2. *Despite visible differences in the values of solutions u_m^n and u_m^a, the times at which they reach their maximums are almost the same for each localized S-D pair. i.e., Compare Figure (6.1) and Figure (6.3) with Figure (6.2).*

Verification II: Let $x_c^{(1)} = (8, 10, 20)$, $x_c^{(2)} = (12, 10, 20)$. These two point targets are too close.

We choose the following three S-D pairs to calculate u_m^n, $u_m^{a,(1)}$ and $u_m^{a,(2)}$:

$$\{x_d, x_s\} \in \{\{(10, 10, 0), (6, 10, 0)\}, \{(12, 10, 0), (8, 10, 0)\}, \{(14, 10, 0), (10, 10, 0)\}\}.$$

The numerical results are shown in Figure 6.4, Figure 6.5 and Figure 6.6 for each S-D pair.

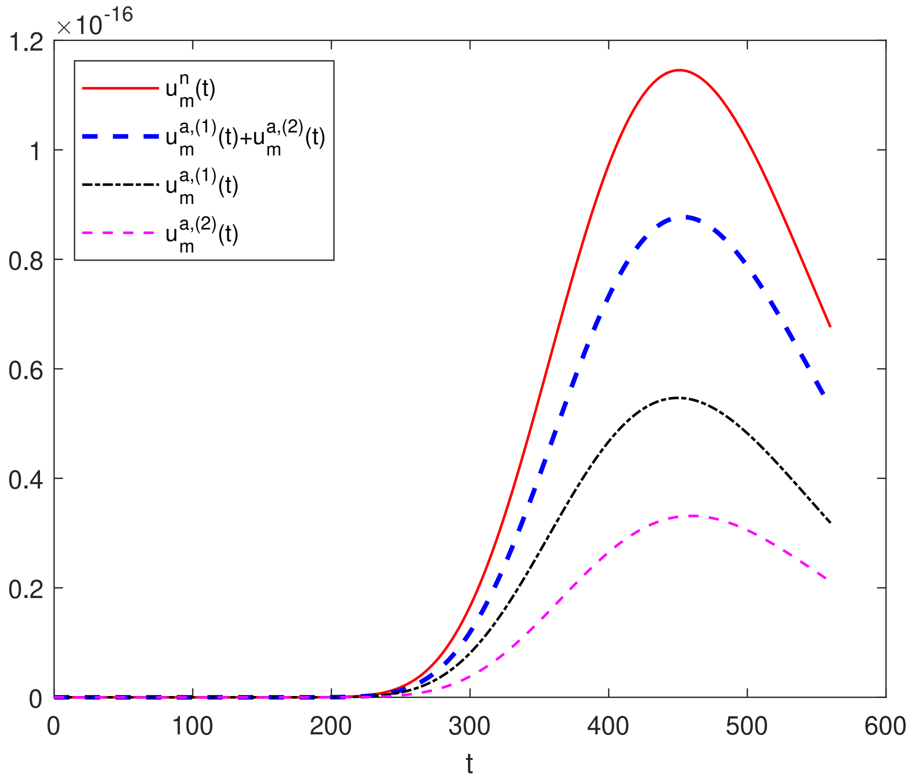

FIGURE 6.4: Numerical solution $u_m^n(x_d, t; x_s)$ and asymptotic solution $u_m^a(x_d, t; x_s)$ of **Verification II** for $\{x_d, x_s\} = \{(10, 10, 0), (6, 10, 0)\}$

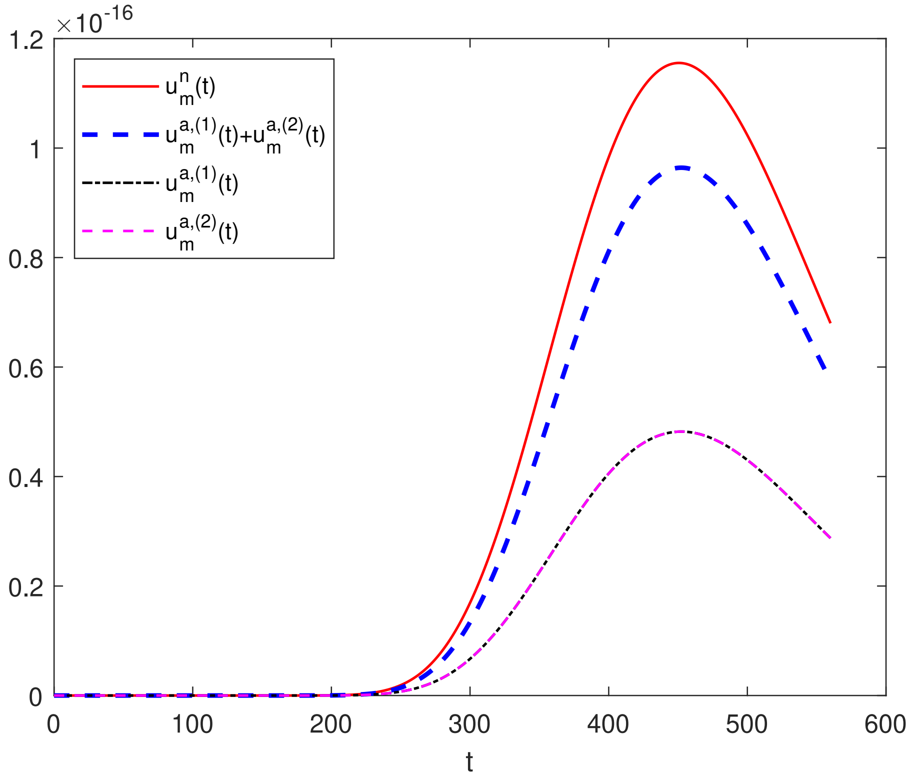

FIGURE 6.5: Numerical solution $u_m^n(x_d, t; x_s)$ and asymptotic solution $u_m^a(x_d, t; x_s)$ of **Verification II** for $\{x_d, x_s\} = \big\{(12, 10, 0), (8, 10, 0)\big\}$

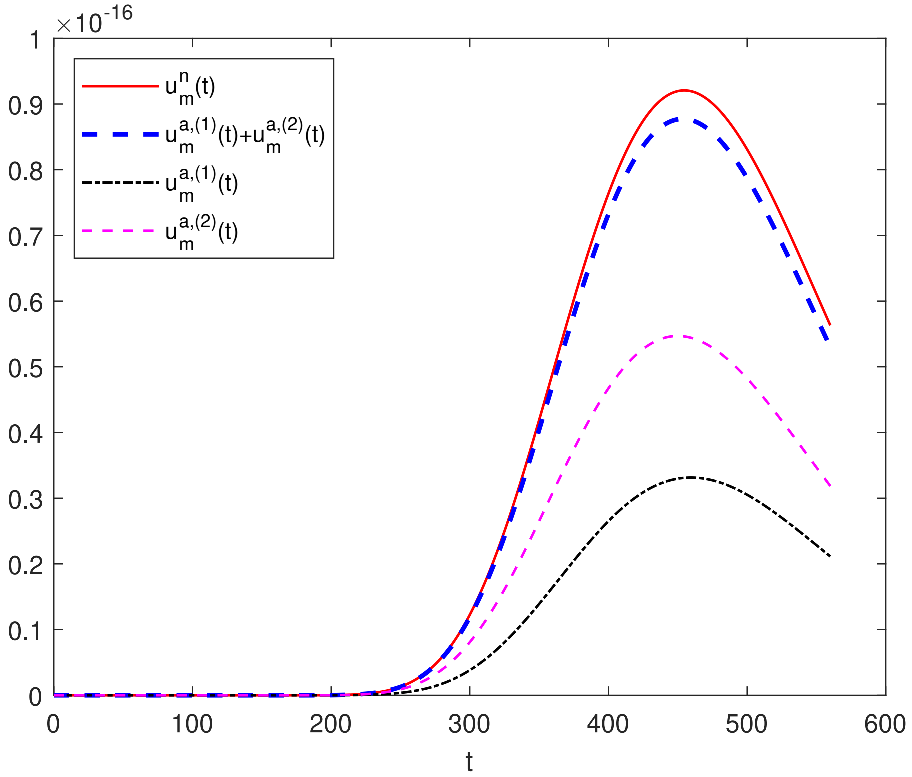

FIGURE 6.6: Numerical solution $u_m^n(x_d, t; x_s)$ and asymptotic solution $u_m^a(x_d, t; x_s)$ of **Verification II** for $\{x_d, x_s\} = \big\{(14, 10, 0), (10, 10, 0)\big\}$

Discussion II: In this verification, the distance between $x_c^{(1)}$ and $x_c^{(2)}$ is smaller than the distance in **Verification I**. For $\{x_d,\, x_s\} = \big\{(10,\, 10,\, 0),\, (6,\, 10,\, 0)\big\}$, which still satisfies

$$|x_d - x_c^{(1)}|^2 + |x_s - x_c^{(1)}|^2 < |x_d - x_c^{(2)}|^2 + |x_s - x_c^{(2)}|^2.$$

In this verification, we could not use $u_m^{a,(1)}$ to locally approximate u_m^n. The same observation is in the case of $\{x_d,\, x_s\} = \big\{(14,\, 10,\, 0),\, (10,\, 10,\, 0)\big\}$. At least, the asymptotic solution $u_m^{a,(1)} + u_m^{a,(2)}$ and the numerical solution u_m^n have almost the same time to reach their maximums. This is also true (see Figure 6.5) for the S-D pair $\{x_d,\, x_s\} = \big\{(12,\, 10,\, 0),\, (8,\, 10,\, 0)\big\}$, which is not a localized S-D pair. So the asymptotic behavior of $\partial_t u_m$ shown in (6.1.5) looks very nice.

6.2 Approximate peak time and its numerical verification

In this section, we define an approximate peak time for each target by using the localized S-D pair. Then, we numerically study the properties of the peak time and verify the accuracy of the approximate peak times.

Let $x_c^{(1)},\, x_c^{(2)},\, \cdots,\, x_c^{(J)}$ be the locations of multiple point targets. From Corollary 6.1, if $x_d,\, x_s \in \partial\Omega$ satisfies

$$|x_d - x_c^{(k)}|^2 + |x_s - x_c^{(k)}|^2 < |x_d - x_c^{(j)}|^2 + |x_s - x_c^{(j)}|^2,\;\; 1 \le j \ne k \le J, \tag{6.2.1}$$

then $\partial_t u_m^a(t) = 0$ implies that

$$\begin{aligned} 0 =& P_3^{(k)}(t;\, x_d,\, x_s,\, x_c^{(k)}) \\ :=& -\mu_a v - \frac{3}{2}t^{-1} + \frac{|x_d - x_c^{(j)}|^2 + |x_s - x_c^{(j)}|^2}{2vD}t^{-2} - \frac{2\beta v D}{x_{c3}^{(j)} + \beta v D t}, \end{aligned} \tag{6.2.2}$$

where $\{x_d,\, x_s\}$ is a localized S-D pair to $x_c^{(k)}$.

We define the approximate peak time for $x_c^{(k)}$, $k = 1,\, 2,\, \cdots,\, J$, as follows.

Definition 6.1. *For each $x_c^{(k)}$, $k = 1,\, 2,\, \cdots,\, J$, if there is a localized S-D pair $\{x_d,\, x_s\}$ satisfying (6.2.1), we can define an approximate time $t_{peak}^{a,(k)} := t_{peak}^a(x_d,\, x_s;\, x_c^{(k)}) > 0$ for $x_c^{(k)}$ such that*

$$P_3^{(k)}(t_{peak}^{a,(k)};\, x_d,\, x_s,\, x_c^{(k)}) = 0,$$

where approximate peak time formula $P_3^{(k)}$ for $x_c^{(k)}$ is defined by (6.2.2).

We give the following remark to the definition of $t_{peak}^{a,\,(k)}$, $k = 1,\, 2,\, \cdots,\, J$.

Remark 6.3. *The approximate peak time formula $P_3^{(k)}(t)$ is the same to $P_3(t)$ defined in (3.2.7) as $x_c^{(k)} = x_c$. From Theorem 4.1, we proved that there is a unique positive root of $P_3^{(k)}(t) = 0$ for any $x_d,\, x_s \in \partial\Omega$. But the approximate peak time $t_{peak}^{a,(k)}$ defined in Definition 6.1 is related to its corresponding localized S-D pair $\{x_d,\, x_s\}$. That is, for any S-D pair $\{x_d,\, x_s\}$, the unique positive root of (6.2.2) is the approximate peak time of $x_c^{(k)}$ depends on whether the current S-D pair satisfies the condition (6.2.1).*

Next, we give some numerical studies from the following two issues: for given $x_c^{(1)},\, x_c^{(2)},\, \cdots,\, x_c^{(J)} \in \Omega$,

(i) study the properties to the peak time t_{peak} of $u_m(t)$ as S-D pair changes.

(ii) study the accuracy of approximating the peak time t_{peak} with the unique positive roots, still denoted by $t^{a,(k)}_{peak}$, of $P^{(k)}_3(t) = 0$, $k = 1, 2, \cdots, J$ for different S-D pair.

We assume two point targets, i.e., $J = 2$ in (2.2.5), with locations $x^{(1)}_c = (5, 10, 20)$, $x^{(2)}_c = (15, 10, 20)$. Give several S-D pairs as

$$\{x_d, x_s\} \in \{\{(1+m, n, 0), (-1+m, n, 0)\}, \quad m, n = 0, 1, \cdots, 20.\}. \tag{6.2.3}$$

The peak time $t_{peak}(x_d, x_s)$ can be observed from the numerical solution $u^n_m(x_d, t; x_s)$ of $u_m(x_d, t; x_s)$. We estimate the accuracy of $t^{a,(1)}_{peak}(x_d, x_s)$ and $t^{a,(2)}_{peak}(x_d, x_s)$ using the absolute errors defined by

$$Err^{(j)}(x_d, x_s) = |t^{a,(j)}_{peak}(x_d, x_s) - t_{peak}(x_d, x_s)|, \quad j = 1, 2.$$

In Figure 6.7, we plot the peak times measured by all S-D pairs defined by (6.2.3), where each grid point (m, n) corresponds to the peak time for $\{x_d, x_s\} = \{(1 + m, n, 0), (-1+m, n, 0)\}$. The approximate peak times $t^{a,(1)}_{peak}(x_d, x_s)$ and $t^{a,(2)}_{peak}(x_d, x_s)$ for all S-D pairs defined by (6.2.3) are shown in Figure 6.8 and Figure 6.9.

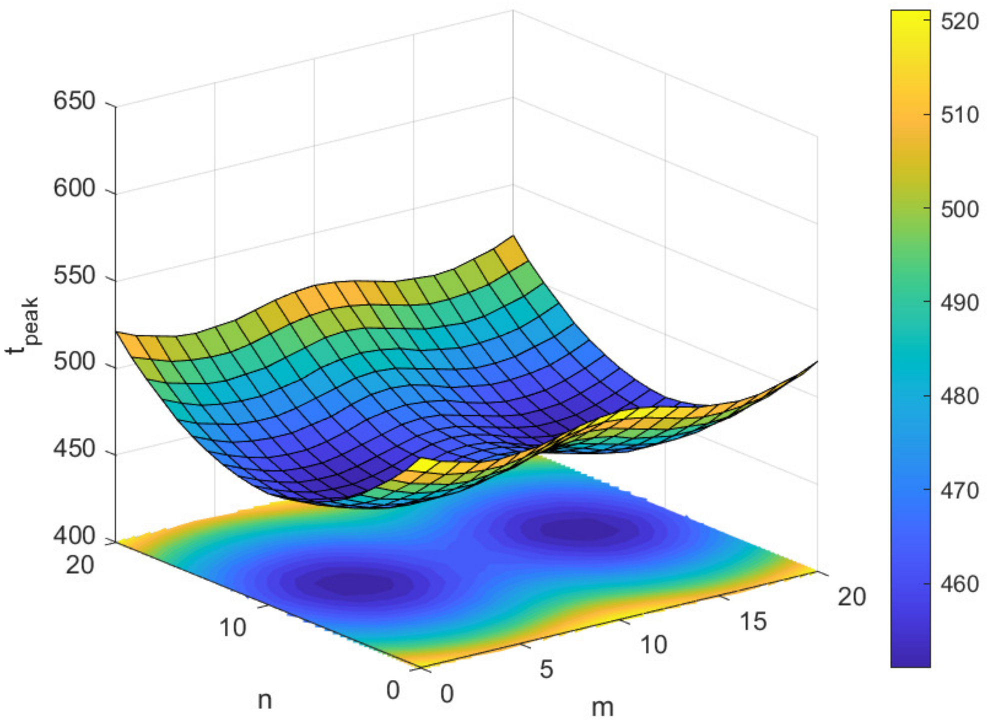

FIGURE 6.7: Peak time $t_{peak}(x_d, x_s)$ for $x^{(1)}_c = (5, 10, 20)$, $x^{(2)}_c = (15, 10, 20)$

We have the following important observations:

(i) For each S-D pair defined by (6.2.3), there exists a unique peak time. In Figure 6.7, there are two local minimums for S-D pair $\{x_d, x_s\} = \{(6, 10, 0), (4, 10, 0)\}$

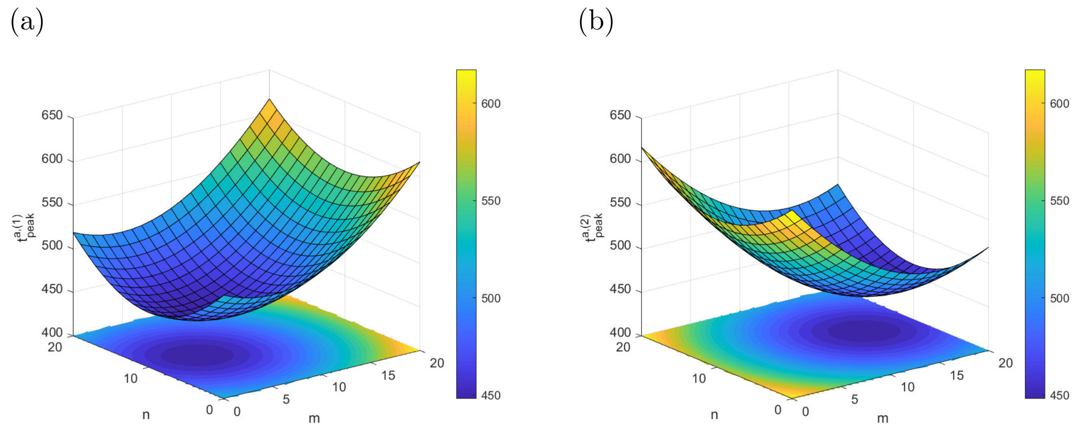

FIGURE 6.8: Approximate peak time: (a) $t^{a,(1)}_{peak}$, (b) $t^{a,(2)}_{peak}$

.

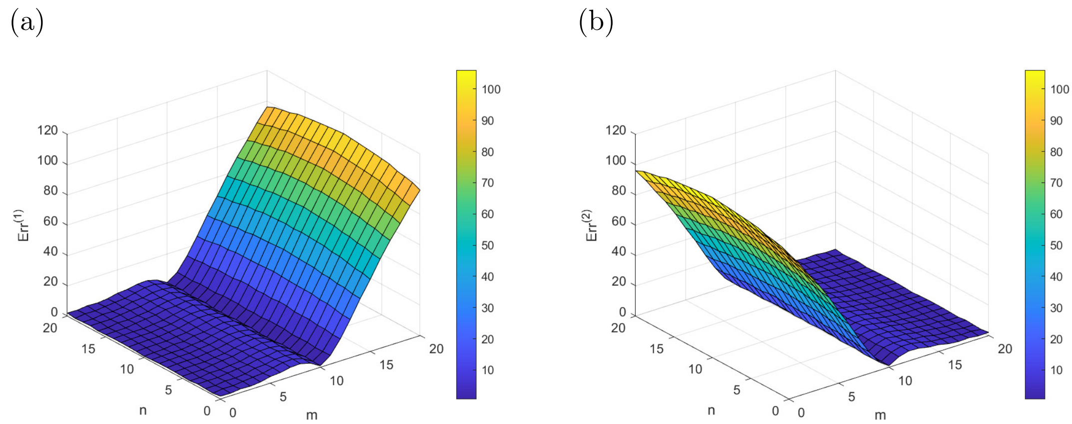

FIGURE 6.9: Absolute error between peak time and approximate peak time: (a) $|t_{peak} - t^{a,(1)}_{peak}|$, (b) $|t_{peak} - t^{a,(2)}_{peak}|$

.

and $\{x_d, x_s\} = \{(16, 10, 0), (14, 10, 0)\}$, respectively. These two S-D pairs are closest to $x_c^{(1)}$ and $x_c^{(2)}$, respectively. That is, the shortest distance from S-D pair to the target gives the smallest peak time (the property of order relation).

(ii) Both $t_{peak}^{a,(1)}$ and $t_{peak}^{a,(2)}$ satisfy the property of order relation. $t_{peak}^{a,(1)}$ and $t_{peak}^{a,(2)}$ reach their minimums as $\{x_d, x_s\} = \{(6, 10, 0), (4, 10, 0)\}$ and $\{x_d, x_s\} = \{(16, 10, 0), (14, 10, 0)\}$, repspectively. Hence, both $t_{peak}^{a,(1)}$ and $t_{peak}^{a,(2)}$ have the same minimization condition as t_{peak}.

(iii) Since the S-D pairs defined by (6.2.3) are close to $x_c^{(1)}$ for $m \leq 10$, the values $t_{peak}^{a,(1)}$ have a good approximation to t_{peak} shown in Figure 6.9 (a). For $m \geq 10$, the values $t_{peak}^{a,(2)}$ have a good approximation to t_{peak}.

Based on the above observations, the localized asymptotic formula of $\partial_t u_m$ given in Corollary 6.1 is reasonable and effective. The approximate peak time can be applied to reconstruct the locations of multiple point targets by choosing a localized S-D pair.

From the comment in Remark 6.1, we can imagine that there is a bad situation as in the following example.

Example 6.1. *Let* $x_c^{(1)} = (9, 10, 20)$, $x_c^{(2)} = (11, 10, 20)$. *We calculate the peak time for different S-D pair* $\{x_d, x_s\}$ *defined by* (6.2.3).

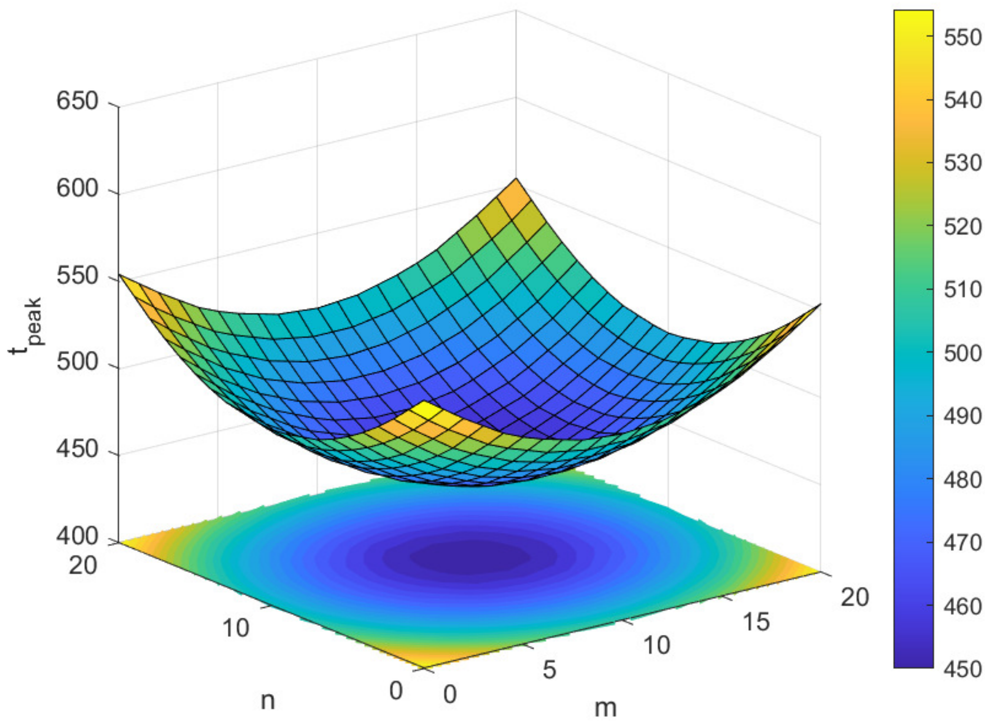

FIGURE 6.10: Peak time $t_{peak}(x_d, x_s)$ for $x_c^{(1)} = (9, 10, 20)$, $x_c^{(2)} = (11, 10, 20)$

From Figure 6.10, we found that there is only one minimum for two close point targets. That is, although there are some localized S-D pairs such that the condition

(6.1.8) assumed in Corollary 6.1 holds, the localized asymptotic formula may not work well for two close point targets.

6.3 Localized reconstruction algorithm

In this section, we propose a localized reconstruction algorithm based on the localized asymptotic formula of $\partial_t u_m$ given in Corollary 6.1. For this, we first introduce the definition of well-separated multiple point targets.

In Section 6.2, we defined the approximate peak time for $x_c^{(j)}$, $j = 1, 2, \cdots, J$, by choosing localized S-D pair. To avoid the situation given in Example 6.1, we define the well-separated multiple point targets as follows.

Definition 6.2. *Let $x_c^{(j)} \in \Omega$, $j = 1, 2, \cdots, J$, be the locations of unknown point targets, where $(x_{c1}^{(j)}, x_{c2}^{(j)}) \in \mathrm{ROI} := (x_l, x_r) \times (x_b, x_t)$. Introduce a uniform partition in* ROI *using a mesh*

$$x^{(m,n)} := \left(m \cdot \frac{x_r - x_l}{M} + x_l,\, n \cdot \frac{x_t - x_b}{N} + x_b,\, 0 \right)$$

for $m = 0, 1, \cdots, M$, $n = 0, 1, \cdots, N$. We define the set Ξ of S-D pairs as

$$\Xi := \Big\{ \{x_d^{(m,n)}, x_s^{(m,n)}\} \; : x_d^{(m,n)} := x^{(m,n)} + (1, 0, 0),\; x_s^{(m,n)} := x^{(m,n)} + (-1, 0, 0), \\ m = 0, 1, \cdots, M,\, n = 0, 1, \cdots, N \Big\}. \tag{6.3.1}$$

Let us further assume that there is a unique peak time for each $\{x_d^{(m,n)}, x_s^{(m,n)}\} \in \Xi$. Then, a set $\mathcal{P}$ of the peak times exists corresponding to Ξ. We say that these J unknown point targets are well-separated if there are J local minimums in $\mathcal{P}$ for J multiple point targets

$$t_{peak}^{min,(j)} := t_{peak}^{min}(x_d^{min,(j)}, x_s^{min,(j)}; x_c^{(1)}, \cdots, x_c^{(J)}), \quad j = 1, 2, \cdots, J, \tag{6.3.2}$$

where the S-D pair $\{x_d^{min,(j)}, x_s^{min,(j)}\} \in \Xi$ is the S-D pair of the smallest distance from the j-th target in Ξ.

Assume that J point targets are well-separated. Hence, we can define J approximate peak times as by (6.2.2) for localized S-D pairs. From the numerical verification shown in Section 6.2, the approximate peak times defined by using localized S-D pairs have a good approximation to the peak time.

By using the property of order relation of the approximate peak time and (6.2.2), we divide the process of reconstructing the locations of multiple point targets into the following two stages.

Stage 1. From the information of J local minimums (6.3.2), we approximately reconstruct the locations $(x_{c1}^{(j)}, x_{c2}^{(j)})$, $j = 1, 2, \cdots, J$, of J point targets denoted by

$$x_{c1}^{(j),inv} := \frac{x_{s_1}^{min,(j)} + x_{d_1}^{min,(j)}}{2}, \qquad x_{c2}^{(j),inv} := \frac{x_{s_2}^{min,(j)} + x_{d_2}^{min,(j)}}{2}. \tag{6.3.3}$$

Stage 2. Substituting $t = t_{peak}^{min,(j)}$, $(x_{c_1}, x_{c_2}) = (x_{c1}^{(j),inv}, x_{c2}^{(j),inv})$ and $\{x_d, x_s\} = \{x_d^{min,(j)}, x_s^{min,(j)}\}$ into the cubic equation (5.1.1), the depth $x_{c3}^{(j),inv}$ can be recovered by solving the cubic equation (5.1.1) for $j = 1, 2, \cdots, J$.

From Proposition 5.1, we can obtain that the reconstructions $x_{c3}^{(j)}$, $j = 1, 2, \cdots, J$, are unique in **Stage 2**.

6.4 Numerical experiments

In this section, we conduct two numerical experiments on the proposed localized reconstruction algorithm for reconstructing multiple point targets.

We assume that there are two unknown point targets, i.e., $J = 2$. We estimate the relative error of the reconstruction computed by the following formula:

$$RelErr = \sum_{j=1}^{2} \frac{|x_c^{(j)} - x_c^{(j),inv}|}{|x_c^{(j)}|},$$

where $x_c^{(j)}$ and $x_c^{(j),inv}$ are the actual and the reconstructed locations of the j-th target, respectively.

Example 6.2. *Let* $x_c^{(1)} = (6, 8, 20)$, $x_c^{(2)} = (14, 12, 20)$ *and* ROI $:= (0, 20) \times (0, 20)$. *We choose the S-D pairs as* (6.3.1) *for* $M = N = 20$.

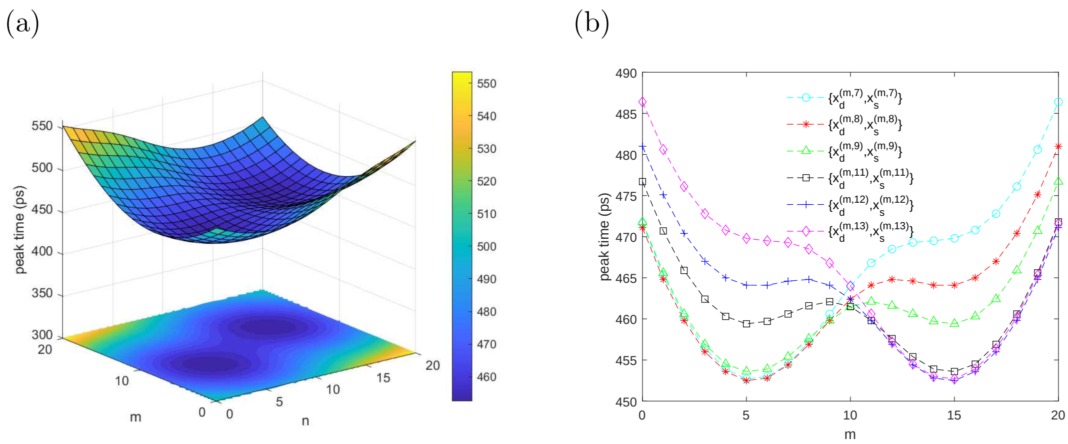

FIGURE 6.11: Noise-free peak times measured by different S-D pairs (6.3.1) in Example 6.2: (a) 3D contour plot of peak times for $m = 0, 1, \cdots, 20$, $n = 0, 1, \cdots, 20$, (b) peak times for $m = 0, 1, \cdots, 20$, $n = 7, 8, 9, 11, 12, 13$

For each S-D pair in the set Ξ defined in (6.3.1), we observe that there is a unique peak time. Hence, 21×21 peak times are measured by 21×21 S-D pairs for $M = N = 20$. In Figure 6.11 (a), the noise-free peak times measured by all S-D pairs in Ξ are plotted as a contour graph. We find that there exist two local minimums, which indicates that there should exist two point targets. For the sake of observation, we plot the changes of the noise-free peak times as $\{x_d^{(m,8)}, x_s^{(m,8)}\}$, $\{x_d^{(m,12)}, x_s^{(m,12)}\}$, $m = 0, 1, \cdots, 20$, and their two neighboring S-D pairs in Figure 6.11 (b). These two local minimums are $t_{peak}^{min,(1)} = 452.5\,\text{ps}$ and $t_{peak}^{min,(2)} = 452.5\,\text{ps}$ for $(n, m) = (8, 5)$ and $(n, m) = (12, 15)$, respectively. According to (6.3.1), we will get the locations of S-D pairs, which give the local minimums. Then, we can compute the reconstructions via (6.3.3) and (5.1.1). As a similar discussion for the measured noise peak times, the numerical results are shown for different noise levels $\hat{\delta}$ in Table 6.1.

TABLE 6.1: Reconstructions for different noise levels in Example 6.2

$x_c^{(1)}, x_c^{(2)}$	$\hat{\delta}$	$x_c^{(1),inv}$	$x_c^{(2),inv}$	$RelErr$
	0	$(5.00, 8.00, 20.18)$	$(15.00, 12.00, 20.18)$	8.28e-2
$(6, 8, 20), (14, 12, 20)$	0.1%	$(6.00, 7.00, 20.18)$	$(15.00, 12.00, 20.18)$	8.28e-2
	1%	$(6.00, 7.00, 20.02)$	$(14.00, 14.00, 18.57)$	1.35e-1

From the results listed in Table 6.1, these two point targets are accurately reconstructed from the peak times under low noise levels ($\hat{\delta} \leq 1\%$). However, two local minimums will not be distinguished when the order of the noise becomes much larger than the height of two bumps, local minimums, of the peak times, as shown in Figure 6.11 (b).

Next, we reconstruct two unknown point targets with different depths.

Example 6.3. *Let* $x_c^{(1)} = (5,\ 5,\ 18)$, $x_c^{(2)} = (15,\ 15,\ 20)$ *and* ROI $:= (0,\ 20) \times (0,\ 20)$. *We choose the S-D pairs as* (6.3.1) *for* $M = N = 20$.

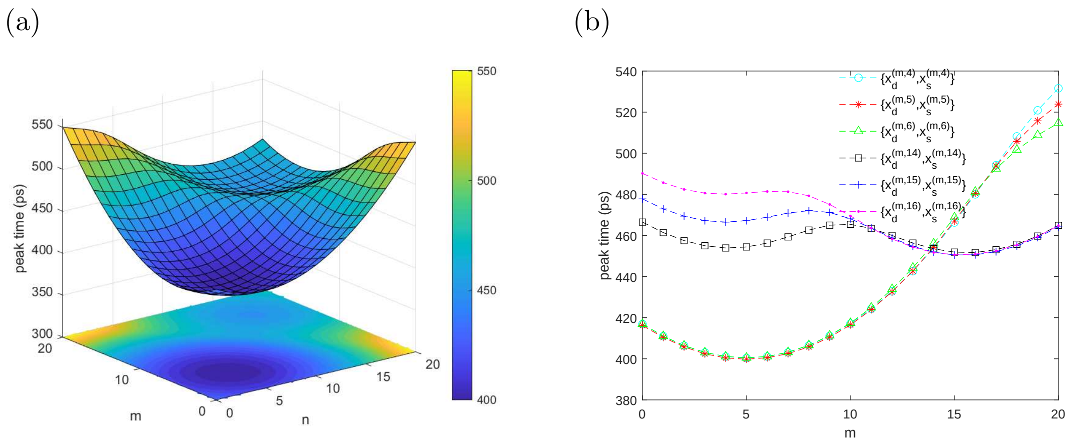

FIGURE 6.12: Noise-free peak times measured by different S-D pairs (6.3.1) in Example 6.3: (a) 3D contour plot of peak times for $m = 0, 1, \cdots, 20$, $n = 0, 1, \cdots, 20$, (b) peak times for $m = 0, 1, \cdots, 20$, $n = 4, 5, 6, 14, 15, 16$

As in the previous Example 6.2, we observe a unique peak time for each S-D pair and have 21×21 peak times. In Figure 6.12 (a), the noise-free peak times measured by all S-D pairs in Ξ are plotted as a contour graph. In Figure 6.12 (b), we plot the changes of the peak times as $\{x_d^{(m,5)},\ x_s^{(m,5)}\}$, $\{x_d^{(m,15)},\ x_s^{(m,15)}\}$, $m = 0,\ 1,\ \cdots,\ 20$, and their two neighboring S-D pairs. There are two local minimums $t_{peak}^{min,(1)} = 399.8\,\text{ps}$ and $t_{peak}^{min,(2)} = 450.5\,\text{ps}$ for $(n,\ m) = (5,\ 5)$ and $(n,\ m) = (15,\ 15)$, respectively. By the same discussions as in Example 6.2, the numerical results are shown for different noise levels $\hat{\delta}$ in Table 6.2.

Similarly, two unknown point targets can be well reconstructed from the peak times under low noise levels ($\hat{\delta} \leq 1\%$). From Figure 6.12 (b), the peak times for the S-D pairs $\{x_d^{(m,5)},\ x_s^{(m,5)}\}$ are more affected by the target at the shallow depth, but those for the

TABLE 6.2: Reconstructions for different noise levels in Example 6.3

$x_c^{(1)}, x_c^{(2)}$	$\hat{\delta}$	$x_c^{(1),inv}$	$x_c^{(2),inv}$	$RelErr$
$(5, 5, 18), (15, 15, 20)$	0	$(5.00, 5.00, 18.05)$	$(15.00, 15.00, 20.10)$	6.02e-3
	0.1%	$(5.00, 5.00, 18.05)$	$(15.00, 16.00, 20.10)$	3.71e-2
	1%	$(6.00, 5.00, 17.92)$	$(16.00, 14.00, 20.02)$	1.00e-1
	5%	$(6.00, 5.00, 17.51)$	—	—

S-D pair $\{x_d^{(m,15)}, x_s^{(m,15)}\}$ are less affected by the targets but from both the targets, as $m = 0, 1, \cdots, 20$. The reason is due to the different depths of the two unknown targets; the S-D pairs $\{x_d^{(m,5)}, x_s^{(m,5)}\}$ are closer to the target at the shallower depth. An increase in the noise level ($\hat{\delta}$= 5%) makes the two local minimums of the peak times indistinguishable, resulting in only one point target being reconstructed and another target being invisible. Comparing the inversion results of a single unknown point target, the reconstruction of two unknown point targets sensitively depends on the errors of the measured peak times due to the interaction between point targets. Hence, proper preprocessing of data, such as a denoising method, must reduce the influence of noise contained in the peak times.

According to the results of Example 6.2 and Example 6.3, it is feasible to apply the peak time and peak time formula defined by the localized asymptotic formula to reconstruct multiple point targets. The localized reconstruction algorithm is a generalization of the bisection reconstruction algorithm under the condition that the multiple point targets should be well-separated.

Chapter 7

Application of Approximate Peak Time to Unknown Target with Volume

In this chapter, we try to numerically reconstruct the location of an unknown target with a small volume from measured peak times. Since its volume is very small, we reconstruct the location of the target as if it is a single point target which is any fixed point inside the target. Thus, we can directly apply the approximate peak time and the approximate peak time formula defined in Chapter 4 for a single point target. We conduct some numerical experiments to numerically extend the bisection reconstruction algorithm for reconstructing the target.

Let μ_f have the form:

$$\mu_f(x) = c\chi_\omega(x), \quad x \in \Omega,\, \omega \Subset \Omega, \tag{7.0.1}$$

where $c > 0$ is a positive constant and χ_ω is the characteristic function of a strictly convex bounded domain ω. Then, the solution u_m to (2.2.2) is given as

$$\begin{aligned} &u_m(x, t; x_s) \\ &= D \int_0^t \int_\omega \mu_f(y)\mathcal{K}(x, y; t-s)\mathcal{K}(y, x_s; s)\,\mathrm{d}y\mathrm{d}s, \quad (x, t) \in \overline{\Omega} \times (0, T), \end{aligned} \tag{7.0.2}$$

where $\mathcal{K}(x, y; t)$ is the Green function associated with (2.2.2) defined by (2.2.4).

Let us give a numerical scheme for calculating the numerical solution $u_m^n(x_d,\, t;\, x_s)$ of $u_m(x_d,\, t;\, x_s)$ for $x_d,\, x_s \in \partial\Omega$. Then, the peak time can be observed from u_m^n. For the spatial integral region ω, we divide it into K small regions ω_k, $k = 1,\, 2,\, \cdots,\, K$ satisfying $\omega = \bigcup_{k=1}^K \omega_k$. Let the integral interval $(0,\, t)$ be divide into J equal subintervals with step size Δt with grid points $t_j = j \cdot \Delta t, \quad j = 0,\, 1,\, \cdots,\, J$. we calculate the numerical solution $u_m^n(t)$ of $u_m(t)$ at $t = t_j$ by

$$u_m^n(x_d,\, t_j;\, x_s) = \Delta t D \left(\sum_{j'=1}^{j} \sum_{k=1}^{K} |\omega_k| \mu_f(y_k) \mathcal{K}(x_d, y_k; t_j - s_{j'}) \mathcal{K}(y_k, x_s; s_{j'}) \right), \tag{7.0.3}$$

where $y_k \in \omega_k$, $|\omega_k|$ is the area of subdomain ω_k, $k = 1,\, 2,\, \cdots,\, K$. $s_{j'} = j' \cdot \Delta t$, $j' = 1,\, 2,\, \cdots,\, J$.

The rest of this chapter is organized as follows. In Section 7.1, we formulate our inverse problem as reconstructing a marker point of ω and then directly use the bisection reconstruction algorithm. We give some numerical experiments to examine the performance of this algorithm in Section 7.2.

7.1 Formulation of inverse problem and reconstruction scheme

In this section, we simplify the problem of reconstructing ω to reconstruct one marker point $x_c := (x_{c_1}, x_{c_2}, x_{c_3})$ of ω, where x_c is any fixed point in ω.

Now, our inverse problem is reduced as follows.

Inverse Problem: Reconstruct x_c from the measured peak times given as

$$t_{peak}^{(n)} := t_{peak}(x_d^{(n)}, x_s^{(n)}) = \{t : \arg\max_{t>0} u_m^n(x_d^{(n)}, t; x_s^{(n)})\}, \, n = 1, 2, \cdots, N,$$

where $\{x_d^{(n)}, x_s^{(n)}\}$, $n = 1, 2, \cdots, N$, are N sets of source and detector points (S-D pair) located on $\partial\Omega$. The temporal function $u_m^n(x_d^{(n)}, t; x_s^{(n)})$ is defined by (7.0.3).

For the inverse problem, we directly apply the bisection reconstruction algorithm given in Algorithm 2 to reconstruct x_c. The only difference compared with the experiments given in Section 5.3 is that the peak time is observed from u_m^n defined by (7.0.3). To consider the measured peak times inevitably containing noise, we generate the noisy peak times t_{peak}^{δ} via (5.3.2).

7.2 Numerical experiments

In this section, we give two numerical experiments for reconstructing the marker point x_c of the unknown small ball-shaped target. For a small ball-shaped target with constant absorption strength of fluorescence $c = 1$, we temporarily regard the marker point x_c as the center of the ball. Then, we estimate the relative error of the reconstruction x_c^{inv} computed by (5.3.3).

Example 7.1. *Let* $\omega := \{(x_1, x_2, x_3) : (x_1-x_{c_1})^2+(x_2-x_{c_2})^2+(x_3-x_{c_3})^2 < 0.25^2\}$ *with* $(x_{c_1}, x_{c_2}, x_{c_3}) = (10, 10, 10)$*. We set the parameters* $\mathrm{ROI} = (0, 20)\times(0, 20)$, $L = 8$ *and* $\epsilon_1 = \epsilon_2 = 0.1$ *in Algorithm 2. The results of numerical inversions for different noise levels* $\hat{\delta}$ *are listed in Table 7.1.*

Table 7.1: Reconstructions of marker point of target for different noise levels $\hat{\delta}$ in Example 7.1

x_c	$\hat{\delta}$	x_c^{inv}	$RelErr$
$(10, 10, 10)$	0	$(9.96, 10.04, 10.07)$	5.10e-03
	0.1%	$(9.96, 10.04, 10.07)$	5.10e-03
	1%	$(9.96, 10.04, 9.94)$	4.85e-03
	5%	$(9.88, 10.04, 10.29)$	1.81e-02

Here, ω is a ball with x_c as its center and 0.25 as its radius. The radius of the ball is very small compared to the distance between the center of the ball and the boundary $\partial\Omega$. So it is reasonable to assume the target is a point target x_c.

From the numerical results shown in Table 7.1, we found the marker point of the unknown target has been reconstructed very well. For the relative noise level $\hat{\delta} \le 1\%$, x_c^{inv} are always inside ω. In other words, the result of reconstruction still represents some information of the target. Even for the data with large relative noise level ($\hat{\delta} = 5\%$), the absolute error for each reconstructed coordinate of x_c^{inv} is less than 0.3 mm. The reconstructed marker point is very close to the boundary of ω.

Next, we consider the case of the unknown target inside the domain Ω with deep depth.

Example 7.2. *Let* $\omega = \{(x_1, x_2, x_3) : (x_1 - x_{c_1})^2 + (x_2 - x_{c_2})^2 + (x_3 - x_{c_3})^2 < 0.25^2\}$ *with* $(x_{c_1}, x_{c_2}, x_{c_3}) = (10, 10, 20)$. *We set the parameters* $\mathrm{ROI} = (0, 20) \times (0, 20)$, $L = 8$ *and* $\epsilon_1 = \epsilon_2 = 0.1$ *in Algorithm 2. The results of numerical inversions for different noise levels* $\hat{\delta}$ *are listed in Table 7.2.*

Table 7.2: Reconstructions of marker point of target for different noise levels $\hat{\delta}$ in Example 7.2

x_c	$\hat{\delta}$	x_c^{inv}	$RelErr$
$(10, 10, 20)$	0	$(10.04, 10.00, 20.02)$	1.78e-03
	0.1%	$(10.04, 9.96, 20.04)$	2.70e-03
	1%	$(10.12, 9.88, 20.20)$	1.06e-02
	5%	$(9.96, 10.04, 20.20)$	8.51e-03

Compare the numerical results shown in Table 7.2 with Table 7.1, our reconstruction scheme is less affected by the depth of the unknown target. From the results for $\hat{\delta} = 0$, we obtain that there must be a marker point in ω that satisfies the approximate peak time formula (4.1.1) because the reconstructed x_c^{inv} always inside ω, where (4.1.1) is the approximate peak time formula for the point target.

Since the inverse problem is ill-posed, it is usually necessary to regularize the reconstruction process to overcome the influence of noise. From Table 7.1 and Table 7.2, our reconstruction scheme is robust to noise without any regularization.

We close this chapter with some discussions. Even though in this chapter, we do not derive the approximate peak time for the target with volume to discuss its properties. Indirectly, we can come to the following conclusions:

(i) The peak time for the target with volume should have the same properties as the peak time for the point target.

(ii) The peak time for the target with volume should be an approximate positive root of (4.1.1), where (4.1.1) is the approximate peak time formula for the point target.

These conclusions inspire us to study the FDOT problem for the target with volume by using peak time. Of course, it should be pointed out that we assume that ω is a ball. The good symmetry of the ball with respect to the center of the ball provides a good basis for our inversion. For more general ω, such as slender bars, we need to give a rigorous mathematical theoretical study.

Chapter 8

Conclusion and Future Works

Conclusion

In this thesis, we focused on reconstructing the locations of unknown point targets using peak times, which are clearly observed in temporal response function $u_m(x_d, t; x_s)$ for given $\{x_d, x_s\}$ on the measurement surface. Analyzing the asymptotic behaviors of u_m and $\partial_t u_m$, we derived the approximate peak time formula as a cubic polynomial equation. Its positive root is the approximate peak time. We analyzed the properties of the approximate peak time (uniqueness, order relation, symmetry, and accuracy) and numerically verified the peak time. Based on these analyses, we proposed the bisection reconstruction algorithm to reconstruct the location of a single point target, where the peak time is used as the index to shrink ROI. For the case of multiple point targets, we derived a localized asymptotic analysis of the solution. Under the well-separated assumption between targets, we proposed a localized reconstruction algorithm. We remark on the advantage of considering the peak time. The peak time is uniquely and visibly identified in the measured data. It is the least noisy data point in $u_m(x_d, t; x_s)$, making it potentially robust for identification. Through our analysis, we found that the peak time directly reflects the relation between the S-D pair and the target.

We close the conclusion by summarizing the novelties of this study as follows.

- We found no other study that analytically derived the approximate peak time formula and systematically used it for reconstructing the locations of unknown targets.
- In the theoretical part, our asymptotic analysis took care of β, coming from the boundary influence. As a consequence, we obtained a much more accurate approximation of the peak time, which fits more practical situations.
- The proposed algorithm is a direct imaging method by comparing the order of the measured peak times. There are no complicated calculations and regularization. For given ROI, the projections of reconstructed targets are always in ROI. Further, we do not need to deliberately choose ROI, except for including the projections of targets. Moreover, it is potentially robust and accurate for reconstructing target locations deeply embedded.
- Our analysis is also useful for reconstructing a target with a small volume. That is, our algorithm can provide better initial guesses for more accurate reconstruction.

Future works

Based on the current work, there are three prospects for future research as follows.

- From the numerical results shown in Chapter 7, we only obtain a rough reconstruction of the target with volume. We need to give a detailed mathematical analysis to obtain a more accurate reconstruction scheme.
- We can apply our method to practical experimental data.
- We can consider the fluorescence lifetime $\ell > 0$ instead of $\ell \to 0$ in our mathematical model of FDOT, which should be more practical. The peak time will be delayed for $\ell > 0$.

Bibliography

[1] J. Abascal, J. Chamorro-Servent, J. Aguirre, S. Arridge, T. Correia, J. Ripoll, J. Vaquero and M. Desco, Fluorescence diffuse optical tomography using the split Bregman method, *Med. Phys.*, 38 (2011), 6275–6284.

[2] H. Ammari, J. Garnier and L. Giovangigli, Mathematical modeling of fluorescence diffuse optical imaging of cell membrane potential changes, *Quart. Appl. Math.*, 72 (2014), 137–176.

[3] S. Arridge, Optical tomography in medical imaging, *Inverse Problems*, 15 (1999), 41–93.

[4] S. Arridge, M. Cope and D. Delpy, The theoretical basis for the determination of optical pathlengths in tissue: temporal and frequency analysis, *Phys. Med. Biol.*, 37 (1992), 1531–1560.

[5] S. Arridge and J. Schotland, Optical tomography: forward and inverse problems, *Inverse Problems*, 12 (2009), 123010.

[6] K. Ayyalasomayajula and P. K. Yalavarthy, Analytical solutions for diffuse fluorescence spectroscopy/imaging in biological tissues. Part I: zero and extrapolated boundary conditions, *J. Opt. Soc. Am. A*, 30 (2013), 537–552.

[7] A. Behrooz, H. Zhou, A. Eftekhar and A. Adibi, Total variation regularization for 3D reconstruction in fluorescence tomography: experimental phantom studies, *Appl. Opt.*, 51 (2012), 8216–8227.

[8] J. Baritaux, K. Hassler and M. Unser, An efficient numerical method for general L(p) regularization in fluorescence molecular tomography, *IEEE Trans. Med. Imag.*, 29 (2010), 1075–1087.

[9] Y. Bérubé-Lauzière and V. Robichaud, Time-resolved fluorescence measurements for diffuse optical tomography using ultrafast time-correlated single photon counting, *Proc. SPIE*, 6372 (2006), 637206.

[10] S. Chandrasekhar, *Radiative Transfer*, Dover Publications, New York, 1960.

[11] S. Chen, J. Eom, G. Nakamura and G. Nishimura, Approximate peak time and its application to time-domain fluorescence diffuse optical tomography, *Commun. Anal. Comput.*, 1 (2023), 379–406.

[12] N. Ducros, C. Andrea, A. Bassi and F. Peyrin, Fluorescence diffuse optical tomography: Time-resolved versus continuous–wave in the reflectance configuration, *IRBM*, 32 (2011), 243–250.

[13] N. Ducros, L. Hervé, A. Da Silva, J. Dinten and F. Peyrin, A comprehensive study of the use of temporal moments in time-resolved diffuse optical tomography: part I. Theoretical material, *Phys. Med. Biol.*, 54 (2009), 7089–7105.

[14] N. Ducros, A. Silva, J. Dinten, C. Seelamantula, M. Unser and F. Peyrin, A time–domain wavelet–based approach for fluorescence diffuse optical tomography, *Med. Phys.*, 37 (2010), 2890–2900.

[15] T. Durduran, R. Choe, W. Baker and A. Yodh, Diffuse optics for tissue monitoring and tomography, *Rep. Prog. Phys.*, 73 (2010), 076701.

[16] H. W. Engl, M. Hanke and A. Neubauer, *Regularization of Inverse Problems*, Kluwer Academic Publishers, Dordrecht, 1996.

[17] J. Eom, M. Machida, G. Nakamura, G. Nishimura and C. Sun, Expressions of the peak time for time-domain boundary measurements of diffuse light, *J. Math. Phys.*, 64 (2023), 083504.

[18] J. Eom, G. Nakamura, G. Nishimura and C. Sun, Local analysis for locating a single point target in time-domain fluorescence diffuse optical tomography, *Differ. Integral Equ.*, 37 (2024), 27–58.

[19] K. Furutsu and Y. Yamada, Diffusion approximation for a dissipative random medium and the applications, *Phys. Rev. E*, 50 (1994), 3634–3640.

[20] F. Gao, H. Zhao, L. Zhang, Y. Tanikawa, A. Marjono and Y. Yamada, A self-normalized full time-resolved method for fluorescence diffuse optical tomography, *Opt. Exp.*, 16 (2008), 13104–13121.

[21] J. Hadamard, *Lectures on the Cauchy Problem in Linear Partial Differential Equations*, Yale University Press, New Haven, 1923.

[22] D. Hall, G. Ma, F. Lesage and Y. Wang, Simple time–domain optical method for estimating the depth and concentration of a fluorescent inclusion in a turbid medium, *Opt. Lett.*, 29 (2004), 2258–2260.

[23] S. Han, S. Farshchi-Heydari and D. Hall, Analytical method for the fast time–domain Reconstruction of fluorescent inclusions in vitro and in vivo, *Biophys. J.*, 98 (2010), 350–357.

[24] D. Han, J. Tian, S. Zhu, J. Feng, C. Qin, B. Zhang and X. Yang, A fast reconstruction algorithm for fluorescence molecular tomography with sparsity regularization, *Opt. Exp.*, 18 (2010), 8630–8646.

[25] D. Han, X. Yang, K. Liu, C. Qin, B. Zhang, X. Ma and J. Tian, Efficient reconstruction method for L1 regularization in fluorescence molecular tomography, *Appl. Opt.*, 49 (2010), 6930–6937.

[26] M. Hanke, A regularizing Levenberg-Marquardt scheme with applications to inverse ground-water filtration problems, *Inverse Problems*, 13 (1997), 79–95.

[27] L. Hervé, A. Koenig and J. Dinten, Non-uniqueness in fluorescence-enhanced continuous wave diffuse optical tomography, *J. Opt.*, 13 (2011), 015702.

[28] Y. Hoshi and Y. Yamada, Overview of diffuse optical tomography and its clinical applications, *J. Biomed. Opt.*, 9 (2016), 091312.

[29] V. Isakov, *Inverse Problems for Partial Differential Equations*, Third Edition, Springer, Cham, 2017.

[30] K. Ito and B. Jin, *Inverse Problems: Tikhonov Theory and Algorithms*, World Scientific Publishing Co. Pte. Ltd., Hackensack, NJ, 2015.

[31] H. Jiang, *Diffuse Optical Tomography: Principles and Applications*, CRC Press, Boca Raton, 2010.

[32] H. Jiang, *Fluorescence Molecular Tomography: Principles and Applications*, Springer Cham, Switzerland, 2022.

[33] S. Kabanikhin, Definitions and examples of inverse and ill-posed problems, *J. Inverse Ill-Posed Probl.*, 16 (2008), 317–357.

[34] P. Mohajerani, A. Eftekhar, J. Huang and A. Adibi, Optimal sparse solution for fluorescent diffuse optical tomography: theory and phantom experimental results, *Appl. Opt.*, 46 (2007), 1679–1685.

[35] B. Kaltenbacher, A. Neubauer and O. Scherzer, *Iterative Regularization Methods for Nonlinear Ill-posed Problems*, Walter de Gruyter GmbH, Berlin-New York, 2008.

[36] J. Keller, Inverse Problems, *Amer. Math. Monthly*, 83 (1976), 107–118.

[37] A. Kirsch, *An Introduction to the Mathematical Theory of Inverse Problems*, Springer-Verlag, New York, 1996.

[38] A. Laidevant, A. Da Silva, M. Berger, J. Boutet, J. Dinten and A. Boccara, Analytical method for localizing a fluorescent inclusion in a turbid medium, *Appl. Opt.*, 46 (2007), 2131–2137.

[39] S. Lam, F. Lesage and X. Intes, Time domain fluorescent diffuse optical tomography: analytical expressions, *Opt. Exp.*, 13 (2005), 2263–2275.

[40] J. Liu, M. Machida, G. Nakamura, G. Nishimura and C. Sun, On fluorescence imaging: the diffusion equation model and recovery of the absorption coefficient of fluorophores, *Sci. China Math.*, 65 (2022), 1179–1198.

[41] Y. Liu, W. Ren and H. Ammari, Robust reconstruction of fluorescence molecular tomography with an optimized illumination pattern, *Inverse Probl. Imaging*, 14 (2020), 535–568.

[42] F. Marttelli, S. Bianco, A. Ismaelli and G. Zaccanti, *Light Propagation through Biological Tissue and Other Diffusive Media: Theory, Solutions, Software*, SPIE Press, Bellingham, 2010.

[43] A. Milstein, S. Oh, K. Webb, C. Bouman, Q. Zhang, D. Boas and R. Millane, Fluorescence optical diffusion tomography, *Appl. Opt.*, 42 (2003), 3081–3094.

[44] M. Mycek and B. Pogue, *Handbook of Biomedical Fluorescence*, Marcel Dekker, New York, 2003.

[45] F. Natterer, *The Mathematics of Computerized Tomography*, SIAM, Philadelphia, 2001.

[46] M. Niedrea, R. de Kleinea, E. Aikawa, D. Kirscha, R. Weissledera and V. Ntziachristos, Early photon tomography allows fluorescence detection of lung carcinomas and disease progression in mice in vivo, *Proc. Nat. Acad. Sci.*, 105 (2008), 19126–19131.

[47] V. Nitziachristos, C. Tung, C. Bremer and R. Weissleder, Fluorescence molecular tomography resolves protease activity in vivo, *Nat. Med.*, 88 (2002), 757–761.

[48] K. Papadimitriou, E. Rosas, E. Zhand, R. Cooper, J. Hebden, S. Arridge and S. Powell, Dual wavelength spread-spectrum time-resolved diffuse optical instrument for the measurement of human brain functional responses, *Biomed. Opt. Express*, 11 (2020), 3477–3490.

[49] K. Prieto and G. Nishimura, A new scheme of the time-domain fluorescence tomography for a semi-infinite turbid medium, *Opt. Rev.*, 24 (2017), 242–251.

[50] K. Sikorski, Bisection is optimal, *Numer. Math.*, 40 (1982), 111–117.

[51] C. Sun, Mathematical Study on Fluorescence Diffuse Optical Tomography—Recovering the Distribution of Fluorophores Using Cuboid Approximation, *PhD theis*, Hokkaido University, 2020.

[52] C. Sun, G. Nakamura, G. Nishimura, Y. Jiang, J. Liu and M. Machida, Fast and robust reconstruction algorithm for fluorescence diffuse optical tomography assuming a cuboid target, *J. Opt. Soc. Am. A*, 37 (2020), 231–239.

[53] W. Symes, The seismic reflection inverse problem, *Inverse Problems*, 25 (2009), 123008.

[54] L. Wang and J. Liu, On fluorophore imaging by diffusion equation model: decompositions and optimizations, *Acta Math. Appl. Sin. Engl. Ser.*, 36 (2020), 203–222.

[55] M. Williams, The Milne problem with Fresnel reflection, *J. Phys. A: Math. Gen.*, 38 (2005), 3841–3856.

[56] Q. Zhu, H. Dehghani, K. Tichauer, R. Holt, K. Vishwanath, F. Leblond and B. Pogue, A three-dimensional finite element model and image reconstruction algorithm for time-domain fluorescence imaging in highly scattering media, *Phys. Med. Biol.*, 56 (2011), 7419–7434.

List of Figures

List of Tables

List of Abbreviations

FDOT	**F**luorescence **D**iffuse **O**ptical **T**omography
FMT	**F**luorescence **M**olecular **T**omography
DOT	**D**iffuse **O**ptical **T**omography
RTE	**R**adiative **T**ransfer **E**quation
DE	**D**iffusion **E**quation
CW	**C**ontinuous **W**ave
FD	**F**requency **D**omain
TD	**T**ime **D**omain
S-D	**S**ource-**D**etector
ROI	**R**egion **O**f **I**nterest

List of Symbols

symbol	*definition*	*name*
Ω	$\mathbb{R}^3_+$	half space
ω		support of fluorophore
$\partial\Omega$		boundary surface
$\mathbb{S}^2$		unit sphere
t		time
x_c		location of point target
x_d		location of point detector
x_s		location of point source
v		speed of light propagation
Φ_e		radiant intensity of excitation
Φ_m		radiant intensity of emission
U_e		photon density of excitation for nonlinear DE model
U_m		photon density of of emission for nonlinear DE model
u_e		photon density of excitation for lineared DE model
u_m		photon density of emission for lineared DE model
u_m^a		asymptotic solution of u_m
μ_a		absorption coefficient of medium
μ_f		absorption coefficient of fluorophore
μ_s		scattering coefficient of medium
c		absorption strength of fluorescence
g		anisotropy parameter (or average scattering cosine)
D	$1/(3\mu_s(1-g))$	photon diffusion coefficient
τ	vt/D	non-dimensional time
ρ_c	x_c/D	non-dimensional location of point target
ρ_d	x_d/D	non-dimensional location of point detector
ρ_s	x_s/D	non-dimensional location of point source
θ		angular direction variable (or solid angle)
γ		quantum efficiency of the fluorescence
ℓ		fluorescence lifetime
$\eta(\theta, \theta')$		scatter phase function from direction θ into θ'
ν		unit outward normal vector
R		Fresnel reflection coefficient
β		Robin coefficient
erfc		complementary error function
$\mathcal{K}$		Green function to diffusion equation
t_{peak}		peak time at which the photon density is strongest
t_{peak}^a		approximate peak time
$\hat{\delta}$		relative noise level

Physical Constants in Simulations

Speed of Light in the Medium	$v = 0.219\,\mathrm{mm/ps}$
Quantum Efficiency of the Fluorescence	$\gamma = 1$
Absorption Coefficient of the Medium	$\mu_a = 0.1\,\mathrm{mm}^{-1}$
Fluorescence Lifetime	$\ell = 0\,\mathrm{ps}$
Photon Diffusion Coefficient	$D = 1/3\,\mathrm{mm}$
Robin Coefficient	$\beta = 0.5493\,\mathrm{mm}^{-1}$
Absorption Strength of the Fluorescence	$c = 1$